UNIVERSITY OF CALIFORNIA,
IRVINE

Elucidation and Impact of Photoacid Proton-Transfer Regeneration Dynamics

DISSERTATION

submitted in partial satisfaction of the requirements
for the degree of

DOCTOR OF PHILOSOPHY

in Chemistry

by

Simon Luo

Dissertation Committee:
Associate Professor Shane Ardo, Chair
Chancellor's Professor Reginald M. Penner
Professor Matthew D. Law

2021

Chapter 3 has been reproduced with permission from the Royal Society of Chemistry:
S. Luo, W. White, J. M. Cardon and S. Ardo, *Energy Environ. Sci.*, DOI:10.1039/D1EE00482D.

DEDICATION

To

my parents

for all you have given and your never-ending support.

四歲粵語辯論
Heated Cantonese exchange at four-years-old

父母: 你知道你做错了吗?
Parents: Do you know what you did wrong?

我: 知道.
Me: Yeah.

父母: 你做错(坐)哪里?
Parents: Where were you wrong(sitting)?

我: 我坐在地板上!
Me: I'm sitting on the ground!

TABLE OF CONTENTS

Page

LIST OF FIGURES

Page

LIST OF TABLES

Page

ACKNOWLEDGEMENTS

First and foremost, I would like to thank my committee chair, Professor Shane Ardo, for his mentorship and guidance during my time at UCI. Your enthusiasm with anything you learn, whether it drives the forefront of your research, or whether it expands on your knowledge of general chemistry, kept me motivated and taught me that there is always more to know. Your attitude towards science is contagious and your ability to engage interdisciplinary research is reflected in the diverse students you bring aboard. In addition, I would like to thank my committee members, Professor Reginald M. Penner and Professor Matthew D. Law in their participation and feedback in this dissertation and presentation.

I need to thank my labmates for their support during the pursuit of my degree. In particular, I would like to thank Dr. William White, who was my point-of-contact and mentor during my first years in lab, and Dr. Joseph Cardon and Dr. Kevin Tkaczibson, for their work in building our nanosecond transient absorption system and mentorship when I knew little-to-nothing about transient spectroscopy. To everyone in the group, both past and present, I need to thank you for being such inclusive people both academically and socially. The collaborative nature of the lab made it easier to deal with the rollercoaster that is graduate school, and I enjoyed the random day to day interactions we engaged in.

I would like to acknowledge the various people/facilities who have enabled my research: Dr. Dmitry Fishman, director of UCI's Laser Spectroscopy Labs; Mark Steinborn, manager of the UCI Research Machine Shop; and Professor Peter de Lijser, for his generous donation of a nanosecond transient absorption spectroscopy instrument that was modified for our work. My research was supported by following funding sources: Moore Inventor Fellowship

(GBMF grant #5641), Research Corporation for Science Advancement under a Cottrell Scholar Award (Award #24169), Nissan Chemical Corporation for sponsored research support, the U.S. Department of Energy Office of Science under an Early Career Research Program Award (DE-SC0019162), and the National Science Foundation CSDM-B (Grant #2101665).

I would like to thank the people in my life who were involved in my academic journey: Professor Claire Castro and Professor William Karney, my undergraduate research advisors, for offering me a research assistantship, mentorship in computational chemistry, and overall being great people; Gail Vinnacombe-Wilson, my undergraduate research partner and friend who supported me while acting as my academic rival; David Bass, my sports coach, employer, and life mentor who taught me technical skills and creative problem solving; and my friends from high school in San Francisco who were my academic getaway and indulged in my hobbies of anime, cosplay, and games, and were (and still are) largely my social support group.

Lastly, I would like to thank my parents, Steven and Michelle, for their major role in the person I am today. When I wanted something as a kid, despite a tight budget, you would try your best to deliver. When I had any social or academic anxiety, you would always be available with an open ear. When I was ecstatic about receiving a scholarship from my undergraduate institution and transitioned immediately to dejection when viewing the remaining cost of tuition, you never once showed doubt and only said “we will make it work”. From immigrating to America with an unsure future to taking care of a newborn while going to school WHILE working multiple jobs to support us, I would like to express my sincerest gratitude for your sacrifices made to date. Even if I seem aggravated or disinterested at times, I want you to know that I do, and always will, love you.

VITA

Simon Luo

2014-16	Undergraduate Research Assistant in Castro/Karney Research Group, University of San Francisco, San Francisco, CA.
2016	B.S. in Chemistry (ACS Certified)-Minor in Physics, University of San Francisco, San Francisco, CA.
2016-21	Graduate Research Assistant in Ardo Research Group, University of California, Irvine, Irvine, CA.
2021	Ph.D. in Chemistry, University of California, Irvine, Irvine, CA.

FIELD OF STUDY

Physical Chemistry

PUBLICATIONS

Luo, S., White, W., Cardon, J. M. & Ardo, S. Clarification of mechanisms of protonic photovoltaic action initiated by photoexcitation of strong photoacids covalently bound to hydrated Nafion cation-exchange membranes wetted by aqueous electrolytes. *Energy Environ. Sci.* (2021) doi:10.1039/D1EE00482D.

White, W., **Luo, S.**, Bhide, R., Sanborn, C. D., Baranov, M. S., Solntsev, K. M., Ardo, S. Evaluation of the role that photoacid excited-state acidity has on photovoltage and photocurrent of dye-sensitized ion-exchange membranes. in *Physical Chemistry of Semiconductor Materials and Interfaces XVIII* vol. 11084 12 (SPIE, 2019).

Luo, S., Kuhn, A. J., Castano, I., Castro, C. & Karney, W. L. Hydrogen Shifts in Aryl Radicals and Diradicals: The Role of m-Benzynes. *J. Org. Chem.* **83**, 314–322 (2018).

ABSTRACT OF THE DISSERTATION

Elucidation and Impact of Photoacid Proton-Transfer Regeneration Dynamics

by

Simon Luo

Doctor of Philosophy in Chemistry

University of California, Irvine, 2021

Associate Professor Shane Ardo, Chair

This dissertation focuses on the interrogation of the photoacid sensitization (Förster) cycle to understand mechanisms for light-to-protonic energy conversion. I define protonic species as those capable of undergoing proton-transfer reactions, including $H_2O(l)$, $H^+(aq)$, $OH^-(aq)$, and Brønstead–Lowry (conjugate) acids/bases. The central theme of this work is relating operating principles between traditional electronic photovoltaics (electron/holes) and protonic photovoltaics (OH^-/H^+) including charge carrier generation and conduction with the goal of developing design strategies for efficient light-to-ionic power conversion. This is achieved by investigating ground-state proton transfer processes in the Förster cycle using electrochemical and spectroscopic techniques and leveraging this knowledge to understand photo-initiated ion transport in ion-exchange membranes.

Transient absorption spectroscopy studies of aqueous photoacids provided insight into the protonic species generated during the Förster cycle and the inefficiencies of current state-of-the-art photoacids for generating large photoresponses in photoacid-modified ion-exchange membranes. An abundance of ultrafast spectroscopy data exist that revealed mechanistic details

for excited-state proton transfer, but there was limited information regarding the mechanisms for the subsequent ground-state proton transfer. Proton acceptance in the excited-state and proton donation in the ground-state from $H_2O(l)$ in the Förster cycle results in the transient generation of H^+ and OH^-, analogous to photogeneration of electrons and holes in electronic photovoltaics. An obstacle for realizing this ideal mechanism is kinetics. These were analyzed via a systematic study using various photoacids by varying the concentration of deprotonated photoacids and protons, photoacid ground-state acidity, solution acidity, and total photoacid concentration.

Photoacids were covalently bonded to ion-exchange membranes to assess the impact that their photochemical mechanisms had on their ability to exhibit photovoltaic action. Existing methodology for four-probe electrochemical measurements was revamped to produce reproducible signals and temporally stable baselines. The key factor was eliminating the introduction of external electrolyte from reference electrodes filled with saturated internal electrolyte by replacing those electrodes with reference electrodes immersed directly into the electrolyte in contact with the photoacid-modified ion-exchange membranes. This introduced experimental constraints that required physical modification of the experimental apparatus as well as deconvolution of the Nernst electrode potential from the membrane potential. Implementation of this new setup resulted in the observation of a “reverse” photovoltage, meaning that it was opposite in sign to photovoltages measured in traditional electronic photovoltaics and that observed in our group in all prior studies of these systems. A series of control experiments was performed, and a mechanism coined “electrolyte crossover induced bulk membrane polarization” was hypothesized to explain this reverse photovoltage.

Introduction

In 1954, researchers at Bell Labs demonstrated the first silicon p-n junction construct for conversion of photons to electrical power.[1] Advances since then have improved the energy conversion efficiency of p-n junction solar cells,[2] while identifying construct design strategies and knowledge of power generation mechanisms.[3,4] Although p-n junction solar cells are ubiquitous for solar to electric power conversion, they are most efficiently utilized when immediately driving an electrical load. For applications in desalination, electrical energy from a solar cell may be converted to ionic transport through the electrochemical generation of ionic species. Alternatively, direct photo-ionic energy conversion can be used to drive ionic transport without intermediate energy losses due to electrochemical generation of ionic species. Furthermore, the absence of components facilitating electron generation and transport allows tighter integration of photo-ionic devices applicable in mimicking biological processes. However, literature from others for the direct conversion of solar energy to ionic transport is sparse.[6–8]

Conversion of light into electricity through photogeneration of mobile charged species[9–11] is termed photovoltaic action. This process is efficient when species of one charge type are collected at a contact more rapidly, and thus more selectively, than species of the other charge type, which is a hallmark of current rectification.[4,12] Current rectification and sunlight absorption are important factors for effective photovoltaic action. Nearly all examples of photovoltaic action have used electronic semiconductors, because of their demonstrated ability to be fabricated into diodes that effectively rectify current.[13] Semiconductors that are ineffective visible-light absorbers use dye molecules to sensitize them to absorption of more solar photons.[14] Many examples of these dye-sensitized solar energy conversion devices exist.[15–17] The most common have dyes positioned at an interface between an inorganic semiconductor and a redox-active liquid electrolyte,[16] or

incorporated into a polymeric material and rely on exciton diffusion to reach interfaces and charge separate, such as in organic photovoltaics.[18,19]

Recently, our group reported an alternative dye-sensitized construct for conversion of visible light into useful power that did not rely on electronic mobile charged species or an interface for initial charge separation.[20–22] These composite materials consisted of a perfluorosulfonic acid (PFSA) ion-exchange membrane, like Nafion, with covalently bound derivatives of pyrenol-based reversible photoacid molecules, 8-hydroxypyrene-1,3,6-trisulfonylethylenediammonium (HPTSA), as dye sensitizers. *Unique to our efforts is that we used water as the protonic semiconducting medium.* Doping of the water semiconductor was achieved by infiltrating it into hydrophilic domains of the dopant-containing PFSA polymeric scaffold. Through its covalent modification, this scaffold, termed a "membrane-liquid junction assembly", prevented macroscopic transport of dopant functional groups and photoacid molecular dyes, while enabling generation of mobile H^+ and/or OH^- in the water semiconductor, predominantly due to thermal excitation of dopants and photochemical excitation of dyes. The work herein identifies tunable experimental parameters to manipulate ground-state proton transfer mechanisms in the Förster cycle while designing experimental techniques and setups to probe and quantify the resulting photogenerated protonic species.

Photoacids and photobases are molecules whose acidity varies depending on its electronic energy level. Photoacids can be categorized into two classes: reversible and irreversible, which describe their ability to conduct **Step 4** in the photosensitization cycle shown below. Often referred to as photoacid generators, *irreversible* photoacids are chemically unstable upon absorption of light and result in the generation of H^+(aq) as well as radicals and other side products. These are

often employed for photolithography to weaken or cure polymers and are used to remotely inject protons into an experimental system.

The photoacids used in our work are *reversible* photoacids, which can regenerate after undergoing photosensitization. These photoacids are often employed as fluorescent pH indicators, however, our work attempts to exploit the regenerative nature of this photosensitization cycle to mimic processes in dye-sensitized solar cells.

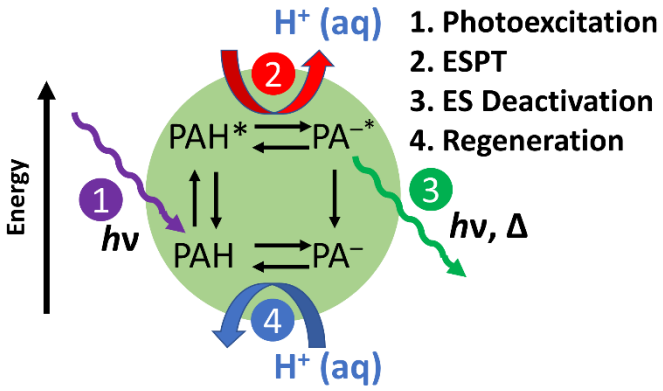

Figure 0.1. Scheme depicting the photoacid dye sensitization Förster cycle for excited-state proton transfer (ESPT) from HPTSA (PAH), including the predominant aqueous proton acceptor species ($H_2O(l)$) and proton donor species ($H^+(aq)$).

The photosensitization cycle describing the relationship between acidity (reflected as pK_a values) and electronic energy level, referred to as the Förster cycle, represents a thermodynamic square scheme for photo-induced proton transfer that is used to approximate the Brønsted–Lowry acidity of reversible photoacids and photobases in their ground state and excited state.[23] Absorption of visible light (**Step 1**) by a photoacid results in a shift in its electron density away from the protic bond, weakening the bond strength of the protic bond which increases the thermodynamic favorability for deprotonation in its electronic excited state.[24] Kinetically, excited-state proton transfer (**Step 2**) is able to occur only when the excited-state lifetime is longer than the time it takes to transfer a proton directly to solvent to form $H^+(aq)$, or directly to $OH^-(aq)$ to form H_2O. After excited-state proton transfer, a separate electronic relaxation of the photoacid from the excited state to the ground state occurs (**Step 3**), resulting in radiative and/or non-radiative emission and formation of the photoacid conjugate base, contrasting with immediate relaxation to

the oxidized ground state in dye-sensitized solar cells after excited-state electron transfer. Ultimately, the conjugate base is reprotonated by H^+(aq), or by H_2O to form OH^-(aq) (**Step 4**). Overall, this sensitization cycle utilized absorbed photons to generate mobile protonic charged species.

Chapter 1 describes the transient spectroscopic study of pairwise ground-state proton transfer between water, protonic species, and aqueous photoacid species. The observed ground-state reprotonation rate constant, or the inverse characteristic amount of time before the photogenerated mobile charge carrier recombines with the photoacid, was manipulated by changing the concentration of reactants in the ground-state reprotonation reaction. Modeling the experimental data to kinetic models allows for the inference of the proton donor for ground-state reprotonation, giving insight into the speciation of the photogenerated protonic species. Following work incorporates additional proton donor species to introduce competing ground-state reprotonation reactions, allowing for the photogeneration of protonic species unrelated to water.

Chapter 2 describes attempts to quantify steady-state net photochemical generation of protonic species electrochemically. The development of an optically transmissive electrochemical proton sensor based on the reversible hydrogen electrode half-reaction is described. Revisions of the sensor produced photoeffects largely dominated by mechanisms unrelated to proton sensing requiring mobile and immobile aqueous photoacids to identify the source of these photoeffects. Lastly, a similar setup for detection of photogenerated protonic species by a former Ardo Group member is discussed.

Chapter 3 focuses on the photoelectrochemical investigation of membrane-liquid junction assemblies. The experimental setup, pioneered by my predecessors for measurements of bipolar membrane assemblies, was adapted and revised for measurements of membrane-liquid junction

assemblies. Experimental considerations with the new setup are described and rationalized. Most notably, substitution of reference electrodes imposed constraints that complicated the experimental setup and post-analysis of data but improved baseline stability and repeatability of photoresponses in membrane-liquid junction assemblies. A suite of photoelectrochemical experiments in conjunction with knowledge of proton transfer mechanisms within the Förster cycle offer new insight to the operating mechanism of membrane-liquid junction assemblies.

Chapter 1: Transient Spectroscopic Investigation of Ground-State Proton Transfers in Aqueous Photoacids

In efficient photochemical energy conversion devices, photoexcitation results in a change in the concentration of at least two chemical species. Photo-induced processes that occur after light is absorbed by semiconductors and electron-transfer dye sensitizers are well known. In traditional crystalline electronic semiconductors, the extent of occupancy of both conduction-band states (electrons) and valence-band states (holes) change under illumination, while in dye-sensitized solar cells, illumination results in a change in the concentration of semiconductor charged species and in the speciation of redox-active molecules in the liquid electrolyte. Analogous to this, ionic solar cells also benefit from exhibiting a light-driven change in the concentration of two mobile charged species, notably H^+(aq) and OH^-(aq) for protonically semiconducting water. This process is enabled through use of photoacids or photobases, which under specific conditions are hypothesized to generate both H^+(aq) and OH^-(aq) as an outcome of the dye sensitization Förster cycle (**Figure 0.1**).[25] It includes several assumptions that limit its applicability for some excited-state proton transfer reactions, such as it assumes that kinetics of proton transfer do not limit excited-state behavior, which is a reasonable assumption for 8-hydroxypyrene-1,3,6-trisulfonic acid (HPTS) and its analogs.[26]

While the Förster cycle serves as a dye-centric representation of the protonation states of photoacidic and photobasic dyes, it does not indicate the transient speciation of protonic species, which is critical in assessing the ability of a dye to exhibit substantial protonic photovoltaic action. While it is well-known that photoexcitation of photoacids, like HPTS and its analogs, result in photogeneration of H^+(aq) from their excited states,[27] less is known about the protonic speciation

that occurs upon regeneration of the ground-state conjugate base of photoacids through reprotonation, via the following reactions,

$$PA^-(aq) + H_2O(l) \underset{k_{-1}}{\overset{k_{+1}}{\rightleftarrows}} PAH(aq) + OH^-(aq) \quad (1.1)$$

$$PA^-(aq) + H^+(aq) \underset{k_{-2}}{\overset{k_{+2}}{\rightleftarrows}} PAH(aq) \quad (1.2)$$

where $PA^-(aq)$ and $PAH(aq)$ stand for ground-state deprotonated and protonated photoacids, respectively. When $H_2O(l)$ is the proton donor, $OH^-(aq)$ is formed, which is desired to obtain substantial photovoltages. However, when $H^+(aq)$ is the proton donor then the sensitization cycle produces no net chemical species, suggesting that the photovoltaic effect will be quite small, although nonzero.[28] As such, we utilized transient absorption spectroscopy to quantify and analyze the reaction kinetics and overall behavior of the ground-state reprotonation reaction of HPTSA, a polymer linkable photoacid, HPTS and 1-naphthol-5-sulfonic acid ($NaphSO_3$).

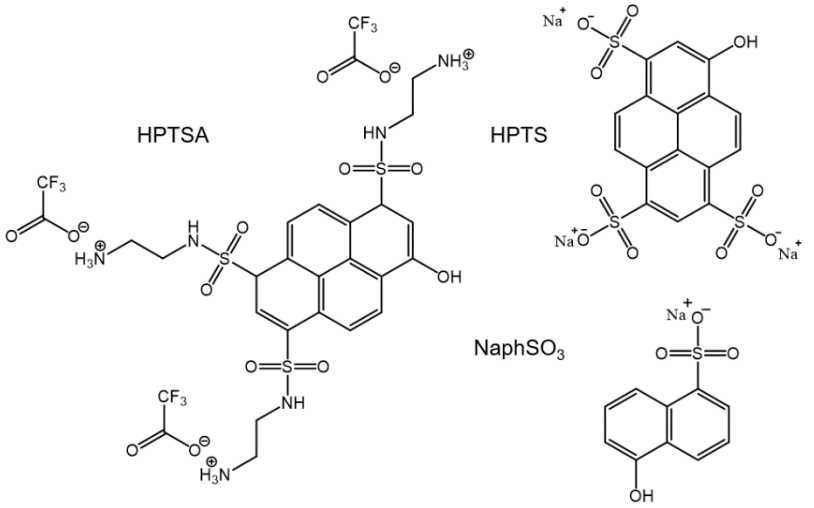

Figure 1.1. Chemical structures of photoacids 8-hydroxypyrene-1,3,6-tris(2-aminoethylsulfonamide) (HPTSA) 8-hydroxypyrene-1,3,6-trisulfonic acid (HPTS) and 1-naphthol-5-sulfonic acid ($NaphSO_3$).

Chapter 1.1: Empirical Determination of Ground-State and Excited-State Acidity

The relevant parameters of photoacids and photobases include the ground-state acidity (pK_a) and observed excited-stated acidity (pK_a*). Characterization of these parameters can be achieved by spectroscopically probing the protonation states of the ground-state and excited-state photoacid species. Differences in electronic absorption spectra reveal speciation of ground-state photoacid species while differences in photoluminescence spectra reveal speciation of excited-state photoacid species, enabling acid–base titrations to reveal information about the speciation of the two states and thus information about pK_a and pK_a*. These data can be accurately analyzed using the Henderson-Hasselbalch equation,

$$pH = pK_a + \log\frac{[PA^-]}{[PAH]} \tag{1.3}$$

where [PA^-] and [PAH] are the equilibrium concentrations of the deprotonated and protonated photoacid species respectively. From the Henderson-Hasselbalch (**Equation 1.3**), it is possible to convert from a ratio of protonated and deprotonated photoacids to a relationship involving the mole fraction of a particular protonation state,

$$[PAH]_{total} = [PAH] + [PA^-] \tag{1.4}$$

$$pH = pK_a + \log\frac{[PA^-]}{[PAH]_{total} - [PA^-]} \tag{1.5}$$

$$\frac{[PA^-]}{[PAH]_{total}} = \frac{1}{1+10^{(-pH+pK_a)*n}} \tag{1.6}$$

where $[PAH]_{total}$ is the total concentration of photoacid species and n is a stretch parameter added to incorporate non-ideality into fits of the titration data and is typically observed to be $|n| < 1$. Stretch parameter of non-unity magnitude is consistent with the molecules existing in

environments that are more heterogenous than expected in bulk solution, where typically $|n| \approx 1$. Values of $|n| < 1$ is indicative of repulsive interactions between PA^-(aq) and H^+(aq) with the addition of more H^+(aq), while $|n| > 1$ is indicative of attractive interactions between PA^-(aq) and H^+(aq) with the addition of more H^+(aq). **Equation 1.6** is a convenient form of **Equation 1.3** for identifying the acidity of a buffer based on the distribution of its protonation state. From the Beer-Lambert Law (**Equation 1.7**), the observable absorbance can be directly converted to concentration,

$$A = \varepsilon bc \tag{1.7}$$

where A is absorbance, ε is the molar decadic absorption coefficient, b is the pathlength of the sample, and c is concentration. The total concentration of photoacids can be normalized to the difference in absorption between the purely protonated and deprotonated photoacids for a given wavelength, resulting in the final form of the **Equation 1.6**,

$$I(pH, \lambda) = \frac{I_f(\lambda) - I_0(\lambda)}{1 + 10^{(-pH + pKa)*n}} + I_0(\lambda) \tag{1.8}$$

where I is the absorbance, I_0 is the initial absorbance when purely in a protonation state, and I_f is the final absorbance when the photoacid is completely converted to the other protonation state. **Equation 1.8** can also be applied to acid–base titration measurements of photoluminescence in optically dilute samples, which reports on the observed excited-state acidity of the photoacid, since the luminescence intensity is also directly proportional to concentration of excited-state species. For photoacids with low pK_a*, the typical pH scale may be insufficient to gauge a_{H+} in solution. Alternative, the Hammett acidity function, H_0, is used instead as a measure of effective acidity in concentrated acid solutions and is not related to the concentration of H^+ present.[29] Prior literature measuring H_0 for the titrant (HCl in this work)[30,31] as a function of concentration can be referenced,

but a best-fit line was reported by Dr. Christopher D. Sanborn, assembled from prior literature of H_0 values for HCl, and is reproduced below.[32]

$$H_0 = -0.3763445 * [HCl] + 0.09397265 \quad (1.9)$$

Maintaining an ionic strength is impractical and sometimes impossible due to the low pH needed to observe protonated photoacid emission. When photoluminescence measurements are compared from samples varying greatly in ionic strength, it is necessary to make luminescence intensity corrections to account for photons that were not able to fall on the detector due to changes in refractive index dictated by the following equation,[23]

$$I_{cor} = I_{obs} \frac{{n_{salt}}^2}{{n_{ref}}^2} \quad (1.10)$$

where I_{cor} and I_{obs} is the corrected and observed luminescence intensity respectively, and n_{salt} and n_{ref} is the refractive index of the solution to be corrected and a reference solution. Typically, the referenced refractive index is that of water (n = 1.333), which is applicable for solutions with low ionic strength. Look up tables for the refractive index of the titrant (HCl for this work)[33] as a function of concentration is used to calculate the refractive index of the high ionic strength solution.

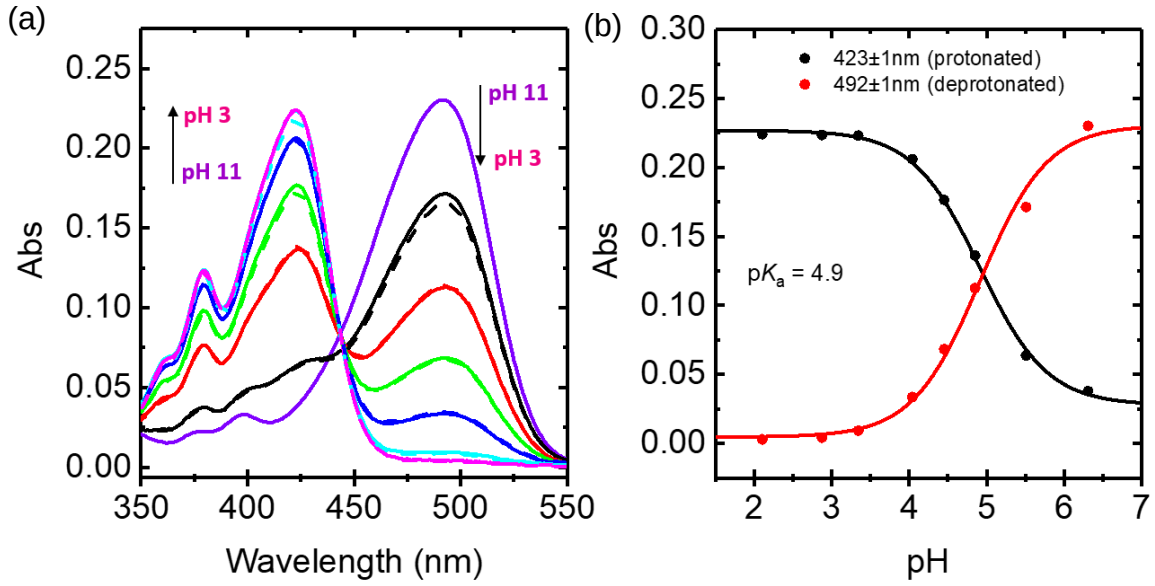

Figure 1.2. **(a)** Electronic absorption spectra of aqueous HPTSA solutions with 1 mM ionic strength at different pH values before (solid line) and after (dash line) transient absorption spectroscopy measurements. **(b)** Absorbance at the wavelength of maximum absorbance for protonated and deprotonated HPTSA (λ_{max} = 423 nm and 492 nm, respectively) as a function of pH with global non-linear least-squares best fit of both datasets to the Henderson-Hasselbalch equation (**Equation 1.8**). Transient absorption spectroscopy data was not reported for conditions at pH < 3, due to indistinguishability between the data and photoluminescence signals, or pH > 6, due to the inaccuracy of the pseudo-first-order approximation for H^+(aq) because of the large initial concentration of ground-state deprotonated HPTSA and poor signal-to-noise ratio.

Ground-state reprotonation kinetics of HPTSA as a function of proton concentration. The ground-state pK_a of HPTSA was confirmed to be about 4.9 which we determined using an acid–base titration procedure with spectrophotometric detection (**Figure 1.2**) described in **Chapter 1.1** and **Chapter 1.4**, and is consistent with values reported previously.[34] Changes in absorbance, each with near-maintenance of an isosbestic point at 443 nm, is consistent with a single titration of a protic functional group. Time-resolved spectroscopic data for HPTSA (**Figure 1.3**) suggest sub-nanosecond photogeneration of ground-state deprotonated photoacids via **Steps 1 – 3** in **Figure 0.1**, followed by slower nanosecond-to-microsecond regeneration of ground-state deprotonated photoacids via **Step 4** in **Figure 0.1**. Consistent with **Step 4**, the transient absorption growth at 480 nm and bleach at 420 nm correspond to near-stoichiometric generation of ground-state

deprotonated HPTSA and loss of ground-state protonated HPTSA, respectively (**Figure 1.3a**). Transient absorption spectroscopy data over time follow a kinetic rate law that is first order in the concentration of deprotonated photoacids (**Figure 1.3b-f**) and depend significantly on the pH of the solution, with an observed rate constant that is directly correlated with the activity of H^+(aq), a_{H+}, and with pH defined as "–log a_{H+}." The range of pH values investigated was limited to ~3 – 6 because at pH ≤ 3, transient absorption spectroscopy kinetics due to ground-state reprotonation were indistinguishable from photoluminescence kinetics, suggesting that the rate of **Step 4** was similar to, or faster than, the rate of **Step 3**. Because protonated HPTSA is required to undergo the Förster cycle, the maximum pH used of 5.5 was limited by the pK_a of HPTSA. The slowest measured regeneration process occurred at pH = 5.5 and was apparent on the timescale of 10 µs. While at first it may seem unexpected that protonation of a deprotonated molecule in water would require such a long time, this observation is completely consistent with prior observations of proton-transfer processes to and from water.[35–37] Although proton transfer from H^+(aq) to ground-state deprotonated HPTSA is thermodynamically favored with a rate constant that is approximately diffusion limited, mass action applied to **Reaction 1.2** indicates that the bimolecular rate can be quite slow at pH ≥ 5 due to the presence of $\leq 10^{-5}$ M H^+(aq). Moreover, because H_2O(l) has pK_a = 14, protonation of species with pK_a < 14, such as HPTSA, via **Reaction 1.1** is thermodynamically unfavored, thus requiring a kinetic barrier at least as large as the standard Gibbs free energy difference between deprotonation of HPTSA and water, ΔG^o, as follows,

$$\Delta G^{\ddagger}_{min} \geq \Delta G^o = 2.303\, RT\, \Delta pK_a \tag{1.11}$$

where $\Delta G^{\ddagger}_{min}$ is the minimum activation Gibbs free energy and ΔpK_a is the difference in acidity between ground-state HPTSA and water. Given that $pK_a \approx 5$, regeneration of ground-state deprotonated HPTSA through deprotonation of water should be quite slow (>100 µs) even if one

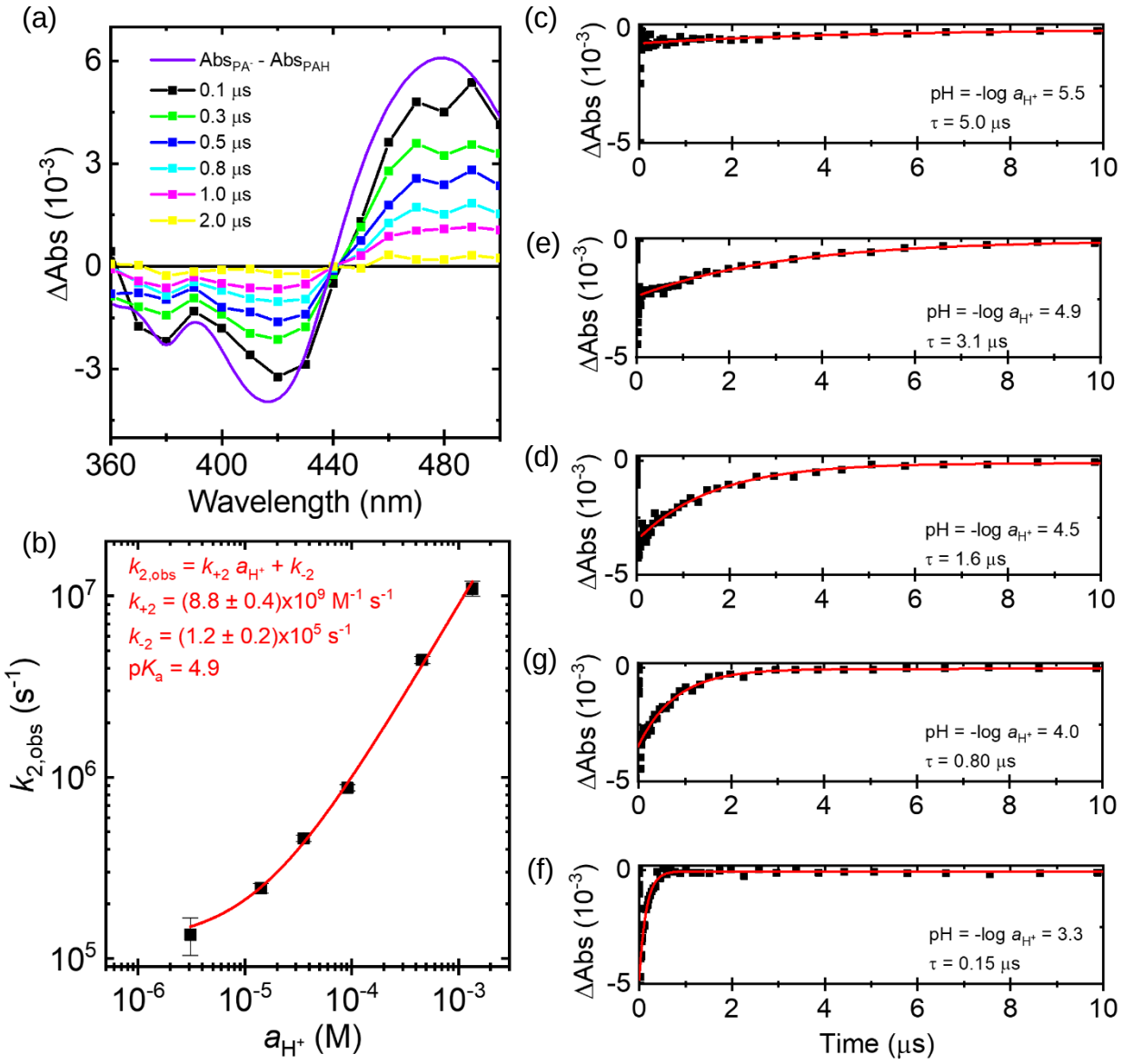

Figure 1.3. Transient absorption spectroscopy data for HPTSA dissolved in aqueous electrolytes after 355 nm pulsed-laser excitation (0.6 mJ/pulse): **(a)** Transient absorption spectra that resolve the ground-state reprotonation of deprotonated HPTSA. **(b)** Log–log plot of the observed rate constants as a function of the proton activity (a_{H+}) and a linear least-squares best-fit to obtain the values shown for the second-order rate constant for reprotonation, k_{+2}, and first-order rate constant for deprotonation, k_{-2}. The observed rate constants were determined from non-linear least-squares best fits of the transient absorption spectroscopy data at 420 nm shown in **panels c – f** to a single-exponential decay function with a variable long-time value. Error bars shown in **panel b** represent the standard error of the mean of the pseudo-first-order rate constants from the non-linear least-squares best fits.

assumes a barrierless back reaction and the fastest frequency factor possible of ~10^{13} s^{-1}. Because our transient absorption spectroscopy signals persisted for an order-of-magnitude less time than this projected lower-limit time constant, it is unlikely that desired **Reaction 1.1** is operative during the dye sensitization Förster cycle for HPTSA(aq).

Kinetic data for the reprotonation of ground-state deprotonated HPTSA(aq) were analyzed in order to obtain both the forward and backward rate constant for ground-state proton transfer with H^+(aq) (**Reaction 1.2**). The integrated rate equation for an analogous process has been reported previously,[38] but for clarity, we show the derivation here for our specific case, which starts with the following differential rate equation,

$$\frac{d[\mathrm{PA}^-]}{dt} = -k_{+2}[\mathrm{PA}^-][\mathrm{H}^+] + k_{-2}[\mathrm{PAH}] \tag{1.12}$$

where k_{+2} is the rate of proton association, k_{-2} is the rate of proton dissociation, [PA^-] and [PAH] are the concentration of ground-state deprotonated/protonated photoacids, respectively, and [H^+] is the concentration of free (unbound) protons. Due to the dilute conditions used in this experiment, activity coefficients for each species are reasonably assumed to be unity. Although reaction rates are dependent on the concentration of protons and photoacid species, our transient absorption spectroscopy measurements only report on the change in concentration of ground-state deprotonated photoacids generated from pulsed-laser excitation, such that **Equation 1.12** can be recast as follows,

$$\frac{d\left(\mathbf{[PA^-]_{eq}}+\mathbf{\Delta[PA^-]_t}\right)}{dt} = -k_{+2}[\mathrm{PA}^-]_t\left([\mathrm{H}^+]_{\mathrm{eq}} + \mathbf{\Delta[H^+]_t}\right) + k_{-2}\left(\mathbf{[PAH]_{eq}} + \mathbf{\Delta[PAH]_t}\right) \tag{1.13}$$

where the $[X]_{eq}$, $\Delta[X]_t$, and $[X]_t$ are written as such to indicate the equilibrium concentration, transient non-equilibrium change in concentration, and transient non-equilibrium total

concentration, respectively. Colors and bold text are used to clarify subsequent substitutions using the following conservation of mass relation (**Equation 1.14**), the fact that experiments were conducted under conditions where a negligible concentration of H^+(aq) was photogenerated relative to its equilibrium concentration (**Equation 1.15**), and the equilibrium expression that results from setting $\frac{d[\mathrm{PA}^-]}{dt}$ equal to zero in **Equation 1.12** (**Equation 1.16**),

$$\boldsymbol{\Delta[PA^-]_t} = [\mathrm{PA}^-]_t - \boldsymbol{[PA^-]_{eq}} = -\boldsymbol{\Delta[PAH]_t} \tag{1.14}$$

$$[\mathrm{H}^+]_t \approx [\mathrm{H}^+]_{\mathrm{eq}}, \text{ and thus } \boldsymbol{\Delta[H^+]_t} \approx 0 \tag{1.15}$$

$$k_{-2}\boldsymbol{[PAH]_{eq}} = k_{+2}\boldsymbol{[PA^-]_{eq}}\boldsymbol{[H^+]_{eq}} \tag{1.16}$$

Substituting these equations into **Equation 1.13** leads to the following,

$$\frac{d[\mathrm{PA}^-]_t}{dt} = \left(-k_{+2}[\mathrm{PA}^-]_t\boldsymbol{[H^+]_{eq}} + 0\right) + \left(k_{+2}\boldsymbol{[PA^-]_{eq}}\boldsymbol{[H^+]_{eq}} - k_{-2}[\mathrm{PA}^-]_t + k_{-2}\boldsymbol{[PA^-]_{eq}}\right) \tag{1.17}$$

$$\int_{[\mathrm{PA}^-]_{\mathrm{eq}} + \Delta[\mathrm{PA}^-]_{\mathrm{o}}}^{[\mathrm{PA}^-]_{\mathrm{eq}} + \boldsymbol{\Delta[PA^-]_t}} \frac{1}{-(k_{+2}\boldsymbol{[H^+]_{eq}} + k_{-2})[\mathrm{PA}^-]_t + (k_{+2}\boldsymbol{[H^+]_{eq}} + k_{-2})\boldsymbol{[PA^-]_{eq}}} d[\mathrm{PA}^-]_t = \int_0^t dt \tag{1.18}$$

where subsequent substitution using the following four relations, $c = [\mathrm{PA}^-]_{\mathrm{eq}}$; $y_t = c + \Delta[\mathrm{PA}^-]_t$; $y_{\mathrm{o}} = c + \Delta[\mathrm{PA}^-]_{\mathrm{o}}$; $k_{\mathrm{obs}} = k_{+2}[\mathrm{H}^+]_{\mathrm{eq}} + k_{-2}$, $y = [\mathrm{PA}^-]_t$, leads to the following integrated rate equations,

$$-\frac{1}{k_{\mathrm{obs}}}\int_{y_{\mathrm{o}}}^{y_t} \frac{1}{y-c} dy = -\frac{1}{k_{\mathrm{obs}}} \ln\left(\frac{y_t - c}{y_{\mathrm{o}} - c}\right) = t \tag{1.19}$$

$$y_t - c = (y_{\mathrm{o}} - c)e^{-k_{\mathrm{obs}}t} \tag{1.20}$$

$$\Delta[\mathrm{PA}^-]_t = \Delta[\mathrm{PA}^-]_{\mathrm{o}}\, e^{-(k_{+2}[\mathrm{H}^+]_{\mathrm{eq}} + k_{-2})t} \tag{1.21}$$

This resulting equation implies that transient absorption spectroscopy kinetic data obtained from photoacids that undergo **Reaction 1.2** should be fit well by a single decaying exponential function, as observed in **Figure 1.3**, with an observed rate constant, k_{obs}, represented by **Equation 1.22**.

$$k_{obs} = k_{+2} \cdot a_{H+} + k_{-2} \quad (1.22)$$

The coincidence of the linear least-squares best fit to the data shown in **Figure 1.3b** suggests that reprotonation of HPTSA is pseudo-first order, because a_{H+} changes little during the experiment given the low energies used for pulsed-laser excitation, which is consistent with transient absorption spectroscopy studies reported previously for HPTS.[36] Best fits to **Equation 1.22** not only enable one to obtain the second-order rate constant for reprotonation of ground-state HPTSA from the slope of the best-fit line, $k_{+2} = 8.8 \pm 0.4 \times 10^9$ M^{-1} s^{-1}, but also the first-order rate constant for deprotonation of ground-state HPTSA from the y-intercept of the best-fit line, $k_{-2} = 1.2 \pm 0.2 \times 10^5$ s^{-1}. The calculated value of k_{+2} is consistent with diffusion-limited recombination between H^+(aq) and a somewhat bulky proton-accepting molecule,[39] and the ratio of the rate constants equals K_a, and thus predicts a pK_a value of 4.9, which is consistent with the pK_a value obtained from measurements using a standard acid–base titration procedure (**Figure 1.2**). Data obtained at pH values significantly greater than the pK_a of HPTSA were excluded from the best fit to **Equation 1.22**, because the presence of large equilibrium concentrations of deprotonated HPTSA and large pH values resulted in deviations from the pseudo-first-order approximation for H^+(aq) and resulted in data that did not fit the trend.

An alternative explanation for **Equation 1.22** being able to sufficiently fit the data shown in **Figure 1.3b** is that both **Reactions 1.1 and 1.2** are operative, and that nearly all photoacids are protonated prior to pulsed-laser excitation. This would result in an expression for k_{obs} that is identical in form to that of **Equation 1.22**. However, this is not the case herein because ground-state absorption spectra clearly indicate that up to 80% of HPTSA are deprotonated in their ground state at the largest pH value studied of 5.5 (**Figure 1.2**). Moreover, based on the calculated pK_a value of HPTSA (4.9) and the pK_a of H_2O (14), the largest possible value for the rate constant of

Reaction 1.1 in the forward direction, k_{+1}, calculated using **Equation 1.11** and the lower-limit time constant (>100 μs)$^{-1}$, is at least one order-of-magnitude smaller than the y-intercept of the best-fit line in **Figure 1.3b**.

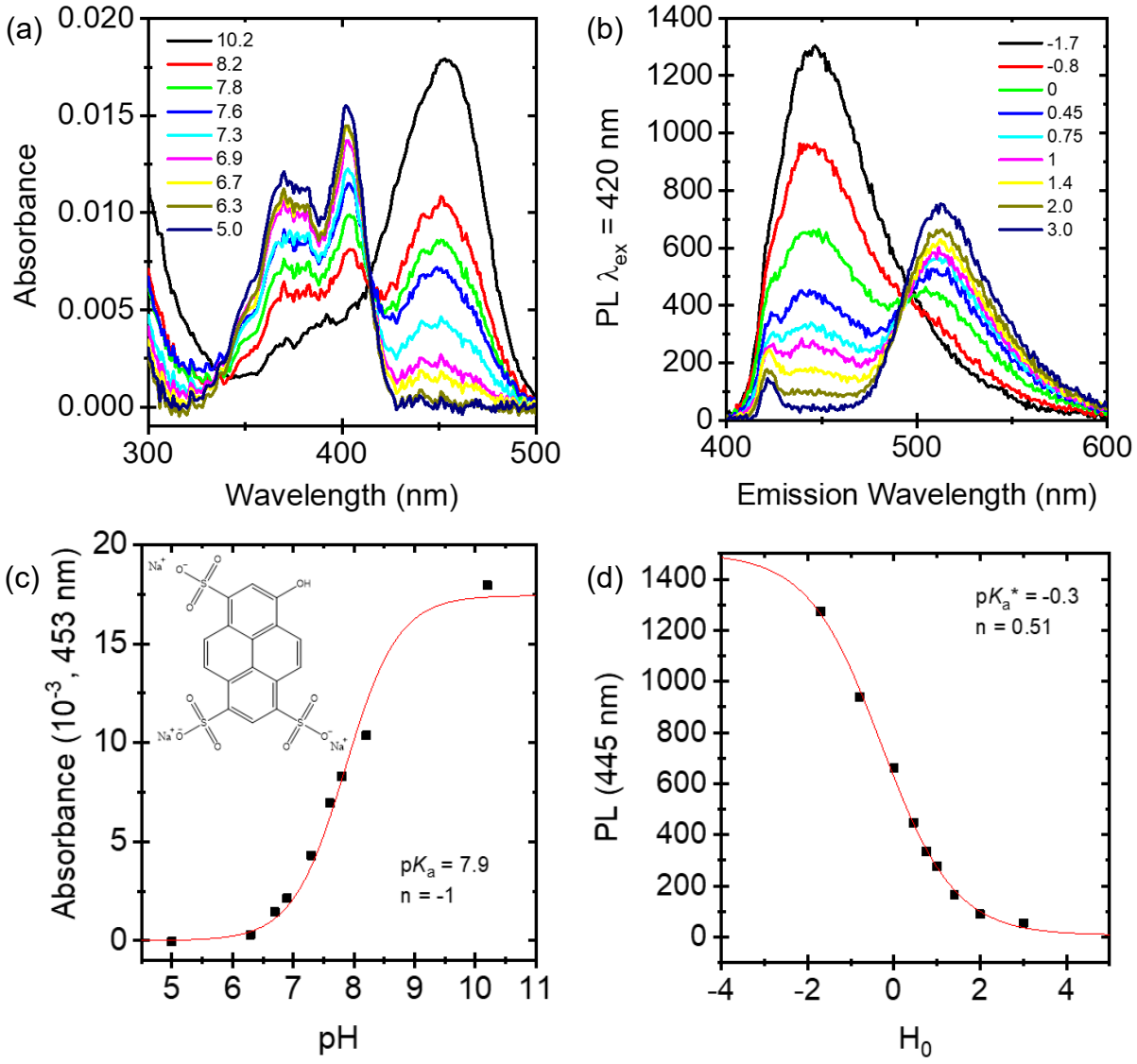

Figure 1.4. **(a)** Absorption (1 mM ionic strength) and **(b)** photoluminescence spectra of 10 μM HPTS under various solution acidities. Photoluminescence data for highly acidic samples (H_0 < 0) were corrected for differences in refractive indexes. **(c)** Absorbance at 453 nm and **(d)** photoluminescence of protonated (445 nm) HPTS as a function of pH. Non-linear least-squares best fits of the Henderson-Hasselbalch equation (**Equation 1.8**) are used to determine pK_a and pK_a*.

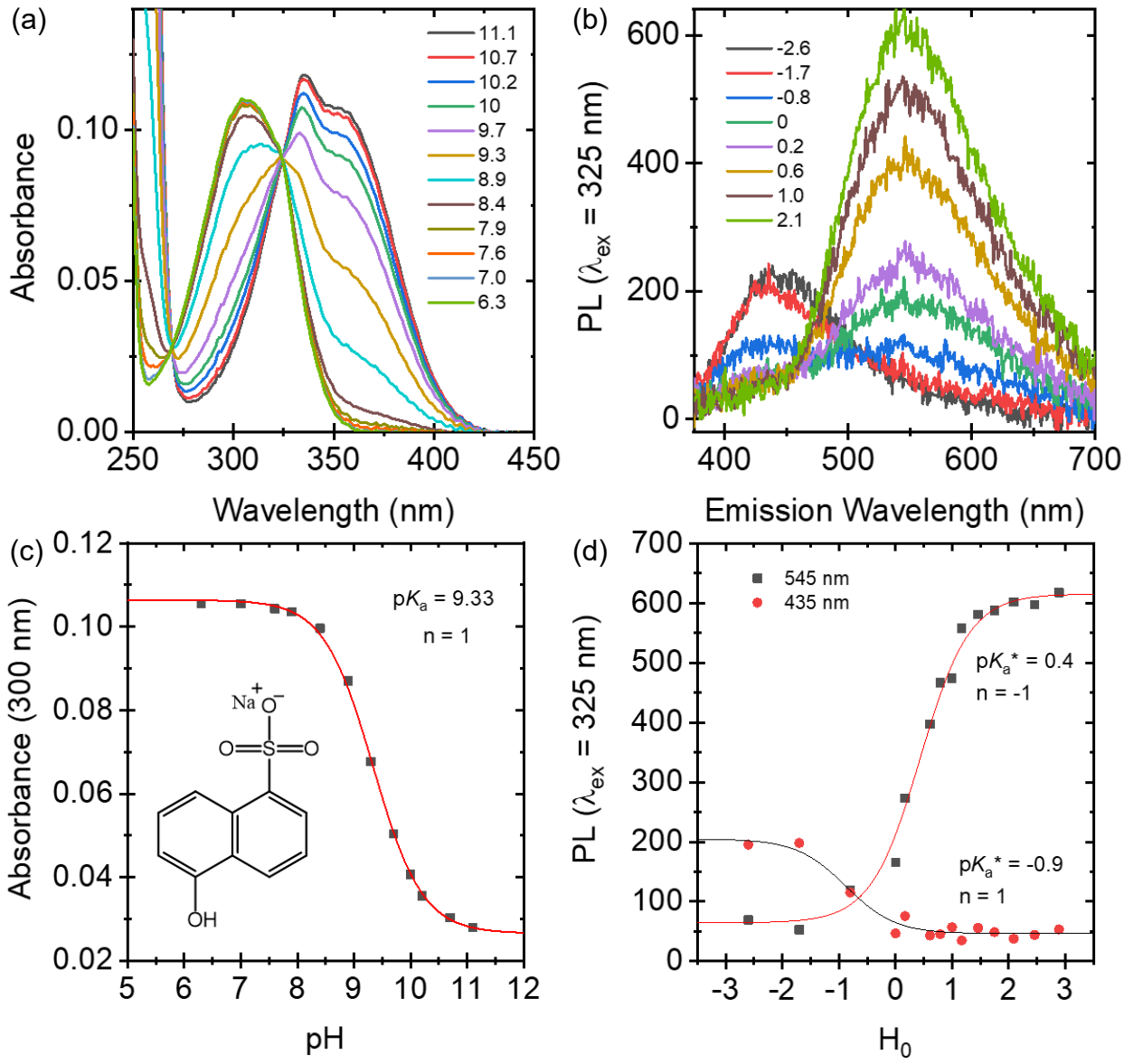

Figure 1.5. **(a)** Absorption (1 mM ionic strength) and **(b)** photoluminescence spectra of 27 μM $NaphSO_3$ under various solution acidities. Photoluminescence data for highly acidic samples ($H_0 < 0$) were corrected for differences in refractive indexes. **(c)** Absorbance at 300 nm and **(d)** photoluminescence of protonated (435 nm) and deprotonated (545 nm) $NaphSO_3$ as a function of pH. Non-linear least-squares best fits of the Henderson-Hasselbalch equation (**Equation 1.8**) are used to determine pK_a and pK_a^*.

Ground-State reprotonation kinetics of HPTS and $NaphSO_3$ as a function of proton concentration.

Acid–base titrations of aqueous solutions of HPTS ($NaphSO_3$) confirmed that the ground-state pK_a value was about 7.9 (9.3) (**Figure 1.4a,c and 1.5a,c**). Changes in absorbance and photoluminescence spectra, each with near-maintenance of an isosbestic point at 414 nm and 494 nm for HPTS (270 nm and 325 nm for $NaphSO_3$), are consistent with a single titration of a protic

functional group. The ground-state pK_a and observed approximate excited-state pK_a, pK_a*, of HPTS ($NaphSO_3$) were determined by non-linear least-squares fitting of the absorbance and photoluminescence data, respectively, at the peak wavelength characteristic of the protonated and deprotonated forms of HPTS ($NaphSO_3$) as a function of solution pH to the Henderson-Hasselbalch equation (**Equation 1.6**). The ability for a photoacid to conduct excited-state proton transfer is inferred from measurements of photoluminescence from the excited-state protonated and deprotonated photoacid species, at 445 nm and 510 nm respectively for HPTS (435 nm and 545 nm respectively for $NaphSO_3$), assuming all photoacids existed in the ground-state protonated form before excitation, which is a reasonable assumption because all pH values explored were well below the pK_a of their respective photoacids (**Figure 1.4b,d and 1.5b,d**). Best-fits for HPTS resulted in pK_a = 7.9 and pK_a* = -0.3. Although $|n| < 1$ was observed, prior titrations of analogous photoacid HPTSA resulted in similar observations,[34] suggesting the addition of concentrated titrant results in repulsive interactions or higher ionic strength increases the pK_a*. The unity value for *n* in $NaphSO_3$ suggests the size and/or number of charged functional groups is responsible for this observation in HPTS/HPTSA. Best-fit values for $NaphSO_3$ resulted in pK_a = 9.3 and two different pK_a*, 0.4 and -0.9. Separate modeling of the Henderson-Hasselbalch equation at 435 nm and 545 nm corresponding to protonated and deprotonated $NaphSO_3$ did not yield a single pK_a* value. The lack of a single isoemissive point suggests there is more than one chemical transition during the titration. This may be explained by a non-radiative encounter complex between deprotonated $NaphSO_3$ and H^+, most prominently demonstrated during the titration from pH 2 to 0 where the deprotonated emission peak (545 nm) decreases without a growth in the protonated emission peak (435 nm). Regardless, the range of pK_a* observed for $NaphSO_3$ suggests the excited-state proton acceptor is H_2O(l), an excited-state proton transfer mechanism the same to that of HPTS.

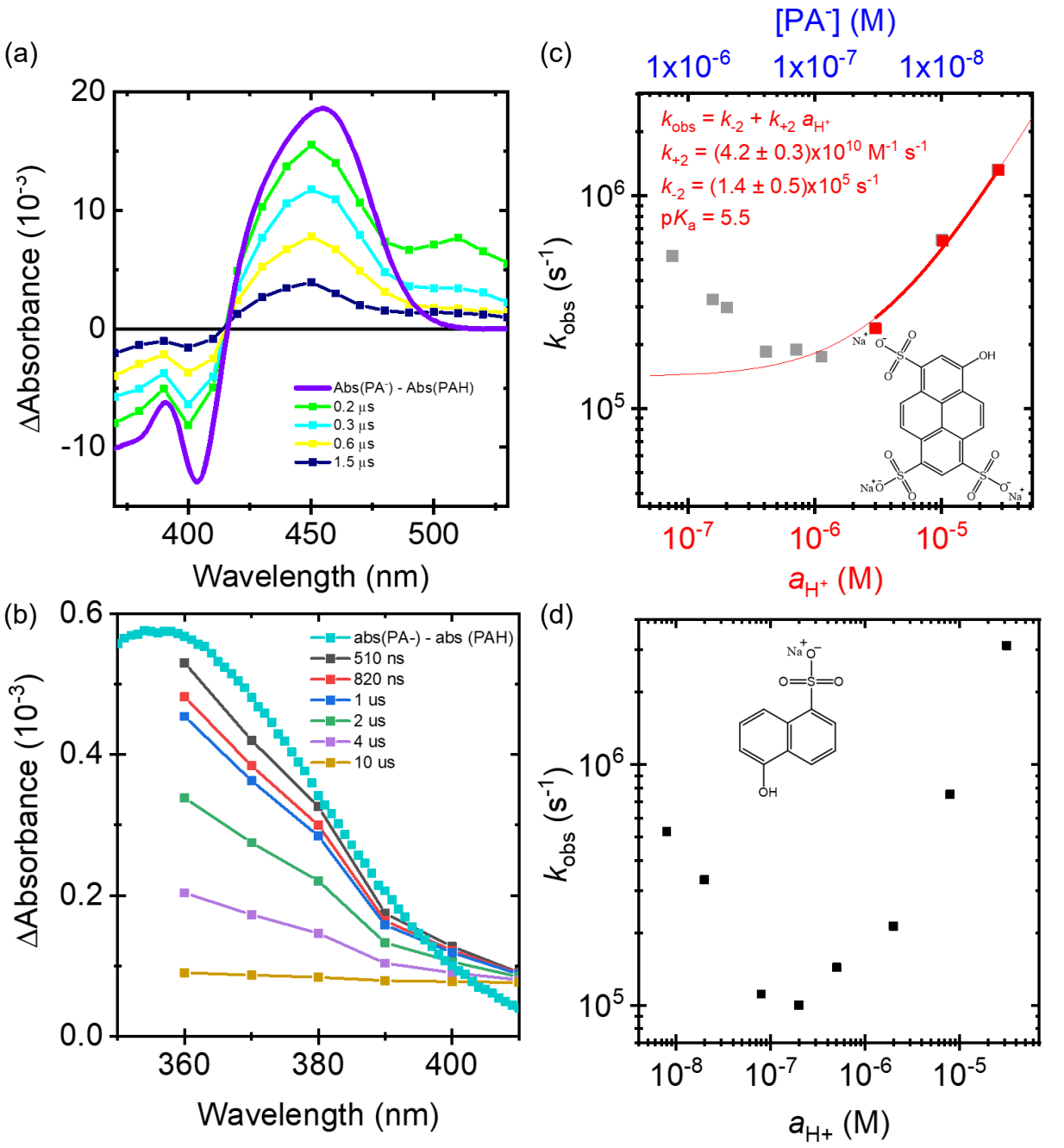

Figure 1.6. Transient absorption spectroscopy data for 10 µM HPTS dissolved in aqueous electrolytes after 355 nm pulsed-laser excitation (1.0 mJ/pulse, Full spectra; 0.5 mJ/pulse, varied pH) and 251 µM $NaphSO_3$ with 10 mM ionic strength dissolved in aqueous electrolytes after 355 nm pulsed-laser excitation (0.2 mJ/pulse, Full spectra/varied pH). Transient absorption spectra that resolve the ground-state reprotonation of deprotonated **(a)** HPTS and **(b)** $NaphSO_3$. Estimated observed rate constants obtained from non-linear least squares fitting of an exponential decay as a function of solution acidity for **(c)** HPTS at 450 nm and **(d)** $NaphSO_3$ at 370 nm. **Panel c** contains additional insight into the concentration of deprotonated HPTS at given acidities and has a non-linear least squares fit for data in the pseudo-first order regime for H^+ as described by **Equation 1.22**.

Time-resolved spectroscopic data of HPTS and $NaphSO_3$ showed resolvable mechanisms similar to that seen in HPTSA: deprotonated photoluminescence with lifetimes of tens of nanoseconds followed by ground-state reprotonation occurring on the microsecond timescale. The growth and bleach in the transient absorption spectrum at 450 nm and 400 nm for HPTS, respectively, (growth at 360 nm for $NaphSO_3$) correspond to changes in the steady-state absorption spectrum upon stoichiometric generation of ground-state deprotonated HPTS ($NaphSO_3$) from loss of ground-state protonated HPTS ($NaphSO_3$) (**Figure 1.6a,b**). An additional growth is observed at 510 nm for HPTS but the mechanism corresponding to the growth and its implications will be discussed later. Kinetic data probed as a function of pH at the maximum change in absorbance for protonated HPTS, 450 nm, ($NaphSO_3$, 370 nm) were best-fitted to an exponential decay to gauge the observed ground-state reprotonation rate constant, k_{obs}. which is dependent on the pH of the solution, revealing three distinct kinetic regimes for ground-state reprotonation: (1) pseudo-first-order kinetics in $[H^+]$ (kinetically modeled by **Equation 1.22**), (2) near-equal-concentration second-order kinetics in $[H^+]$ and $[PA^-]$, and (3) pseudo-first-order kinetics in $[PA^-]$.

Although **Equation 1.22** was used to fit ground-state reprotonation kinetics for HPTSA (**Figure 1.3b**, pK_a = 4.9), the same model is not adequate to fit reprotonation kinetics for photoacids with larger pK_a values (**Figure 1.6c**, HPTS, pK_a = 7.9). As the photoacid solutions are titrated to more alkaline conditions, k_{obs} decreases, which is consistent with **Equation 1.22**, until the pH of the solution approaches pK_a (**Figure 1.6c,d**). The minimum k_{obs} occurs near the pK_a of the photoacid, when both $[PA^-]$ and $[H^+]$ result in perfect equal-concentration second-order kinetics. Further titration to even more alkaline conditions result in pseudo-first-order kinetics dictated by $[PA^-]$ due to ground-state deprotonation of the photoacid described by **Equation 1.5**, reflected in the lower and upper x-axes corresponding to a_{H+} and $[PA^-]$ respectively in **Figure 1.6c**

for HPTS. The presence of more [PA^-] compared to [H^+] resulted in an increase for k_{obs}. The parabolic nature of k_{obs} as a function of pH is reflected in a comprehensive analytical model accounting for all transiently generated species in the following conservation of mass relation (**Equation 1.23**), following **Equation 1.13**, reproduced below. The following approach does not assume any negligible change to the equilibrium concentration of any species and thus is rigorous for both high $[H^+]_{eq}$ and $[PA^-]_{eq}$,

$$\frac{d([\mathbf{PA^-}]_{\mathbf{eq}}+\Delta[\mathbf{PA^-}]_t)}{dt} = -k_{+2}[PA^-]_t([H^+]_{eq} + \Delta[\mathbf{H^+}]_t) + k_{-2}([\mathbf{PAH}]_{\mathbf{eq}} + \Delta[\mathbf{PAH}]_t) \quad (1.13)$$

$$\Delta[\mathbf{PA^-}]_t = \Delta[H^+]_t = [PA^-]_t - [\mathbf{PA^-}]_{\mathbf{eq}} = -\Delta[\mathbf{PAH}]_t \quad (1.23$$

$$k_{-2}[\mathbf{PAH}]_{\mathbf{eq}} = k_{+2}[\mathbf{PA^-}]_{\mathbf{eq}}[\mathbf{H^+}]_{\mathbf{eq}} \quad (1.16)$$

where when conservation of mass (**Equation 1.23**) and equilibrium relationship (**Equation 1.16**) are substituted into **Equation 1.13**, the following quadratic equation (**Equation 1.25**) in terms of $[PA^-]_t$ and equilibrium concentrations is obtained, followed by its corresponding integrated rate equation (**Equation 1.27**).

$$\frac{d[PA^-]_t}{dt} = -k_{+2}[PA^-]_t([\mathbf{H^+}]_{\mathbf{eq}} + [PA^-]_t - [\mathbf{PA^-}]_{\mathbf{eq}}) + k_{+2}[\mathbf{PA^-}]_{\mathbf{eq}}[\mathbf{H^+}]_{\mathbf{eq}} + k_{-2}(-[PA^-]_t + [\mathbf{PA^-}]_{\mathbf{eq}}) \quad (1.24)$$

$$\frac{d[PA^-]_t}{dt} = -k_{+2}[PA^-]_t{}^2 + [PA^-]_t(-k_{+2}[\mathbf{H^+}]_{\mathbf{eq}} + k_{+2}[\mathbf{PA^-}]_{\mathbf{eq}} - k_{-2}) + k_{+2}[\mathbf{PA^-}]_{\mathbf{eq}}[\mathbf{H^+}]_{\mathbf{eq}} + k_{-2}[\mathbf{PA^-}]_{\mathbf{eq}} \quad (1.25)$$

$$\int_{[PA^-]_{eq} + \Delta[PA^-]_o}^{[PA^-]_{eq} + \Delta[PA^-]_t} \frac{1}{-k_{+2}[PA^-]_t{}^2+[PA^-]_t(-k_{+2}[\mathbf{H^+}]_{\mathbf{eq}}+k_{+2}[\mathbf{PA^-}]_{\mathbf{eq}}-k_{-2})+k_{+2}[\mathbf{PA^-}]_{\mathbf{eq}}[\mathbf{H^+}]_{\mathbf{eq}}+k_{-2}[\mathbf{PA^-}]_{\mathbf{eq}}} d[PA^-]_t = \int_0^t dt \quad (1.26)$$

$$\Delta[\mathrm{PA^-}]_t = \frac{\Delta[\mathrm{PA^-}]_0\left(1-\tanh\left(0.5t\left(k_{+2}[\mathbf{PA^-}]_{\mathbf{eq}}+k_{+2}[\mathbf{H^+}]_{\mathbf{eq}}+k_{-2}\right)\right)\right)}{1+\tanh\left(\left(0.5t\left(k_{+2}[\mathbf{PA^-}]_{\mathbf{eq}}+k_{+2}[\mathbf{H^+}]_{\mathbf{eq}}+k_{-2}\right)\right)*\left(1+\frac{2k_{+2}\Delta[\mathrm{PA^-}]_0}{k_{+2}[\mathbf{PA^-}]_{\mathbf{eq}}+k_{+2}[\mathbf{H^+}]_{\mathbf{eq}}+k_{-2}}\right)\right)} \quad (1.27)$$

To solve for an unknown pK_a value, the variables $[H^+]_{eq}$ and $[PA^-]_{eq}$ can be recast to pH and $[PAH]_{total}$, with the latter using the Henderson-Hasselbalch equation (**Equation 1.6**) and the definition of pK_a (**Equation 1.28**) to obtain the following equation.

$$pK_a = -\log\frac{k_{-2}}{k_{+2}} \quad (1.28)$$

$$\Delta[\mathrm{PA^-}]_t = \frac{\Delta[\mathrm{PA^-}]_0\left(1-\tanh\left(0.5t\left(k_{+2}\left(\frac{[PAH]_{total}}{1+10^{(-pH*n)}*\frac{n*k_{+2}}{k_{-2}}}\right)+k_{+2}(10^{-pH})+k_{-2}\right)\right)\right)}{1+\tanh\left(\left(0.5t\left(k_{+2}\left(\frac{[PAH]_{total}}{1+10^{(-pH*n)}*\frac{n*k_{+2}}{k_{-2}}}\right)+k_{+2}(10^{-pH})+k_{-2}\right)\right)*\left(1+\frac{2k_{+2}\Delta[\mathrm{PA^-}]_0}{k_{+2}\left(\frac{[PAH]_{total}}{1+10^{(-pH*n)}*\frac{n*k_{+2}}{k_{-2}}}\right)+k_{+2}(10^{-pH})+k_{-2}}\right)\right)} \quad (1.29)$$

The forward (k_{+2}) and reverse (k_{-2}) rate constants describe ground-state reprotonation kinetics (**Equation 1.2)**, while K_a is an equilibrium constant for acid dissociation, hence why k_{-2} is in the numerator of the logarithmic quotient of **Equation 1.28**.

Non-linear least-squares fitting of kinetic data as a function of pH to **Equation 1.29** produces values for the forward and reverse rate constants for photoacid reprotonation (k_{+2} and k_{-2}), and by extension pK_a, with prerequisite knowledge of $[PAH]_{total}$, pH, and $\Delta[PA^-]_o$ of each transient absorption spectroscopy trial. Experimental error in the fitted values were reduced by simultaneously fitting multiple kinetic data at different pH, while sharing the values of k_{+2} and k_{-2} across all fits, termed global fitting (**Figure 1.7**).

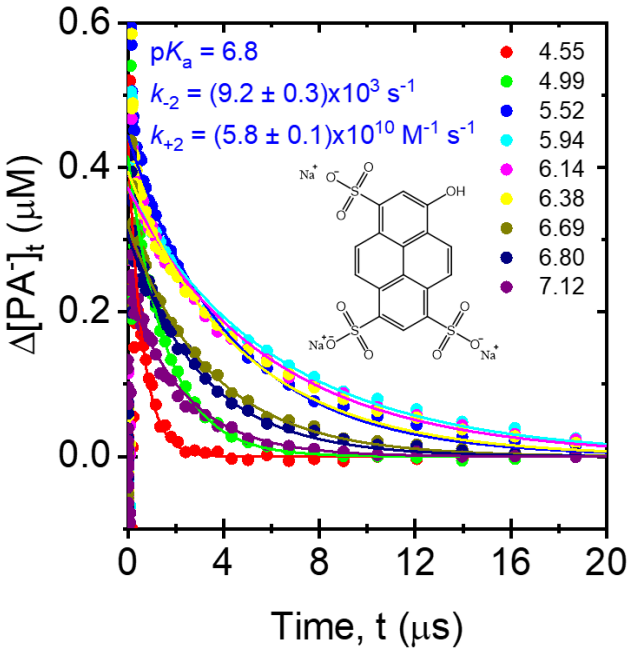

Figure 1.7. Transient kinetic data for 10 μM HPTS dissolved in aqueous electrolyte at various pH after 355 nm pulsed-laser excitation (0.5 mJ/pulse). Global fits were done with non-linear least squares fitting of **Equation 1.29**, producing the above forward and reverse rate constants for photoacid reprotonation.

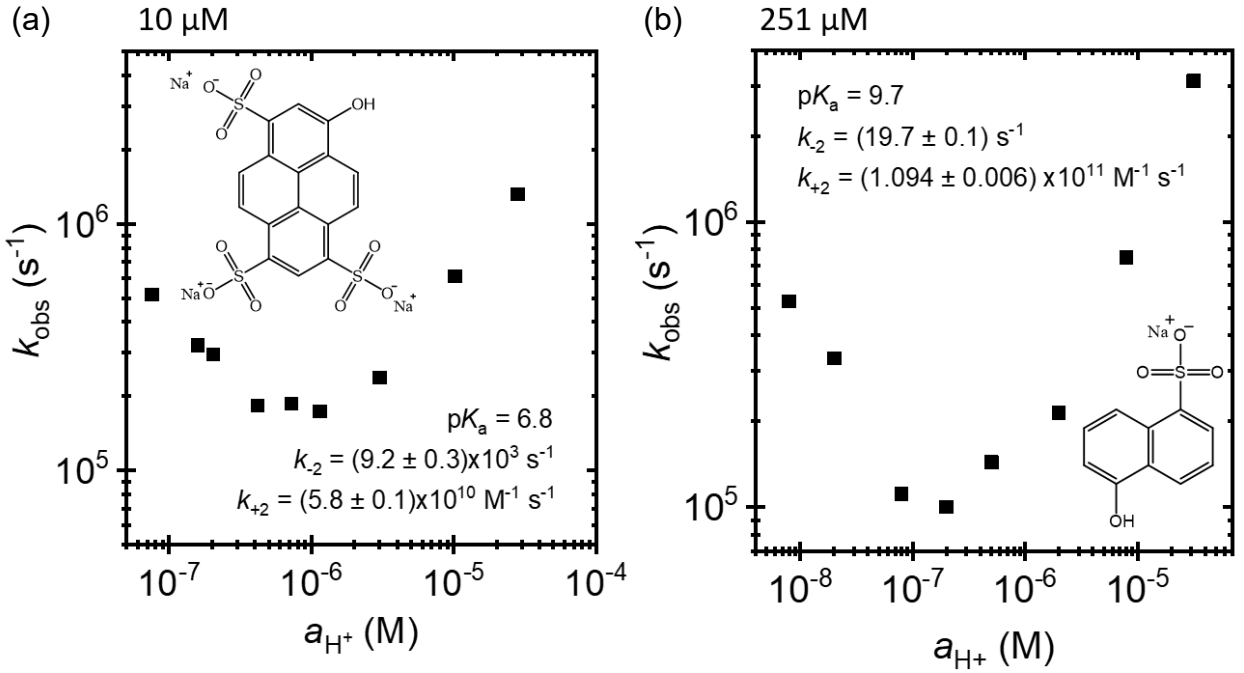

Figure 1.8. Kinetic data from transient absorption spectroscopy for **(a)** 10 μM HPTS (0.5 mJ/pulse) and **(b)** 251 μM $NaphSO_3$ with 10 mM ionic strength (0.2 mJ/pulse) dissolved in aqueous electrolytes after 355 nm pulsed-laser excitation. Individual data points are estimated observed rate constants obtained from non-linear least squares fitting of an exponential decay as a function of solution acidity while the listed values were derived from a global fit with **Equation 1.29**.

Application of the global fit described above for HPTS and $NaphSO_3$ results in pK_a values of 6.8 and 9.7, respectively (**Figure 1.8**). Although these values differ from those determined using steady-state spectroscopic acid–base titrations (HPTS pK_a = 7.9, $NaphSO_3$ pK_a = 9.3), the derived kinetic model **Equation 1.29** only accounts for the forward and backwards reaction of **Reaction 1.2**. Ground-state reprotonation with H_2O(l) as the proton donor would result in inaccurate modeling of the forward and reverse rate constants though the extent of this error has yet to be quantified. Furthermore, the model assumes no other reactions aside from ground-state reprotonation occurs. This is important to note, because spectroscopic data for the ground-state reprotonation of HPTS (**Figure 1.6a**) contains an additional growth at 510 nm that corresponds to the electronically reduced, deprotonated HPTS, which can occur if photoacids are excited with high peak fluences and/or if the equilibrium solution contains a large [PA^-]. It is hypothesized that absorption of a second photon by excited-state deprotonated HPTS results in excited-state electron transfer to ground-state deprotonated HPTS, resulting in the oxidation and reduction of two HPTS molecules.[40] Although the reduced form of HPTS quickly returns to its neutral form, oxidized HPTS is relatively stable on the order of minutes if reduced HPTS does not recombine with oxidized HPTS, instead reducing H^+(aq). For quantitative studies of photoacids where electron-transfer reactions are not accounted for, it is imperative to avoid high peak fluences as oxidation of the photoacid results in modeling inaccuracies which may manifest itself as a loss of protonated photoacids able to undergo the Förster cycle, basification of the solution due to reduction of H^+(aq), or an underestimation of $\Delta[PA^-]_o$, especially if the kinetic data is collected after numerous excitation pulses/averages. Lastly, ionic strength influences the pK_a of photoacids and buffers,[34] therefore comparisons between techniques quantifying pK_a are only valid when performed under similar ionic strengths due to changes in activity coefficients which shift observed pK_a values. The

differences in pK_a for HPTS between steady-state and time-resolved acid–base titrations can be associated with a loss of PA^-(aq) due to oxidation (**Figure 1.6a**). Subsequent experiments utilized lower irradiation densities but a 10-fold increase in ionic strength (1 mM for steady-state titration and 10 mM for transient absorption spectroscopy) may account for the difference in pK_a values for $NaphSO_3$.

The observation that pseudo-first-order kinetics are operative in the presence of either excess $[H^+]$ or $[PA^-]$ implies that the valley of the parabola in each dataset describes the estimated acidity needed to obtain the smallest product of $[PA^-]$ and $[H^+]$, resulting in the minimum k_{obs} (**Figure 1.8**). The Henderson-Hasselbalch equation (**Equation 1.6**) shows that $[PA^-]$ is dependent on pK_a, $[H^+]$, and $[PAH]_{total}$, which ultimately sets the smallest product of $[PA^-]$ and $[H^+]$. When comparing the pK_a difference between HPTS and $NaphSO_3$, it is unintuitive that a 1.4 unit increase in pK_a from HPTS to $NaphSO_3$ only results in a minor decrease in k_{obs} (~$2x10^5$ s^{-1} for HPTS, $1x10^5$ s^{-1} for $NaphSO_3$, **Figure 1.8**). It was serendipitous that the combinations of pK_a and $[PAH]_{total}$ explored for these two photoacids resulted in roughly the same $[H^+]$ ($1x10^{-6}$ to $2x10^{-7}$ M) corresponding to their minimum k_{obs}. Since the minimum k_{obs} is observed when $[PA^-] \approx [H^+]$, an order-of-magnitude difference in the acidity required to observe the minimum k_{obs} between two photoacids should result in a two-fold decrease in minimum k_{obs}, assuming all photoacids studied have similar second-order ground-state reprotonation rate constants, k_{+2}. For HPTS and $NaphSO_3$, k_{+2} is within an order-of-magnitude, suggesting the minor decrease in k_{obs} is due to a smaller-than-expected difference in acidities where the lowest k_{obs} was observed, or due to alternative proton donors becoming more kinetically viable, namely H_2O(l). The latter can be further explored in future studies since the acidities needed to generate the lowest reprotonation rates between PA^-(aq) and H^+(aq) is a second-order kinetic process while reprotonation rates between PA^-(aq) and

$H_2O(l)$ is expected to be first order given the assumption of a fixed $a_{H2O(l)} = 1$, which is a reasonable assumption under our experimental conditions.

Ground-State reprotonation kinetics of HPTS and $NaphSO_3$ as a function of buffer concentration. Traditional electronic dye-sensitized solar cells are majority carrier devices. Light absorption results in photogeneration of majority carrier electrons typically in a wide bandgap electronic semiconductor, like TiO_2, SnO_2, ZnO, etc., and concomitant generation of an oxidized dye that is then regenerated via reduction by a soluble redox mediator to complete the dye sensitization cycle. Analogous to this, the addition of a Brønsted–Lowry acid proton donor (buffers, BH/B^-), aside from water, can enable ground-state regeneration of a photoacid by the reaction below, transiently photogenerating $H^+(aq)$ and $B^-(aq)$.

$$PA^-(aq) + BH(aq) \underset{k_{-3}}{\overset{k_{+3}}{\rightleftarrows}} BH(aq) \tag{1.30}$$

To most clearly demonstrate transient storage and photogeneration of protonic species other than those from water, the ground-state reprotonation of HPTS and $NaphSO_3$ was examined in the presence of soluble buffers 2-(*N*-morpholino)ethanesulfonic acid (MES) and tris(hydroxymethyl)aminomethane (Tris) respectively. Using this we demonstrate that $H^+(aq)$ and $B^-(aq)$ can be transiently photogenerated, providing preliminary evidence that photoacids can be used as dye sensitizers in water-based solar cells.

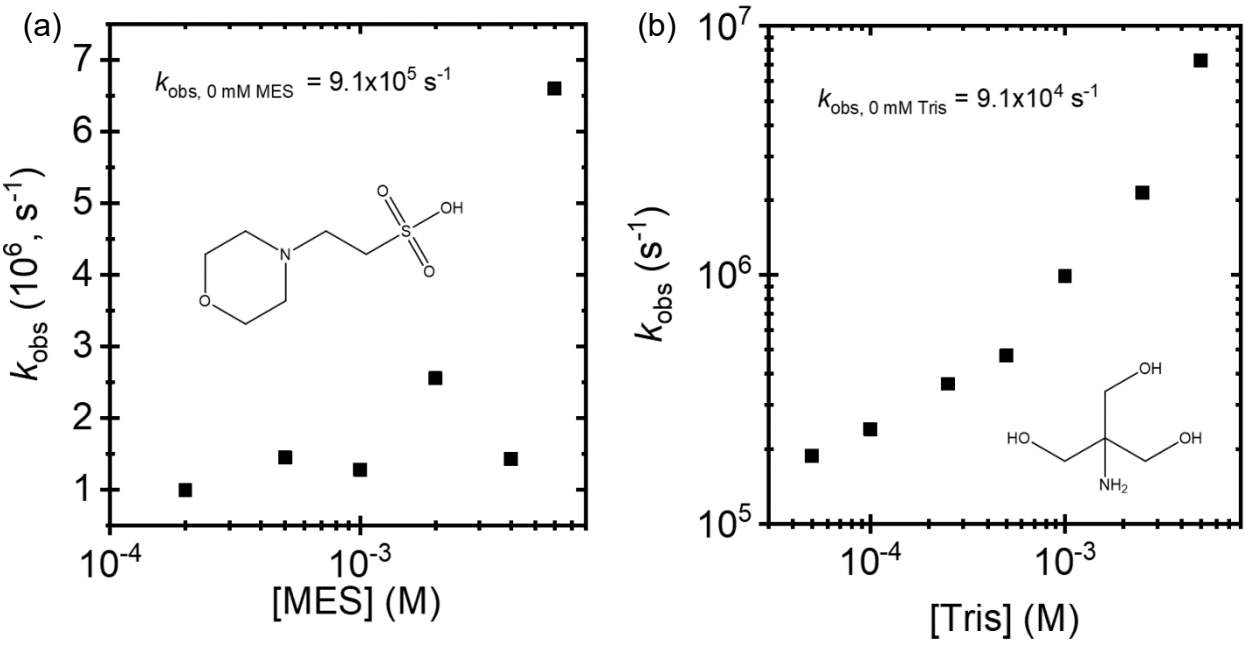

Figure 1.9: Kinetic data from transient absorption spectroscopy as a function of [BH] with **(a)** 1 μM of HPTS, pH 5.0, titrated with MES, and **(b)** 251 μM of NaphSO3, pH 6.7, titrated with Tris. Measurements were performed at 355 nm pulsed-laser excitation at 0.5 mJ/pulse and 1.2 mJ/pulse for HPTS and NaphSO3 respectively.

To demonstrate majority carrier photochemical generation of protonic species analogous to ground-state redox regeneration of photoreduced dyes in p-type dye-sensitized solar cells, buffers were titrated in solutions of photoacids to observe a mechanistic shift from H^+(aq) to BH(aq) as the proton donor species. The buffers MES (pK_a = 6.2) and Tris (pK_a = 8.1) were selected for HPTS and $NaphSO_3$ respectively due to an approximate one unit pK_a difference between BH(aq) and PAH(aq). This condition allows the ground-state reprotonation with BH(aq) to be thermodynamically favorable (**Equation 1.11**) without unnecessarily increasing solution acidity, since [H^+] influences [BH] via the Henderson-Hasselbalch equation (**Equation 1.5**) but H^+(aq) is also the competing reactant (**Reaction 1.2**) to **Reaction 1.30**. With acidity fixed, the total concentration of buffer species, $[BH]_{total}$, can be increased to increase the ground-state reprotonation rate constant (k_{obs}) between PA^-(aq) and BH(aq). **Figure 1.9** contains the k_{obs} for deprotonated photoacid reprotonation obtained from non-linear least squares fitting of an

exponential decay to transient absorption spectroscopy data at various [BH] with k_{obs} in the absence of BH(aq) listed for comparison. For both HPTS and $NaphSO_3$, increasing $[BH]_{total}$ resulted in higher ground-state reprotonation rate constants. When the photoacid pK_a is larger, lower $[H^+]$ is accessible while maintaining high [PAH], allowing the proton donor transition from H^+(aq) to BH(aq) to be observed at lower [BH]. Although the correlation between k_{obs} and [BH] implies that the favored proton donor is shifting from H^+(aq) to BH(aq), the time constant for the regeneration of B^-(aq) is unknown, where B^-(aq) is analogous to photogenerated, non-equilibrium redox species in dye-sensitized solar cells. It is of interest to lengthen the recombination time constant between the photogenerated majority carrier and the transient redox/buffer species as instantaneous recombination results in lower quantum yields and photoresponses, with a sub-field of dye-sensitized solar cell study focused on redox species optimization.[41,42] Prior studies utilized time-resolved infrared spectroscopy to directly observe proton-transfer intermediates following excitation of an *irreversible* photoacid. Despite the presence of OH^-(aq), acetate ion was observed to be transiently protonated from the photogenerated H^+(aq).[43] Adaption of this technique allows direct observation of the protic functional group of B^-(aq), offering insight into the reprotonation time constant for B^-(aq) reprotonation and charge collection requirements of a water based solar cell.

Chapter 1.3: Conclusion

Transient absorption spectroscopy was utilized to identify the proton donor species for ground-state reprotonation of aqueous photoacids for analogous comparisons to photogenerated mobile charge carriers in crystalline electronic semiconductors. Reprotonation rate constants were measured as a function of proton concentration, leading to the development of an analytical model for identifying the forward and reverse rate constants for ground-state reprotonation with H^+(aq).

The proton donor in most scenarios was H^+(aq) but preliminary data from photoacids with neutral to basic pK_a at low total photoacid concentration suggests ground-state reprotonation from H_2O(l), potentially being the first evidence for transient generation of H^+(aq) and OH^-(aq) via the Förster cycle. Similar studies for analogous comparisons to ground-state redox regeneration of photoreduced dyes in p-type dye-sensitized solar cells showed that ground-state reprotonation of conjugate bases of photoacids with Brønsted–Lowry acid proton donors could outcompete similar reprotonation with H^+(aq).

Chapter 1.4: Experimental

Absorption and Photoluminescence Spectroscopy. Absorption and photoluminescence spectra were obtained using a spectrophotometer (Duetta, HORIBA). Photoluminescence spectra were collected with 5 nm excitation and emission slit widths and with resulting data autocorrected for the wavelength-dependent sensitivity of the detection system. All titrated solutions were prepared by mixing stocks of 1 mM acid and base solution (e.g. HCl and NaOH), both containing the same concentration of photoacid to achieve a desired pH. Photoluminescence spectra were corrected for their refractive indexes and HCl concentration was corrected for its effective acidity, H_0, as defined in **Chapter 1.1**.

Transient Absorption Spectroscopy. Kinetic data for the reprotonation of ground-state deprotonated photoacids were collected with a custom transient absorption spectroscopy system. Optically dilute aqueous solutions of photoacids (Abs_{355nm} < 0.05 at the excitation wavelength (λ_{ex})) were titrated to pH values of ~3 – 6 for HPTSA and ~4-9 for HPTS/NaphSO_3 using concentrated $HClO_4$(aq) and NaOH(aq). $HClO_4$(aq) was chosen for its high acidity ($pK_a = -10$) and redox stability of the conjugate base, ClO_4^-(aq). Other strong acids, specifically H_2SO_4(aq) ($pK_{a,1} = -3.0$, $pK_{a,2} = +2.0$) and HNO_3(aq) ($pK_a = -1.3$), were avoided to prevent excited-

state proton transfer between PAH* and the conjugate base of the strong acid. Titrated solutions of $NaphSO_3$ were prepared by mixing stocks of 10 mM acid and base ($HClO_4$ and NaOH), both containing the same concentration of photoacid to achieve a desired pH. HPTS and HPTSA solutions were prepared by injecting identical volumes of stock photoacid solution into a volumetric flask and arbitrary amounts of acid and base were added to achieve the desired pH, before the flask was filled to the final volume.

Titrated solutions were sparged with argon and excited using the third harmonic of an Nd:YAG laser (Continuum Minilite II, ~5 ns pulse width, 3 mm diameter) and probed with an optically chopped 150 W xenon arc lamp (~20 ms pulse width) with averaged signals obtained from 100-4000 pump–probe pulses. A 360 nm long-pass filter was used for both full spectra and single-wavelength measurements to minimize laser scatter into the monochromator, while a 450-nm short-pass filter was introduced for single-wavelength pH-dependent measurements to attenuate photoluminescence. To minimize effects due to excited-state species, including competing transient absorption spectroscopy signals and PMT ringing due to strong photoluminescence, kinetic analysis of transient absorption spectroscopy data was performed starting 100 ns after photo-excitation. In order to preserve time resolution at early times, at the expense of signal-to-noise, data was adjacent-average smoothed in a logarithmic time domain resulting in <100 points for each decade of time. Changes in absorbance was converted to changes in concentration of deprotonated photoacid by dividing absorbance by the difference of the molar decadic absorption coefficient between the protonated and deprotonated photoacid species at the wavelength studied.

Chapter 2: Development of Photoelectrochemical Detection of Photogenerated Protons and Hydroxides

The consequences of exciting aqueous solutions of photoacids or photobases is the transient generation of H^+(aq) and/or OH^-(aq) as described by the Förster cycle. Under continuous illumination, photogeneration of these protonic species compete with their recombination via the following reaction,

$$H^+ (aq) + OH^- (aq) \rightleftharpoons H_2O (l) \qquad (2.1)$$

where the diffusion-limited forward rate constant is 1.3 x 10^{11} M^{-1} s^{-1} at room temperature.[44] Although the forward rate constant implies a fast reaction, at equilibrium, the rate of this reaction is actually quite slow due to the autoionization rate constant of 1.3 x 10^{-3} M^{-1} s^{-1}. Work by Natzle and Moore in the 1980s demonstrated a 50 μs time constant for recombination of photoionized H_2O(l) from pulsed-laser experiments at room temperature.[45] When the rate of photogenerating H^+(aq) and OH^- (aq) from excited photoacids are higher than the rate of recombination of those ions, a steady-state increase of protonic mobile charged species (H^+(aq) and OH^-(aq)) is observed.

Quantification of [H^+] and [OH^-] is possible assuming a sensor is selective for only one ion. A commercially available option is a typical pH probe, which consists of a proton selective glass membrane measuring the difference in a_{H+} between its internal electrolyte and

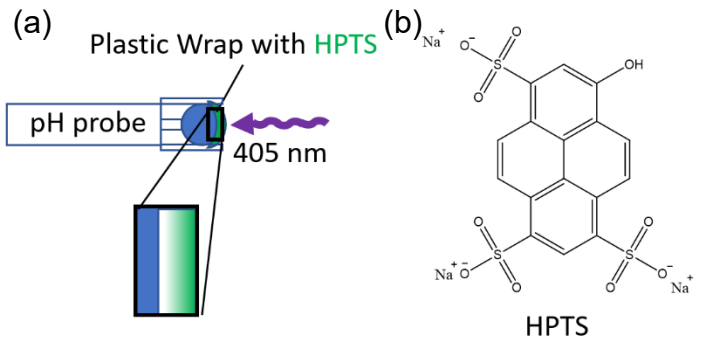

Figure 2.1. (a) Cartoon demonstrating initial attempts to measure pH changes due to excitation of photoacids. Concentrated solutions of photoacid (HPTS) results in Beer-Lambert absorption of light, confining most photoexcitation (green) to occur away from the active area (glass membrane) of the pH probe. **(b)** Chemical structure of 8-hydroxypyrene-1,3,6-trisulfonic acid (HPTS).

the sample solution.[46] Similarly, a commercial fluoride selective electrode, which is sensitive to OH^-(aq) as an "interfering ion" can be used to measure a_{OH-}. A simple, attempted experiment is to encase the bulb of a pH probe with plastic wrap containing a small volume of concentrated photoacid solution. Illuminating the bulb of the pH probe at a wavelength the photoacid absorbs at should induce a change in the pH measured by the probe, assuming the photoacid solution is in ionic communication with the pH probe electrolyte through a frit. Unfortunately, no noticeable change in pH was directly correlated with illumination of the bulb with 405 nm light. Although the thickness of the solution was defined by the capillary action between the plastic wrap and the pH probe bulb, a high concentration of photoacid solution was used to localize the density of photogenerated protonic species at the material||solution interface, resulting in a Beer-Lambert absorption profile across the solution with most absorption happening at the plastic wrap||solution interface (**Figure 2.1a**). Excitation of the solution at the glass||solution interface is predicted to produce the largest measurable change in a_{H+} or $[H^+]$.

Chapter 2.1 Results and Discussion

The observations made from the above experiment lead to the following design criteria for a transparent H^+(aq) sensor: 1) Must be optically transmissive, to allow for backside illumination through the sensor and 2) must be selective for either H^+(aq) or OH^-(aq). The signal contribution from H^+(aq) or OH^-(aq) from a sensor sensitive to both can be deconvoluted only if recombination (**Reaction 2.1**) was the only sink for those species. The presence of other protonic species, namely the photoacid and its conjugate base, have a non-zero contribution to the concentration of H^+(aq) and OH^-(aq). The first revision of this sensor was a circular Pt electrode, slightly smaller than the diameter of the light source (3 mm), electroplated in the center of fluorine-doped tin oxide (FTO) glass. FTO was chosen due to its ubiquitous application in dye-sensitized solar cells as a visibly

transmissive, conductive electrode while Pt was chosen for its half-cell reaction, the reversible hydrogen electrode (RHE), involving H^+ (aq) and H_2 (g). The half-cell potential measured at a RHE is defined by the Nernst equation, which has the following general form,

$$E_{\mathrm{N}} = E_{\mathrm{N}}^{\mathrm{o}} - \frac{RT}{nF}\ln\left(\frac{\left(a_{\mathrm{red}}^{\mathrm{sol}}\right)^{\nu_{\mathrm{red}}}}{\left(a_{\mathrm{ox}}^{\mathrm{sol}}\right)^{\nu_{\mathrm{ox}}}}\right) = E_{\mathrm{N}}^{\mathrm{o}\prime} - \frac{RT}{nF}\ln\left(\frac{\left(c_{\mathrm{red}}^{\mathrm{sol}}\right)^{\nu_{\mathrm{red}}}}{\left(c_{\mathrm{ox}}^{\mathrm{sol}}\right)^{\nu_{\mathrm{ox}}}}\right) \quad (2.2)$$

where $E_{\mathrm{N}}^{\mathrm{o}}$ and $E_{\mathrm{N}}^{\mathrm{o}\prime}$ are the standard reduction potential and formal reduction potential, respectively, including contributions from activity coefficients and standard-state concentrations, *R* is the gas constant (J mol^{-1} K^{-1}), *T* is temperature (K), *F* is the Faraday constant (C mol^{-1}), *n* is the number of electrons transferred in the redox reaction, and *v* and *c* are the relative stoichiometric number and concentration of the reduced (red) or oxidized (ox) species, respectively. The form of **Equation 2.2** specific for a RHE is defined as

$$E_{\mathrm{RHE}} = E_{\mathrm{RHE}}^{\mathrm{o}\prime} - \frac{RT}{2F}\ln\left(\frac{P_{H_2}}{[H^+]^2}\right) = -\frac{\ln(10)RT}{2F}\log\left(\frac{P_{H_2}}{[H^+]^2}\right) \quad (2.3)$$

$$E_{\mathrm{RHE|1\ bar}\ H_2, 25\ ^\circ C} = -0.0296 * \log\left(\frac{1}{[H^+]^2}\right) = -0.0592 * pH \quad (2.4)$$

When the solution is sparged with hydrogen gas to open atmosphere at room temperature, **Equation 2.3** approximates to the relationship defined by **Equation 2.4**. A scintillation vial, with its bottom removed, affixed to the platinized FTO slide with silicone caulk results in a custom electrochemical cell with an optically transparent RHE. A septum with ports for a counter and reference electrode forms a complete, gas tight electrochemical cell (**Figure 2.3b**, with sputtered Pt). A 405 nm light source incident from the bottom of the cell transmits through the RHE and excites the photoacid at the RHE||solution interface. We first confirmed the background response of platinized FTO by illumination of the circular Pt electrode with various laser diodes. A response from platinized FTO upon illumination with 405 nm light resulted in a photovoltage in inert supporting electrolyte (**Figure 2.2**), while illumination of platinum sputtered on glass microscope slides in the same setup (**Figure 2.3b**, measurement not included) resulted in no noticeable photovoltage, suggesting FTO was photoactive from our 405 nm laser diode.

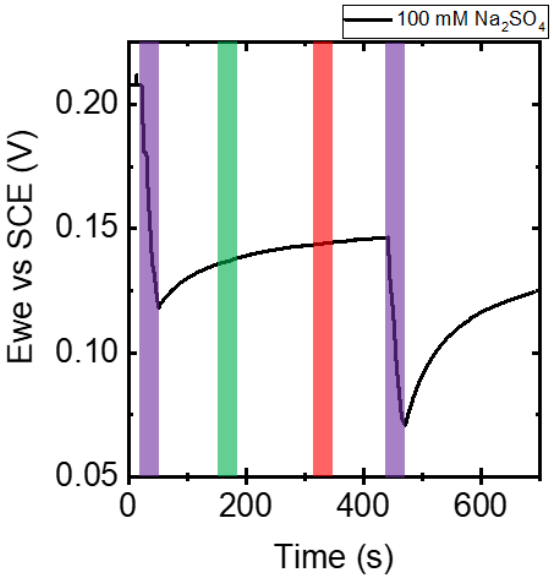

Figure 2.2. Open-circuit potential measurement of a platinized FTO electrode integrated into an electrochemical cell with a Pt counter electrode and a saturated calomel electrode (SCE) immersed in 100 mM Na_2SO_4 supporting electrolyte. Colored bars represent periods of illumination through the FTO-Pt electrode with 405 nm (purple), 532 nm (green), and 650 nm (red) laser diodes (10-25 mW).

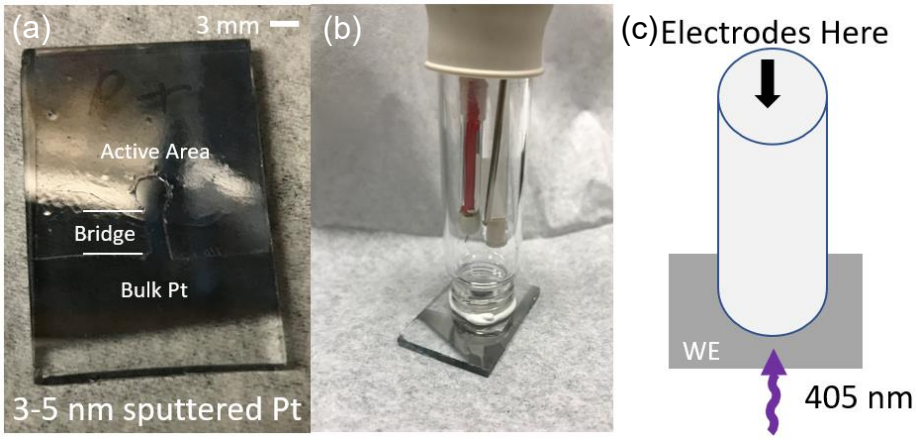

Figure 2.3. (a) Masked glass microscope slide with sputtered Pt. A narrow bridge connects the bulk Pt outside of the electrochemical cell with a circular active area. **(b)** Assembled electrochemical cell consisting of a scintillation vial affixed to the sputtered Pt electrode with silicone caulk. A septum is inserted in an opening at the top of the scintillation vial to replace electrodes and form a gastight seal. **(c)** Cartoon depicting the electrochemical cell in use.

The second revision of this sensor kept the same electrochemical cell construction albeit replacing the electroplated platinized FTO electrode with sputtered Pt on glass microscope slides. Substitution of the conductive FTO substrate with an insulating glass slide guaranteed contributions to photoresponses are solely due to the thin film of Pt. Electroplating was replaced with sputtering due to the ease of patterning the Pt electrode as well as better reproducibility in Pt thickness, affecting properties like electrode resistance and optical transmission. Prior to sputtering, a mask patterned with Scotch transparent tape was applied to the glass slide to define a ~3 mm active area with a ~2 mm bridge connecting the active area (**Figure 2.3a**) with bulk Pt outside of the electrochemical cell (**Figure 2.3b**). The addition of bulk Pt and a Pt bridge was necessary to electrically connect the active area of the sensor to the potentiostat, features not necessary for electroplated platinized FTO electrodes. Dye solutions were continuously sparged with H_2 gas during the experiment and photoexcitation was performed by back-side illumination of the RHE with a various laser diodes.

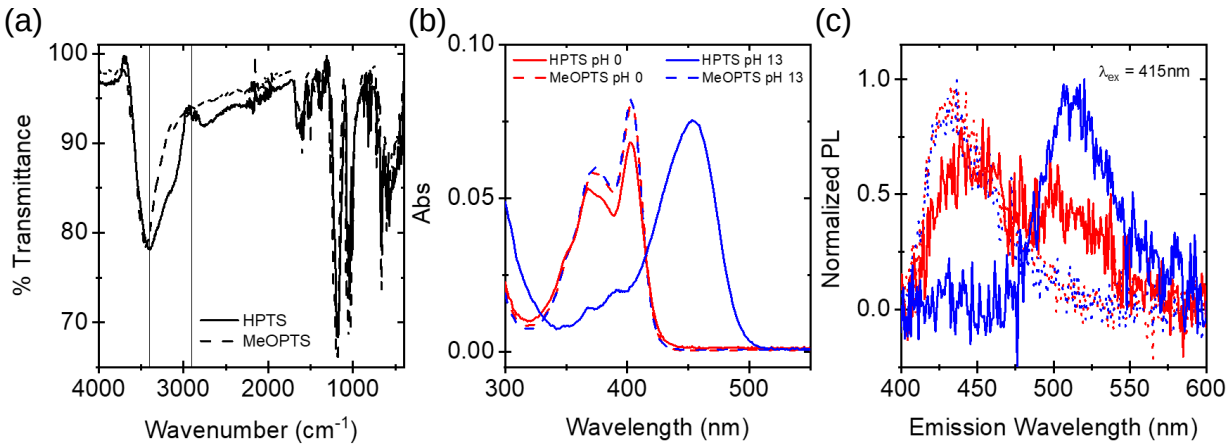

Figure 2.4. Spectroscopic characterization of HPTS (solid lines) and MeOPTS (dashed lines): **(a)** Fourier-transform infrared spectra using attenuated total internal reflection of vacuum-dried solid powder, and **(b)** electronic absorption spectra and **(c)** photoluminescence spectra of aqueous electrolytes consisting of 1 M HCl (red) and 100 mM NaOH (blue).

Two different dyes were used in the electrochemical cell: photoacid 8-hydroxypyrene-1,3,6-trisulfonic acid (HPTS; pK_a = 7.8; pK_a* = -0.3) and its analogous control dye 8-methoxypyrene-1,3,6-trisulfonic acid (MeOPTS). The difference between these two dyes is the photoacidic alcohol group in HPTS is replaced with a methoxy group, a change that has little impact on the conjugated pyrene ring and results in similar absorption spectra between HPTS and MeOPTS (**Figure 2.4b**). Success of this reaction was supported by data obtained using FTIR–ATR spectroscopy (**Figure 2.4a**) and NMR spectroscopy (**Figure 2.5)**, which indicated a lack of a broad shoulder associated with the photoacidic hydroxyl group in the range of 2900 – 3400 cm^{-1} and the prescence of a singlet at a chemical shift of ~4.4 ppm that integrates to ~3 times larger than signals arising from single protons and is consistent with the methyl group on MeOPTS, respectively. Acid–base titrations with spectroscopic detection also supported that MeOPTS is not photoacidic, given similarities between the absorption and photoluminesce spectra when dissolved in aqueous acidic solutions *versus* alkaline solutions, and compared to protic HPTS under the same conditions (**Figure 2.4b,c**).

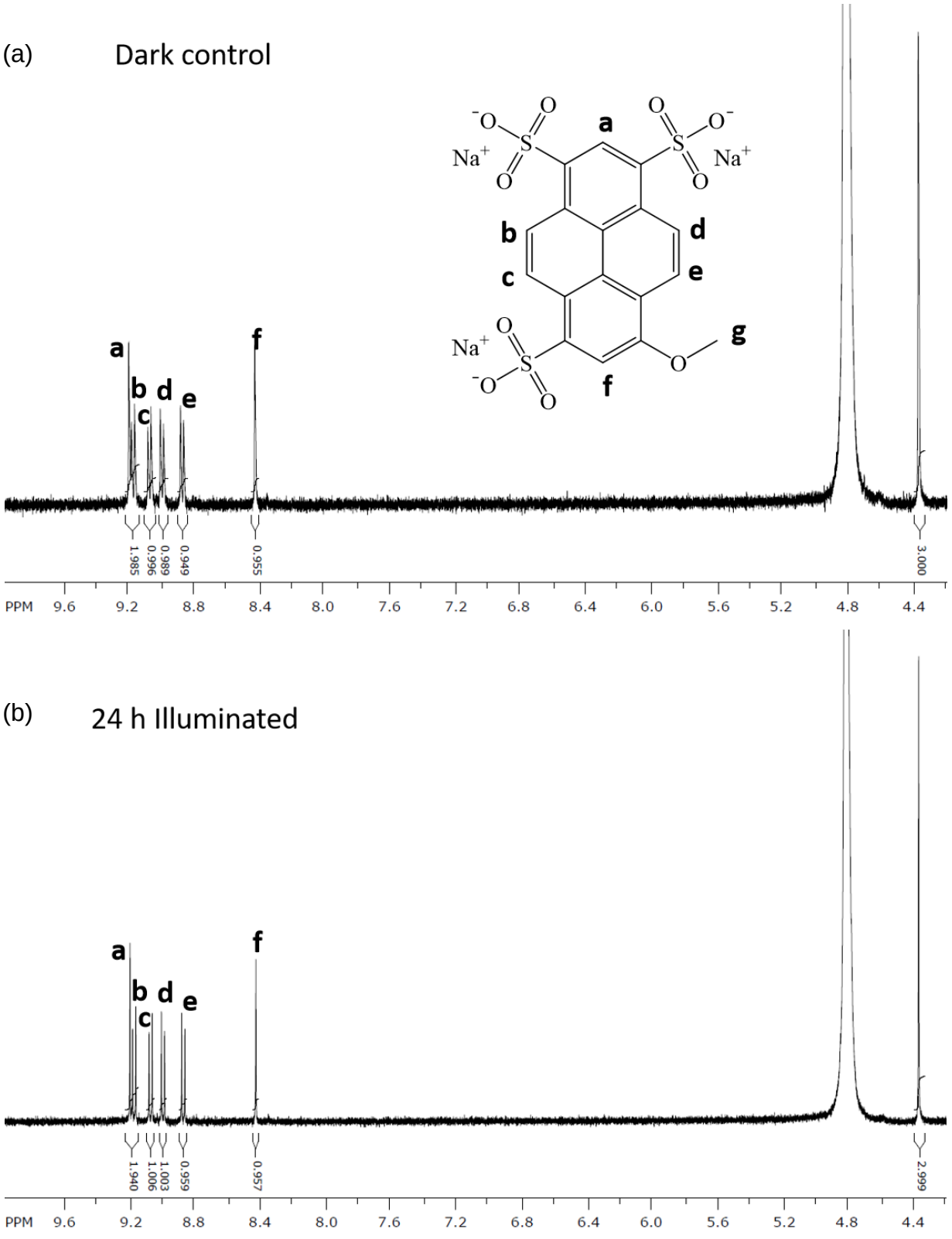

Figure 2.5. ^{1}H-NMR spectra of MeOPTS (inset: structure with labeled peaks) dissolved in D_2O(l) after being subjected to the following conditions for 24 h: **(a)** in the dark under ambient conditions and **(b)** illuminated from the bottom of the NMR tube with ~20 mW of 405 nm diode light from a generic presentation pointer. The peak at 4.8 ppm is due to H_2O impurity.

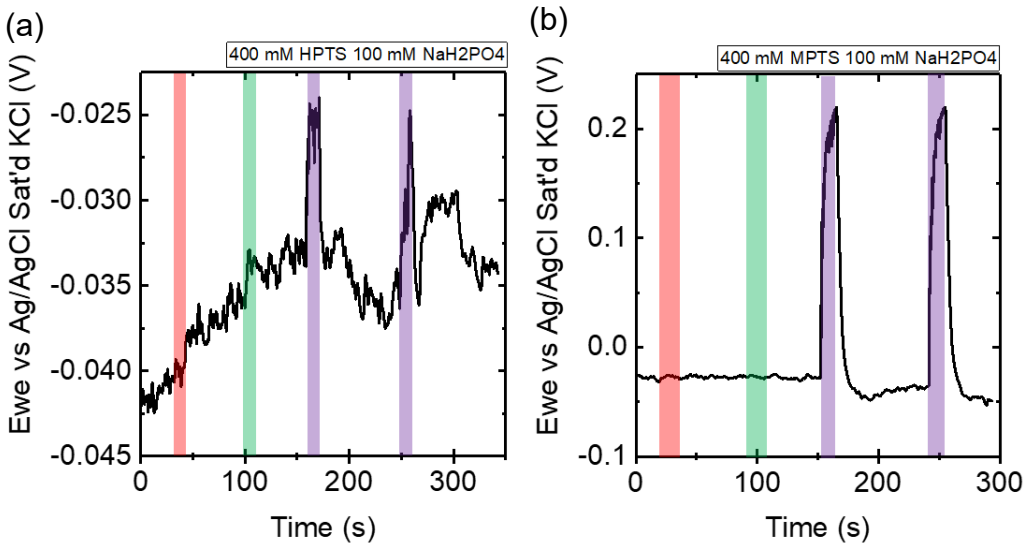

Figure 2.6. Open-circuit potential measurement of **(a)** 400 mM HPTS and **(b)** 400mM MPTS buffered to pH 7 with 100 mM NaH_2PO_4 under various wavelength illuminations with potentials referenced to a Ag/AgCl saturated KCl reference electrode.

Photoexcitation of 400 mM HPTS buffered to pH 7 with 405 nm light resulted in a positive photovoltage of ~10 mV, suggestive of an increase in a_{H+} (**Figure 2.6a**). This would agree well with the steady-state net photogeneration of protonic mobile charged species, however, the same experiment performed on 400 mM MeOPTS also showed a positive photovoltage despite MeOPTS's inability to photogenerate H^+ (aq) (**Figure 2.6b**). More surprisingly was that the photovoltage from MeOPTS was at least 20 times higher than that measured for HPTS, suggesting the photovoltage is not primarily dependent on perturbations of the RHE half-cell. Instead, the Pt sputtered electrode may be coupled to a different redox half-reaction, possibly the redox of the dyes, or is directly being perturbed by excited-state electron transfer from the dyes.

The third revision of the cell focused on decoupling electronic communication between the dye and the electrode while maintaining protonic transport. The solution was to spatially separate the dye from the electrode while enabling diffusion of H^+(aq) to the Pt electrode surface. Borrowing techniques from dye-sensitized solar cell construction, a thin layer of mesoporous

alumina was deposited on top of sputtered Pt by doctor-blading and sintering a suspension of alumina nanoparticles to serve as an electronically insulating barrier. Furthermore, molecules with carboxylic acid functional groups are able to anchor to the surface of alumina,[47] allowing photoacids to be deposited onto alumina while minimizing the amount of custom photoacids used when testing various electrolyte conditions (**Figure 2.7a**).

The photoacid chosen to anchor to alumina was 4,4'-((1E,1'E)-(5-carboxy-2-hydroxy-1,3-phenylene)bis(ethene-2,1-diyl))bis(1-methylpyridin-1-ium) (CHyPEMP; pK_a = 5.2; **Figure 2.7b**), synthesized by Dr. Christopher D. Sanborn.[32] The pK_a of CHyPEMP was experimentally determined from acid–base spectroscopic titrations by Dr. Sanborn but the pK_a* was predicted to be -8.5 from Förster cycle analysis from prior literature of a similar molecule (carboxylic acid substituted with a carboxylic ester).[48] However, the accuracy of this predicted pK_a* is questionable due to observations, from the same report, of protonated photoacid photoluminescence or incomplete excited-state proton transfer at mildly acidic conditions (pH 3), suggesting the pK_a* might be higher than reported. Förster cycle analysis assumes the energy difference between the $E_{0\text{-}0}$ for the protonated photoacid and the $E_{0\text{-}0}$ for the deprotonated

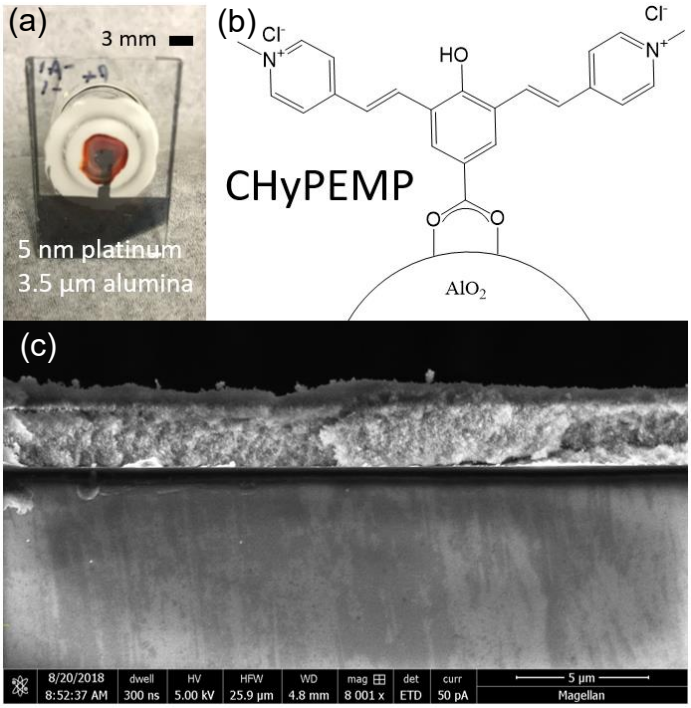

Figure 2.7. (a) Photographic image of the dyed alumina sintered on sputtered Pt electrode. **(b)** Molecular structure of CHyPEMP bound to alumina nanoparticles. **(c)** Scanning electron microscope image of the alumina-Pt electrode cross section showing a ~3.5 µm thick alumina layer.

photoacid, where $E_{0\text{-}0}$ is the energy difference between the lowest vibrational state of the ground and excited state, is the difference in the change in standard Gibbs free energies for excited-state proton transfer (ESPT) and ground-state proton transfer (GSPT).

$$E_{0-0,PAH} - E_{0-0,PA^-} = \Delta G^o_{GSPT} - \Delta G^o_{ESPT} \quad (2.5)$$

This assumption may not apply to CHyPEMP and its reported analog due to conformational relaxation (changes in entropy) of the excited-state photoacid before and/or after excited-state proton transfer.

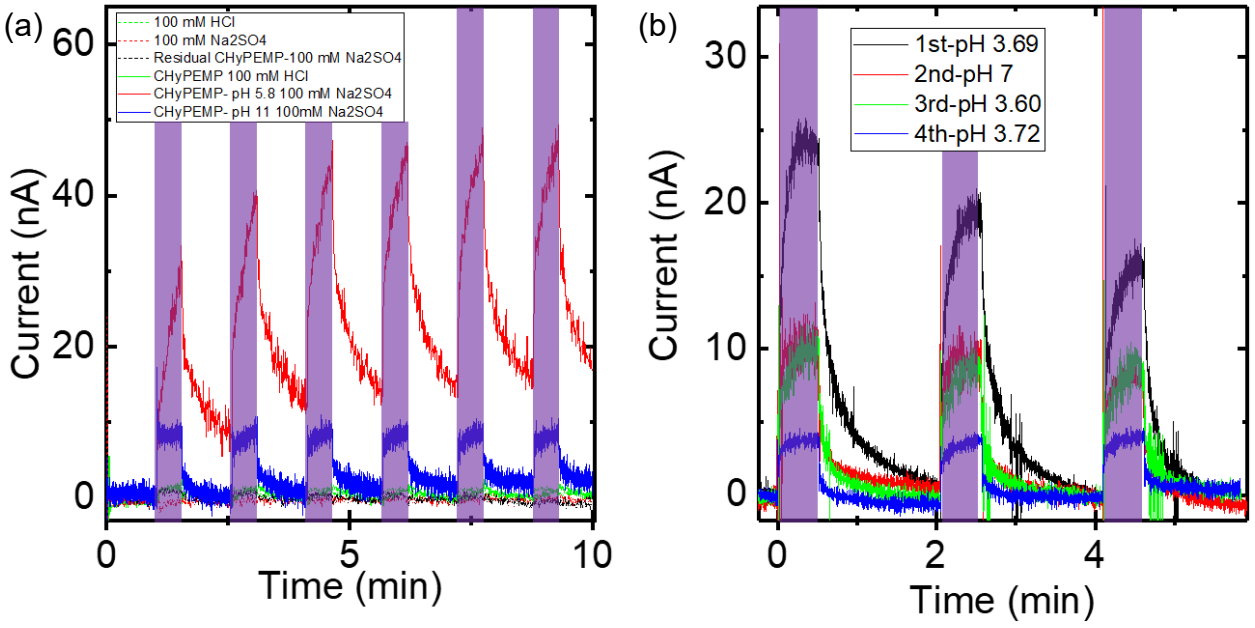

Figure 2.8. Short-circuit current measurement of **(a)** either undyed (dashed) and CHyPEMP dyed (solid) alumina-Pt reference electrodes in various pH electrolytes and **(b)** CHyPEMP dyed alumina-Pt reference electrode after several exchanges with fresh electrolyte in the electrochemical cell. All photoresponse events were due to illumination with 405 nm light.

Although CHyPEMP dyed alumina-Pt electrodes featured noticeable photocurrents (**Figure 2.8a**, solid lines), the pH under which these signals were measured did not agree with our knowledge of the Förster cycle. When 100 mM HCl was placed into the dyed electrochemical cell (green solid), a negligible signal similar to those observed in undyed electrochemical cells (dashed lines) was observed. Considering the pK_a of CHyPEMP is 5.2, it was unexpected to observe a small photoresponse at pH 1 unless the previously reported pK_a* determined via Förster cycle

analysis was predicted more negative then experimentally observed. However, experiments at pH > pK_a appear to produce larger photocurrents, suggesting the mechanism for photocurrent generation is again not related to H^+(aq) sensing.

Various electrolyte solutions affecting photoacid protonation state and the presence of redox active species were placed into electrochemical cells with and without CHyPEMP to identify the source of the photocurrent. When all solutions were sparged with hydrogen gas, electrolytes placed in the electrochemical cell without a dyed electrode resulted in negligible photocurrents when illuminated with 405 nm light (**Figure 2.8a**, dashed lines). This meant that light did not initiate photoredox reactions with electrolytes in the electrochemical cell, including one electrolyte solution containing leached CHyPEMP (black dash). Lower photocurrents were observed with subsequent electrolyte exchanges with fresh electrolyte, suggesting CHyPEMP was leaching into the electrolyte over time (**Figure 2.8b**). The lack of response from aqueous CHyPEMP alleviated concerns of CHyPEMP desorption from the electrode mid-experiment, altering measured

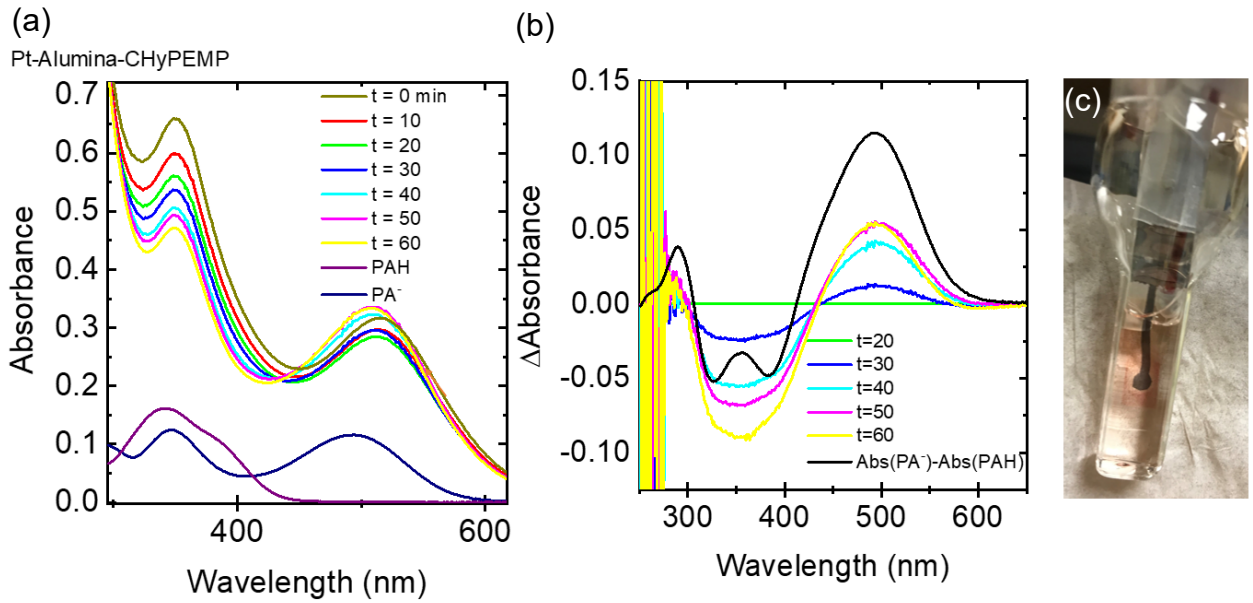

Figure 2.9. (a) Absorption spectra of a CHyPEMP dyed alumina-Pt electrode at different durations of negative bias. Protonated and deprotonated spectra correspond to measurements aqueous CHyPEMP. **(b)** Changes in absorbance baselined to the spectrum obtained at 20 minutes with earlier times omitted. **(c)** Photograph of CHyPEMP dyed electrode in a cuvette after one hour bias. The electrode was biased at -250 mV vs SCE at pH 7.

photocurrents in the CHyPEMP dyed alumina-Pt electrode trials. This observation demonstrated alumina's ability to attenuate diffusion of aqueous CHyPEMP and/or the concentration of leached CHyPEMP was negligible to the overall photocurrent measured.

Spectroelectrochemical measurements of the dyed alumina-Pt electrode were conducted to determine whether the dyes anchored to the alumina layer were still in electrical contact with the Pt electrode. The absorption of the dyed electrode was continuously monitored over time while the electrode was negatively biased at -250 mV vs SCE (**Figure 2.9a**). Normally, redox studies of photoabsorbers are conducted in nonaqueous solvents to prevent solvent-related redox reactions (e.g. water splitting responsible for hydrogen and oxygen evolution) from limiting the potential applied. However, water was kept as the solvent for this characterization as the dyed alumina-Pt electrode was originally operated in aqueous solution. With this limitation, a low bias was applied to avoid water electrolysis reactions that can affect $[H^+]$ and $[OH^-]$, or the protonation of the dye.

Spectral changes of the electrode can be either due to desorption and diffusion of dyes, changes in the protonation state of the dye due to hydrogen evolution, or the reduction of the dye. A continual decrease in the absorbance at 350 nm supports all hypotheses but the absorbance at 510 nm only decreases for the first 20 minutes and increases beyond its initial absorbance after an hour. From the nearly 1:1 absorbance ratio seen for deprotonated CHyPEMP at 350 nm/510 nm and the loss of ~0.1 absorbance at each peak for the spectrum collected at 20 minutes, it is likely desorption was responsible for most of the absorbance charge in the first 20 minutes. Absorption spectra were baselined to the spectrum obtained at 20 minutes to remove absorbance contributions from the alumina-Pt electrode and desorption of the dye, and the resulting difference spectra were compared to the difference spectrum due to the deprotonation of CHyPEMP (**Figure 2.9b**). The near maintenance of a single isosbestic point at 430 nm after 20 minutes suggests that only one

chemical transition is occurring. The isosbestic point corresponding to a protonation change in CHyPEMP (410 nm) along with the spectral features between 300 nm and 400 nm in the deprotonation difference spectrum disagrees with the difference spectra observed while the electrode was biased, indicative of a species change unrelated to protonation, suggesting CHyPEMP is still in electrical communication with the Pt electrode despite the presence of a 3.5 μm alumina layer. Although alumina is a wide bandgap semiconductor, lateral hole transfers between metal-oxide anchored photoabsorbers offer a mechanism for the observed redox reaction in CHyPEMP.[49]

A related effort to develop a photoelectrochemical sensor was initiated by Dr. Jennifer Glancy and her work in detection of photogenerated protonic species in photoacidic quantum dots using a similar idea to the work discussed in this chapter.[50] Motivated by the work of Dawlaty et. al.,[51] a thin pathlength liquid flow cell with optically transmissive FTO electrodes was constructed to measure solution resistance changes during low frequency electrochemical impedance spectroscopy. The distance between the electrodes, defined by the thickness of a Teflon spacer, varied spacing on the order of hundreds of microns. Decreases in real impedance at low frequency alternating current when the cell was illuminated with 405 nm light was associated with photogeneration of protonic species modeled by a simplified Randles circuit. The simplification incorporated the capacitive component of the Warburg element into the diffuse double layer capacitance with the real impedance reflecting a sum of charge transfer resistance and diffusional resistance. Although the real impedance decreased with illumination of the photoacid, deconvolution of the charge transfer resistance and diffusional resistance is being explored.

Chapter 2.2: Conclusion

Attempts at creating a H^+(aq) sensor were unsuccessful for the application of detecting changes in pH after exciting photoacid or photobases. Although commercial solutions exist to measure pH, a novel requirement for my work required the ability to detect events in the local volume of solution where light absorption occurred. Photoelectrochemical sensors based on the reversible hydrogen electrode were developed but suffered from being in electric contact with the excited-state dye, resulting in photoresponses that are not entirely reflective of Nernstian perturbations to [H^+] but to excited-state electron transfer processes. Efforts to understand similar sensors based on electrochemical impedance spectroscopy are on-going.

Chapter 2.3: Experimental

Electroplating Pt on fluorine doped tin oxide. Fluorine-doped tin oxide glass (TEC15, 2.2 mm thickness, GreatCell Solar Limited) was masked with a small O-ring (~ 3 mm ID) held on with binder clips. Three drops of ~8 mM chloroplatinic acid (~40% Pt, Sigma-Aldrich) was placed within the O-ring and +1 mA current was applied for 2 minutes in a three electrode setup consisting of a Pt wire counter electrode and Ag/AgCl saturated KCl reference electrode. The assembly was disassembled and rinsed with DI water.

Production of CHyPEMP dyed alumina-Pt electrodes. Glass microscope slides (1 mm thickness) were masked with Scotch transparent tape with the features described in **Figure 2.3a**. Pt sputtering was done courtesy of Harold Fu from the Lewis Research group at the California Institute of Technology. A layer of mesoporous alumina was placed atop the sputtered Pt by first applying a rectangular mask over the circular Pt active area and doctor blading an alumina nanoparticle suspension prepared by my graduate predecessor Dr. Joseph M. Cardon. The mask was removed, and the patterned alumina was sintered on a hotplate at its max temperature (~500 ºC). After

assembly of the electrochemical cell, the alumina layer was submerged in 5 mM solution of CHyPEMP overnight, followed by a DI water rinse. CHyPEMP was previously synthesized by my graduate predecessor Dr. Christopher D. Sanborn.

Assembly of electrochemical cell. The following procedure applies to all revisions of the electrochemical cell. The inner bottom of a 10 mL scintillation vial was scribed with a tungsten carbide glass scribe. Several taps with a small, blunt object from the inside of the scintillation vial frees the bottom of the scintillation vial, allowing a septum to be fitted. Neutral cure silicone caulk (Advanced Silicone 2, GE) was applied to the top of the scintillation vial (threaded side), and the vial was inverted onto the transparent Pt electrode, with as much of the Pt bridge covered by the silicone caulk if present. The final assembly had a small weight placed atop of it and the silicone was allowed to cure overnight at room temperature, forming a watertight electrochemical cell. Ports were cut into the septum for reference and counter electrodes.

Synthesis of Methyoxylated Photoacid, MeOPTS. In a round bottom flask, HPTS (5.0 grams, ~9.6 mmol) was dissolved in 80 mL of dimethylsulfoxide. NaOH pellets (0.50 g, ~12.5 mmol) were added and stirred for 30 min at room temperature. Methyl iodide (2.28 g, ~16 mmol) was added and the solution was stirred for 48 h at room temperature. A yellow crude solid was suspended in solution upon addition of 200 mL of ethyl acetate. The product was filtered using vacuum filtration and rinsed with ethyl acetate (2 x 50 mL) followed by acetone (3 x 50 mL). The final crude product was recrystallized with methanol and water to yield a yellow powder. The recrystallized product was characterized when dissolved in D_2O(l) using ^{1}H-NMR spectroscopy (DRX500, Bruker), as a solid powder after drying under vacuum at 60 – 70 °C overnight using FTIR–ATR spectroscopy (FT/IR-4700 equipped with ATR-PRO ONE, JASCO), and as an aqueous solution using electronic

absorption spectroscopy (Duetta, HORIBA). Spectral features were consistent with the methoxylated photoacid, 8-methoxypyrene-1,3,6 trisulfonate (MeOPTS).

Photoelectrochemical Measurements. Electrochemical measurements were conducted using a potentiostat (VSP-300, Biologic) in a three-electrode configuration consisting of a Pt wire counter electrode and either a commercial SCE (CHI150, CH Instruments) or a fritted Ag/AgCl saturated KCl reference electrode. Ag/AgCl saturated KCl reference electrode were prepared by sanding an Ag wire, rinsing it with dilute nitric acid, and rinsing it with copious amounts of DI water, followed by immersing ~3 cm of the bottom of the clean Ag wires in an aqueous 8.25% sodium hypochlorite generic bleach solution for 15 min. After oxidation, the Ag/AgCl wires were rinsed and aged in ultrapure water overnight. A glass frit (Vycour 7930) was attached to a similar outer diameter glass tube with Olefin heat shrink tubing and the Ag/AgCl wire was placed into the tube along with a saturated solution of KCl prepared from ultrapure water. The glass body of the Ag/AgCl reference electrode was coated in black nail polish to prevent photodegradation of the AgCl wire. Absorption measurements were measured with a UV-Vis spectrophotometer (Cary60, Agilent).

Chapter 3: Photoelectrochemical Evaluation and Characterization of Membrane-Liquid Junction Assemblies

To enable generation of large photovoltaic effects, an important property of many, but not all,[4,12,52] electronic semiconductors is the existence of an electrostatic space–charge depletion region that results in the property of current rectification.[12,52] Space–charge depletion regions are typically formed by diffusing dopants into a surface of an oppositely doped semiconductor to create a buried pn-junction, or by contacting the semiconductor with a metal whose work function differs significantly from that of the semiconductor, which creates a Schottky junction at the semiconductor|metal interface. Photon absorption results in net generation of mobile electron and hole charged species that are effectively separated by the space–charge depletion region and subsequently collected at selective contacts. Differences in the electrochemical potentials of electrons and holes at the contacts can be used to power electronic devices, and there is no net generation of chemical species. Analogous to the creation of a Schottky junction, one can also contact one side of an electronic semiconductor with a liquid electrolyte solution that contains redox-active molecules to form a space–charge depletion region at the semiconductor|liquid interface.[53] Photon absorption also results in net generation of mobile electron and hole charged species, however, uniquely these species react with redox-active molecules to ultimately generate electronic power, and form no net chemical species, or drive net chemical redox reactions.[5,54] The benefit of these photoelectrochemical constructs is that formation of a space–charge depletion region is a noninvasive process because in general liquid electrolytes inherently conformally coat even nanostructured electrode surfaces. This means that pinhole-free junctions that do not greatly perturb the surface chemistry of the semiconductor are possible. Notable fundamental science studies by Lewis and colleagues showed that the magnitude of the open-circuit photovoltage (V_{oc})

of a semiconductor–liquid junction scales directly with the reduction potential of the liquid electrolyte,[55,56] which altered the interfacial barrier height, the magnitude of the built-in electric (electrostatic) potential, and the width of the space–charge depletion region. They used a semiconductor consisting of high-quality crystalline silicon, doped p-type or n-type and that contained one ohmic metallurgical back contact to provide low-impedance charge collection to an external circuit, liquid electrolyte consisting of acetonitrile or methanol containing $LiClO_4$, and a redox couple consisting of metallocenes/metalloceniums or viologens that were all mutually compatible and stable. Follow-on work in part overcame instability in aqueous electrolytes through methylation of the freshly-etched Si(111) surface[57] and furthered these studies by implementing liquid junctions at both the front and back contacts to the semiconductor.[58,59] Leveraging this knowledgebase and expanding it to the analysis of dye-sensitized ion-exchange-membrane–liquid-junction assemblies is the aim of the work reported herein.

Chapter 3.1: Donnan Membrane Potential and Donnan Exclusion

It is well-known in membrane science that electrostatic space–charge regions also form across permselective-membrane|solution and membrane|membrane interfaces.[60,61] In the presence of various charged species, resulting *steady-state* electric potential differences are reasonably quantified by the Henderson and Goldman equations.[62–65] When only two species of opposite sign are the dominant mobile charged species at a membrane|solution interface, such as when the solution contains only one soluble salt, these equations quantify *equilibrated* Donnan potentials.

In this case, and by analogy to space–charge regions in electronic semiconductors, Donnan theory predicts that a thermally and electrochemically equilibrated electric potential difference exists across each interface.[66,67] Processes to attain thermal and electrochemical equilibration of mobile charged species across liquid junctions are the same for semiconductors and ion-exchange membranes (**Figure 3.1**). Driven by gradients in the activity, and therefore chemical potential, of mobile charged species, they diffuse across said interfaces. This results in charge separation, and thus formation of a space–charge region, meaning that electric fields and electric potential differences exist to oppose the chemical potential difference of the mobile charged species. When these potentials are equal and opposite, the species has reached electrochemical equilibrium, meaning that the species has a spatially invariant electrochemical potential. Equilibrated electric potential

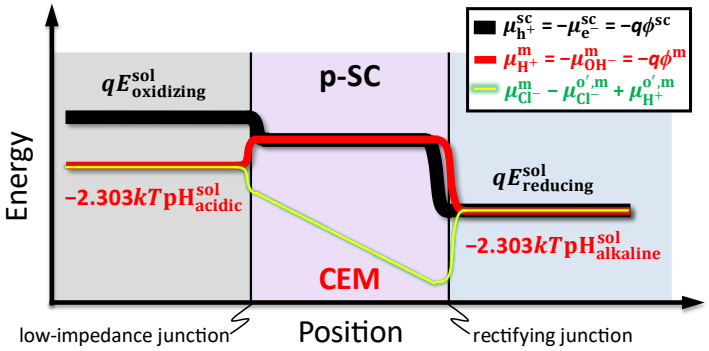

Figure 3.1. Energy-level diagram for a semiconductor–liquid-junction (sc) device, which is analogous to a Schottky-junction device, and consists of a p-type semiconductor (p-SC) wetted on each side by a solution that contains redox species with reduction potential, E_i^{sol}. The chemical potential of electrons, $\mu_{e^-}^{sc}$, and holes, $\mu_{h^+}^{sc}$, at each location are equal and opposite, which signifies chemical equilibrium at each location. The magnitude of $\mu_{e^-}^{sc}$ at each location is equal to the magnitude of the electric potential contribution, $q\Phi^{sc}$, meaning that each species has a spatially invariant electrochemical potential (Fermi level), which signifies electrochemical equilibrium across the entire device geometry. Also illustrated is a membrane–liquid-junction (m) device that consists of a cation-exchange membrane (CEM) wetted on each side by a solution at a fixed pH value, pH_i^{sol}, which results in analogous properties for protons, $\mu_{H^+}^{m}$, hydroxides, $\mu_{OH^-}^{m}$, and their respective electric potential contribution, $q\Phi^{m}$. Notable differences between a desired semiconductor–liquid-junction device and a membrane–liquid-junction device are that *(i)* Φ^{sc} predominantly varies in the semiconductor phase, rather than in the solution phases, while Φ^{m} predominantly varies in the solution phases, rather than in the membrane phase; *(ii)* a perfectly ohmic contact cannot form at the low-impedance charge-collection junction of the CEM because that would completely remove Donnan exclusion, which is required for the membrane to be charge selective for cations, like a p-type semiconductor; and *(iii)* ions of opposite charge to the mobile charged species, e.g. Cl^- counterions, necessarily infiltrate into the CEM as coions and result in non-equilibrium conditions across the entire device geometry. For ease of visualization, the chemical potential of Cl^-, $\mu_{Cl^-}^{m}$, is referenced to the standard concentration chemical potential of H^+, $\mu_{H^+}^{o',m}$, where "concentration" is commonly used for equilibrium constants and is analogous to "formal" for reduction potentials.

differences are analogous to space–charge regions that are responsible for the current–potential behavior of both rectifying charge-separation junctions and low-impedance charge-collection junctions in electronic semiconductors. Control over these electrostatic properties are thus critical to realization of effective ionic diodes, which further motivates development of design principles for light-to-ionic power conversion using dye-sensitized ion-exchange membranes.

Donnan theory is used to quantify spatial distributions of ions and electric potentials across a membrane interface, or across a thin, porous membrane separator when specifically in the presence of other charged species that cannot cross the interface, e.g. a single salt species HCl(aq). Transport of each mobile ion, e.g. H^+ and Cl^-, down its gradient in electrochemical potential results in formation of a space–charge region, due to the charged species that cannot cross the interface, whose single associated electric potential difference satisfies electrochemical equilibrium for each mobile ion. In this case, the electrochemical potential of H^+ on either side of the membrane interface is equal, which also satisfies the condition that the electrochemical potential of Cl^- on either side of the membrane interface is equal, as follows,

$$\bar{\mu}_i^{\mathrm{s}} = \bar{\mu}_i^{\mathrm{m}} \tag{3.1}$$

$$\mu_i^{\mathrm{s}} + z_i F \phi^{\mathrm{s}} = \mu_i^{\mathrm{m}} + z_i F \phi^{\mathrm{m}} \tag{3.2}$$

$$\mu_i^{\mathrm{o,s}} + RT \ln a_i^{\mathrm{s}} + z_i F \phi^{\mathrm{s}} = \mu_i^{\mathrm{o,m}} + RT \ln a_i^{\mathrm{m}} + z_i F \phi^{\mathrm{m}} \tag{3.3}$$

where $\bar{\mu}_i$ is the electrochemical potential of species i, μ_i is the chemical potential, z_i is the valency, ϕ is the electric potential, μ_i^{o} is the standard chemical potential, a_i is activity, and the superscripts s and m refer to species in the solution phase and in the membrane phase, respectively.[61] Assuming the reasonable assumption that μ_i^o in each phase is the same, the interfacial (int) Donnan (D)

electric potential difference between the bulk quasi-neutral region of the solution *versus* the bulk quasi-neutral region of the membrane, $\phi_{\mathrm{D}}^{\mathrm{int}}$, is calculated as follows,

$$RT \ln a_i^{\mathrm{s}} + z_i F \phi^{\mathrm{s}} = RT \ln a_i^{\mathrm{m}} + z_i F \phi^{\mathrm{m}} \tag{3.4}$$

$$\phi^{\mathrm{s}} - \phi^{\mathrm{m}} = \phi_{\mathrm{D}}^{\mathrm{int}} = -\frac{RT}{z_i F} \ln \frac{a_i^{\mathrm{s}}}{a_i^{\mathrm{m}}} \tag{3.5}$$

$$\phi_{\mathrm{D}}^{\mathrm{int}} = -\frac{RT}{F} \ln \frac{a_{\mathrm{H}^+}^{\mathrm{s}}}{a_{\mathrm{H}^+}^{\mathrm{m}}} = -\frac{RT}{F} \ln \frac{a_{\mathrm{Cl}^-}^{\mathrm{m}}}{a_{\mathrm{Cl}^-}^{\mathrm{s}}} \tag{3.6}$$

where *z* is the charge of the majority-carrier counterion species and *a* is the activity of the majority-carrier species on each side of the interface. Because a wetted ion-exchange membrane has two membrane|solution interfaces, there are two $\phi_{\mathrm{D}}^{\mathrm{int}}$ that contribute to the measured net Donnan membrane potential, $\phi_{\mathrm{D}}^{\mathrm{mem}}$. Using **Equation 3.5**, and the fact that the bulk quasi-neutral region of the membrane is a common reference state, leads to the following,

$$\phi_{\mathrm{D}}^{\mathrm{mem}} = \left(\phi_{\mathrm{D}}^{\mathrm{int,WE}}\right) + \left(-\phi_{\mathrm{D}}^{\mathrm{int,CE}}\right) = \frac{RT}{zF} \ln \frac{a^{\mathrm{sol,CE}}}{a^{\mathrm{sol,WE}}} = \frac{(\ln 10)RT}{zF} (\mathrm{pX}^{\mathrm{WE}} - \mathrm{pX}^{\mathrm{CE}}) \tag{3.7}$$

where pX stands for "–log a^{sol}," WE stands for nearer to the working electrode, and CE stands for nearer to the counter electrode. The concept of a membrane reference state and the form of **Equations 3.5 and 3.7** are motivated by those commonly used to represent the Nernst reduction potential of an electrode|solution interface, $E_{\mathrm{N}}^{\mathrm{int}}$, and the net Nernst redox potential of an electrochemical cell, $E_{\mathrm{N}}^{\mathrm{redox}}$, as follows,

$$E_{\mathrm{N}}^{\mathrm{int}} = E_{\mathrm{N}}^{\mathrm{o,int}} - \frac{RT}{nF} \ln \left(\frac{\left(a_{\mathrm{red}}^{\mathrm{sol}}\right)^{\nu_{\mathrm{red}}}}{\left(a_{\mathrm{ox}}^{\mathrm{sol}}\right)^{\nu_{\mathrm{ox}}}} \right) = E_{\mathrm{N}}^{\mathrm{o\prime,int}} - \frac{RT}{nF} \ln \left(\frac{\left(c_{\mathrm{red}}^{\mathrm{sol}}\right)^{\nu_{\mathrm{red}}}}{\left(c_{\mathrm{ox}}^{\mathrm{sol}}\right)^{\nu_{\mathrm{ox}}}} \right) \tag{3.8}$$

$$E_{\mathrm{N}}^{\mathrm{redox}} = \left(E_{\mathrm{N}}^{\mathrm{int,WE}}\right) + \left(-E_{\mathrm{N}}^{\mathrm{int,CE}}\right) = \left(E_{\mathrm{N}}^{\mathrm{o\prime,int,WE}} - E_{\mathrm{N}}^{\mathrm{o\prime,int,CE}}\right) + \frac{RT}{nF} \ln \left(\frac{\left(c_{\mathrm{ox}}^{\mathrm{WE}}\right)^{\nu_{\mathrm{ox}}^{\mathrm{WE}}} \left(c_{\mathrm{red}}^{\mathrm{CE}}\right)^{\nu_{\mathrm{red}}^{\mathrm{CE}}}}{\left(c_{\mathrm{red}}^{\mathrm{WE}}\right)^{\nu_{\mathrm{red}}^{\mathrm{WE}}} \left(c_{\mathrm{ox}}^{\mathrm{CE}}\right)^{\nu_{\mathrm{ox}}^{\mathrm{CE}}}} \right) \tag{3.9}$$

where the various redox species together make up the reaction quotient, $Q = \frac{(c_{ox}^{WE})^{\nu_{ox}^{WE}}(c_{red}^{CE})^{\nu_{red}^{CE}}}{(c_{red}^{WE})^{\nu_{red}^{WE}}(c_{ox}^{CE})^{\nu_{ox}^{CE}}}$.

Donnan exclusion, or the extent of ion exclusion for an ion-selective membrane, is a property that is derived from the formation of a Donnan membrane potential. Since all electrolyte species contribute towards the same Donnan membrane potential, the relationship below follows **Equation 3.6**.

$$a_{H^+}^{m}\, a_{Cl^-}^{m} = a_{H^+}^{s}\, a_{Cl^-}^{s} \tag{3.10}$$

Since cation-exchange membranes, like Nafion, contain negatively charged fixed groups (R^-), the following charge conservation relationships exist,

$$a_{H^+}^{s} = a_{Cl^-}^{s} \tag{3.11}$$

$$a_{H^+}^{m} = a_{R^-}^{m} + a_{Cl^-}^{m} \tag{3.12}$$

which when coupled with **Equation 3.10**, result in the following equations,

$$(a_{Cl^-}^{m})^2 + a_{R^-}^{m}\, a_{Cl^-}^{m} - (a_{Cl^-}^{s})^2 = 0 \tag{3.13}$$

$$a_{Cl^-}^{m} = \frac{-a_{R^-}^{m} + \sqrt{(a_{R^-}^{m})^2 + 4\,(a_{Cl^-}^{s})^2}}{2} = \frac{a_{R^-}^{m}}{2}\left(\sqrt{1 + 4\left(\frac{a_{Cl^-}^{s}}{a_{R^-}^{m}}\right)^2} - 1\right) \tag{3.14}$$

If the square root term is approximated to two non-zero terms in the Maclaurin series, an approximation for the activity of mobile anions in the membrane can be calculated as follows,

$$a_{Cl^-}^{m} \approx \frac{a_{R^-}^{m}}{2}\left(1 + 2\left(\frac{a_{Cl^-}^{s}}{a_{R^-}^{m}}\right)^2 - 1\right) = \frac{(a_{Cl^-}^{s})^2}{a_{R^-}^{m}} \tag{3.15}$$

where **Equation 3.15** is the more general version of **Equation 3.16** based on species concentrations, and which indicates that $a_{Cl^-}^{s} \ll a_{R^-}^{m}$ must be satisfied in order to achieve

significant Donnan exclusion of coion anions, e.g. Cl^-, from the membrane to result in primarily cationic conduction.

Chapter 3.2: Modifications to Prior Experimental Setup

Rationale for using identical electrolyte species. We recently reported photovoltaic action via visible-light excitation of a PFSA membrane covalently modified with HPTSA,[20] an analog of the well-known photoacid HPTS (**Figure 3.7b**).[24] Observed photocurrent densities were as large as 100 μA/cm^2, however photovoltages were only ~1 mV. While that work set the benchmark for this new class of functional materials, the experimental setup and protocols used to quantify photovoltaic behavior were imperfect. In particular, the aqueous electrolytes used were far from ideal because they consisted of strong acid (H_2SO_4) separated from strong base (NaOH) by only a cation-exchange membrane (modified Nafion). For protonic photovoltaics based on cation-exchange membranes, it is *detrimental* to use concentrated base to try to maximize chemical potential differences of each mobile charged species, and thus the electric potential difference, across the rectifying charge-separation junction, because it results in unstable acid–base gradients due to opposing transport of H^+ toward the alkaline electrolyte and Na^+ toward the acidic electrolyte. This is evidenced by the magnitude of the net built-in electric potential difference being significantly smaller than that predicted by **Equation 3.7**, when the concentration of protons on each side of the membrane is used as a surrogate for the activity in the numerator and the denominator of the reaction quotient fraction. And because Nafion and related cation-exchange membranes exhibit similar abilities to transport H^+ and Na^+, these conditions suggest that over time there was a substantial loss in the pH difference across the membrane, which was not

immediately noticeable due to the large volumes of solution and large concentrations of acid and base used.

Comparatively, for analogous electronic photovoltaic semiconductor constructs, it is *beneficial* to try to maximize chemical potential differences of each mobile charged species, and thus the electric potential difference, across the rectifying charge-separation junction and it is *beneficial* to try to minimize chemical potential differences of each mobile charged species, and thus the electric potential difference, across the low-impedance charge-collection junction. However, for protonic photovoltaics based on cation-exchange membranes it is *detrimental* to use concentrated acid to try to minimize chemical potential differences of each mobile charged species, and thus the electric potential difference, across the low-impedance charge-collection junction. This is because Donnan exclusion, which results in a substantial difference in the concentration of one ion charge type – the coion – over the other ion charge type – the counterion – is poor when the activity of salt species in the contacting aqueous electrolyte is similar to the activity of fixed-charge groups in the ion-exchange membrane. The extent of Donnan exclusion can be approximated by the following equation,

$$\left[\mathrm{Coion}^{\mathrm{m}}_{-/+}\right] = \frac{\left[\mathrm{Salt}^{\mathrm{s}}_{\pm}\right]^2}{\left[\mathrm{Fixed}^{\mathrm{m}}_{-/+}\right]} \tag{3.16}$$

where $\left[\mathrm{Coion}^{\mathrm{m}}_{-/+}\right]$ is the coion anion (cation) concentration in a cation-exchange (anion-exchange) membrane (m), $\left[\mathrm{Salt}^{\mathrm{s}}_{\pm}\right]$ is electrolyte salt concentration in solution (s), and $\left[\mathrm{Fixed}^{\mathrm{m}}_{-/+}\right]$ is the concentration of fixed negatively-charged (positively-charged) groups in a cation-exchange (anion-exchange) membrane.[61] When $\left[\mathrm{Salt}^{\mathrm{s}}_{\pm}\right] \geq \left[\mathrm{Fixed}^{\mathrm{m}}_{-/+}\right]$, $\left[\mathrm{Coion}^{\mathrm{m}}_{-/+}\right] \approx \left[\mathrm{Salt}^{\mathrm{s}}_{\pm}\right]$ and thus no Donnan exclusion exists across the interface, resulting in poor permselectivity based on ion charge

type. Nafion NR-212 has $\left[\text{Fixed}^{\text{m}}_{-/+}\right] \approx 1$ M,[68,69] which is approximately the value that we determined for both Nafion NR-212 and our modified Nafion membranes based on measurements of ion-exchange capacity in our prior work.[13] Since we used aqueous 1 M H_2SO_4 and 1 M NaOH electrolytes in our prior work,[20,22] this meant that Donnan exclusion was poor and that SO_4^{2-} and OH^- coions were likely present in the modified Nafion membranes at concentrations in the hundreds of millimolar range, or larger.[70]

When different concentrations of salt species are present in each aqueous electrolyte that wets an ion-exchange membrane, the concentration of partially Donnan excluded coions in the membrane, and their associated mobile counterions, differs at each membrane|solution interface, resulting in diffusion of neutral electrolyte species down its concentration gradient and ultimately formation of a steady-state liquid-junction (LJ) electric potential difference ($\phi_{\text{LJ}}^{\text{mem}}$) across, but within, the membrane (mem). Therefore, similar to electric potentials across pH probes,[46] electric potentials across ion-exchange membranes consist of at least three contributions (2 $\phi_{\text{D}}^{\text{int}}$ (**Equations 3.5 and 3.7**) and 1 $\phi_{\text{LJ}}^{\text{mem}}$), where the presence of a nonzero value for $\phi_{\text{LJ}}^{\text{mem}}$ is indicative of ion crossover and means that the system has not reached electrochemical equilibrium. Ion crossover can be further slowed, even to the point of $\phi_{\text{LJ}}^{\text{mem}} = 0$, when a membrane affords additional means for selectivity of one charge type over the other. For example, perfect ion selectivity is thought to be possible when extremely large polyelectrolyte counterions are used, because size exclusion prevents them from existing as coions in the ion-exchange membrane or using pinhole-free monolayer materials like graphene and boron nitride, because they only allow for transport of H^+ via quantum mechanical tunneling.[71,72] In these cases, the processes and outcome of forming interfacial space–charge regions to modulate ion-transport properties are

identical to those that occur at interfaces of solid-state electronic semiconductors to modulate electron-transport properties.

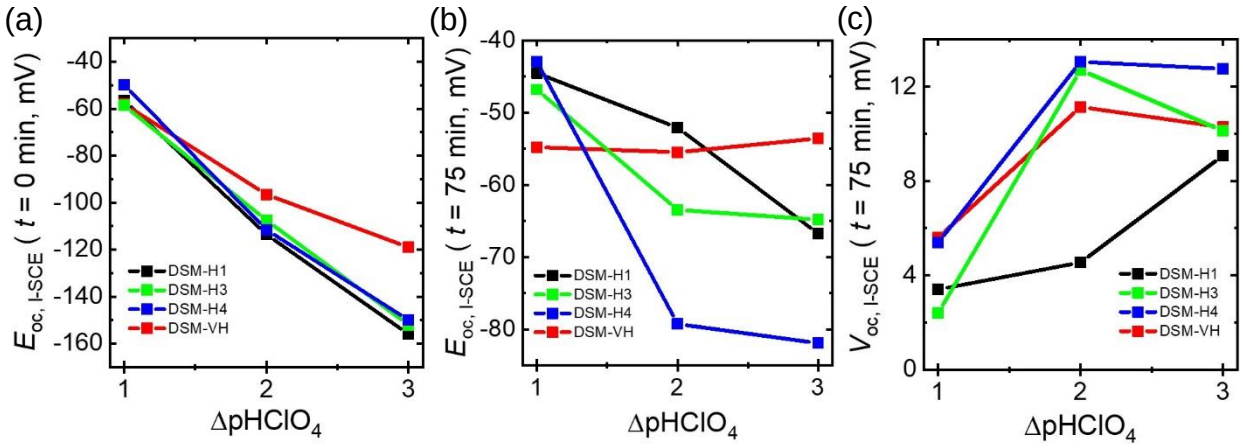

Figure 3.2. **(a)** Open-circuit potential (E_{oc}) recorded immediately after adding electrolyte, **(b)** interpolated E_{oc} values at 75 min into the experiment simulated from a best fit of E_{oc} values measured in the dark, and **(c)** open-circuit photovoltage (V_{oc}) recorded 75 min into the experiment as a function of the difference in $pHClO_4$ across the membrane measured between two nominally identical salt-leaking saturated calomel electrodes (l-SCEs) positioned across several highly dyed HPTSA-modified PFSA under various conditions of 10 mM || 10^-(ΔpHClO4 -1) mM HClO4(aq) (pHClO4 2 || (2 + ΔpHClO4)). We define $pHClO_4$ as "–log[$HClO_4$]", where [$HClO_4$] is the concentration of $HClO_4$. Similar concentrations of HPTSA were used to synthesize **DSM-H1** through **DSM-H4**, while the HPTSA concentration was 20 times larger for the synthesis of **DSM-VH**.

Rationale for adopting externally-referenced vs internally-referenced electrodes. Prior studies of HPTSA-modified PFSA used two nomically identical saturated calomel electrodes (SCEs) to sense potential differences across the membrane as a function of ionic current passing through the membrane.[20–22] The reduction potential of these *photoinactive* SCEs was dictated by the activity of Cl^-(aq) near the electrode surface, which was fixed based on the concentration of Cl^-(aq) present in the fritted tube, resulting in measured values for the open-circuit potential (E_{oc}) being equal to the net electric potential difference across the membrane (see **Equation 3.17**). For our work herein, experiments were initially conducted using SCEs. Although initial values of E_{oc} (**Figure 3.2a**) were in agreement with Donnan theory, i.e. ~59 mV per difference in pH between the room temperature acidic aqueous electrolytes that wetted the membrane, measured E_{oc} values changed over time and were unstable on the timescale of hours (**Figure 3.2b and 3.4a**). To

quantify the open-circuit photovoltage (V_{oc}), a time-dependent baseline was simulated by best-fitting E_{oc} values measured in the dark to a sum of two exponential decays (**Figure 3.4a**). For several HPTSA-modified PFSA with high dye density (OD_{405nm} > 4), measured values for V_{oc} after 60 min of illumination were positive in sign (**Figure 3.2c and 3.4a**), consistent with a decrease in the net built-in electric potential across the membrane and behavior that is expected based on the theory of electronic solar cells. We observed similar behavior in our prior studies.[20–22] It was apparent that higher concentrations of HPTSA used to synthesize **DSM-VH** resulted in larger deviations between experimental E_{oc} values and those predicted by Donnan theory, since HPTSA replaces fixed charge groups in PFSA, but no clear correlations were apparent among V_{oc} values and dye density. Results from a series of follow-on measurements supported that these analyses and trends were complicated, at least in part, by transient changes in the concentration of KCl(aq) that wetted the membrane due to the slow introduction of KCl(aq) into the concentrated and dilute electrolyte chambers via diffusion from the saturated KCl(aq) SCEs. Leakage of salt from the SCEs was supported by measurements of the conductance of an aqueous electrolyte containing an immersed SCE (**Figure 3.4b**).

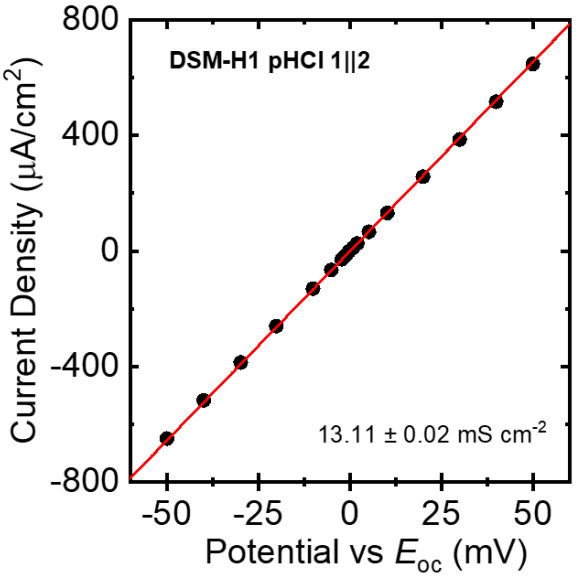

Figure 3.3. Current density versus potential data obtained from four-electrode stepwise chronoamperometry measurements of **DSM-H1** using two Ag/AgCl potential-sensing wires under conditions of 100 mM HCl||10 mM HCl(aq) (pHCl 1||2) in the dark. The area-specific resistance calculated from the slope of these data equals ~76 Ω-cm², which agrees well with the expected bulk-electrolyte-limited area-specific resistance of ~25 Ω-cm², given that in the dilute electrolyte (10 mM HCl; σ ≈ 4 mS cm⁻¹) the electrode–membrane spacing was ~1 mm.

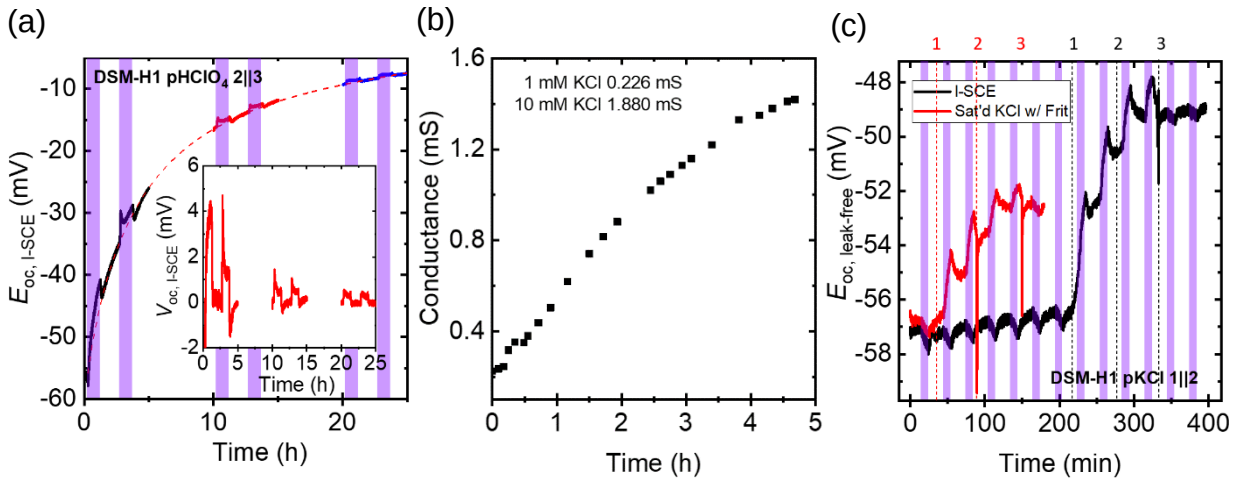

Figure 3.4. (a) Open-circuit potential (E_{oc}) over time measured between two salt-leaking saturated calomel electrodes (l-SCEs) positioned across **DSM-H1** under conditions of 10 mM||1 mM $HClO_4$(aq) (pHClO_4 2||3). The inset shows values for the open-circuit photovoltage (V_{oc}) baseline corrected for changes in E_{oc} values over time using a sum of two exponential decays to best-fit E_{oc} values measured in the dark, highlighting their generally positive values. Short-circuit photocurrent measurements (data not shown) were performed during regions where E_{oc} values were not recorded. **(b)** Conductance measured over time for a 1 mM KCl(aq) solution containing an l-SCE as a KCl leakage source, and with standard reference values measured for KCl(aq) indicated. **(c)** E_{oc} over time measured between two so-called leak-free Ag/AgCl electrodes (lf-Ag/AgCl) across **DSM-H1** under conditions of 100 mM||10 mM KCl(aq) (pKCl 1||2) and in the presence of an external KCl(aq) source. At Event 1, an SCE (black dataset) and a fritted tube filled with saturated KCl(aq) (red dataset) were introduced into the dilute electrolyte chamber as passive KCl(aq) leakage sources. At Event 2, the respective KCl(aq) sources were removed. At Event 3, the electrolyte in each chamber was homogenized by cycling the electrolyte with a pipette. Positive V_{oc} values are dominant during transient salt introduction and/or homogenization; negative V_{oc} values are dominant for the quiescent homogenized solutions. Regions colored in purple indicate the times when the membrane was illuminated.

To further investigate the impact of transient salt leakage on measured electric potential differences, E_{oc} values were measured between two so-called leak-free Ag|AgCl|KCl(aq, 3.4 M) electrodes (Innovative Instruments, LF-2) with timed introduction and removal of SCEs or a fritted tube filled with saturated KCl(aq) into both the concentrated and dilute electrolyte chambers in order to replicate the salt-leakage behavior from SCEs used as sensing electrodes in prior experiments (**Figure 3.4c**). Before *Event 1*, no KCl(aq) source was present and E_{oc} values were found to be rather stable and illumination resulted in an increase in the magnitude of E_{oc} values, resulting in negative values for V_{oc}. At *Event 1*, KCl(aq) sources were immersed into each electrolyte and shortly thereafter the rate of change of E_{oc} with respect to time increased significantly. This was accompanied by a change in the sign of V_{oc} values under illumination,

where now the magnitude of E_{oc} values decreased, behavior that is consistent with effects that occur in traditional electronic solar cells, and that we observed previously.[20–22] At *Event 2*, KCl(aq) sources were carefully removed, so as to not significantly agitate the solution, and the sign of V_{oc} values remained unchanged. At *Event 3*, the electrolyte in each chamber was homogenized by cycling the solutions with a pipette, resulting in behavior similar to that occurring prior to *Event 1*, where V_{oc} values were opposite ("reverse") of those that occur in traditional electronic solar cells. This supports that leakage of salt into the electrolytes and its transient interaction with membrane|solution interfaces were responsible for effects observed in our prior work.[20–22]

A single-junction sensing electrode, for example an SCE, features a redox couple whose chemical potential is dictated by an internal reference electrolyte, typically containing high concentrations of salt and other species when appropriate. This internal reference electrolyte is separated from the experimental electrolyte by a ceramic frit that somewhat slows exchange of electrolyte species but is insufficient at doing so for our studies (**Figures 3.4a**). Therefore, we considered using double-junction sensing electrodes, which each contain a fritted chamber filled with experimental electrolyte that is placed between the single-junction sensing electrode and the experimental electrolyte to decrease the rate of cross-contamination between the internal reference electrolyte and the experimental electrolyte. We also considered using so-called leak-free Ag|AgCl|KCl(aq, 3.4 M) sensing electrodes, which each contain a somewhat conductive (<10 kΩ), but non-porous, junction to slow cross-contamination. We observed that leak-free electrodes exhibited long equilibration times that resulted in less-certain baseline values for E_{oc} when the electrolyte was not KCl and/or when the electrolyte concentration was less than 10 mM (pX = 2). Moreover, in the absence of a membrane, theoretical E_{oc} values and E_{oc} values measured between a double-junction sensing electrode or a leak-free sensing electrode *versus* an Ag/AgCl wire each

immersed in a single aqueous electrolyte differed significantly (**Table 3.1**). These disparities are likely the result of liquid-junction potentials that formed between the internal reference electrolyte and experimental electrolyte and are too large for accurate measurement of membrane potentials. Because Ag/AgCl wires immersed into a chloride-containing electrolyte rapidly reach electrochemical equilibrium and cannot form a liquid-junction potential, they were determined to be the potential-sensing electrode of choice for our studies.

Table 3.1. Open-circuit potential (E_{oc}, in mV) measured for various electrodes (left electrode: *SCE*, leak-free Ag/AgCl(KCl) electrode, custom single-junction or double-junction acidic Ag/AgCl(HCl) electrode) *versus* an Ag/AgCl wire immersed into beakers containing solutions of various concentrations of Cl^-(aq) (right electrode), calculated values (in mV), and differences (in mV) attributed to liquid-junction potentials that form across electrode frits (ϕ_{LJ}^{frit}).

Electrochemical Cell Line Notation (Compartment A ‖ Compartment B ‖ Compartment C *(if necessary)*)	E_{oc} *(measured)*	$E_N^{o',redox}$ *(see first* row*)*	$-\frac{RT}{F}\ln Q$ *(with T = 25 °C; see* ***Equation 4****)*	ϕ_{LJ}^{frit} *(calculated using* ***Equations 4 and 6****)*
Pt(s) | *Hg_2Cl_2(s)* | *Hg(l)* | *KCl(aq,* ***sat'd****)* ‖ KCl(aq, **sat'd ≈ 4.8 M**) | AgCl(s) | Ag(s)	+45	+45	0	0
Pt(s) | *Hg_2Cl_2(s)* | *Hg(l)* | *KCl(aq,* ***sat'd****)* ‖ KCl(aq, **10 mM**) | AgCl(s) | Ag(s)	-97	+45	-159	+17
Pt(s) | *Hg_2Cl_2(s)* | *Hg(l)* | *KCl(aq,* ***sat'd****)* ‖ KCl(aq, **1 mM**) | AgCl(s) | Ag(s)	-143	+45	-218	+30
Ag(s) | AgCl(s) | KCl(aq, **3.4 M**) ‖ HCl(aq, **10 mM**) | AgCl(s) | Ag(s)	-108	0	-150	+42
Ag(s) | AgCl(s) | KCl(aq, **3.4 M**) ‖ HCl(aq, **1 mM**) | AgCl(s) | Ag(s)	-133	0	-209	+76
Ag(s) | AgCl(s) | HCl(aq, **1 M**) ‖ HCl(aq, **10 mM**) | AgCl(s) | Ag(s)	-180	0	-118	-62
Ag(s) | AgCl(s) | HCl(aq, **1 M**) ‖ HCl(aq, **1 mM**) | AgCl(s) | Ag(s)	-289	0	-178	-111
Ag(s) | AgCl(s) | HCl(aq, **1 M**) ‖ HCl(aq, **10 mM**) ‖ HCl(aq, **10 mM**) | AgCl(s) | Ag(s)	-198	0	-118	-80
Ag(s) | AgCl(s) | HCl(aq, **1 M**) ‖ HCl(aq, **1 mM**) ‖ HCl(aq, **1 mM**) | AgCl(s) | Ag(s)	-313	0	-178	-135

Chapter 3.3: Consequences of Ag/AgCl Reference Electrodes and Interpretation of Photovoltages

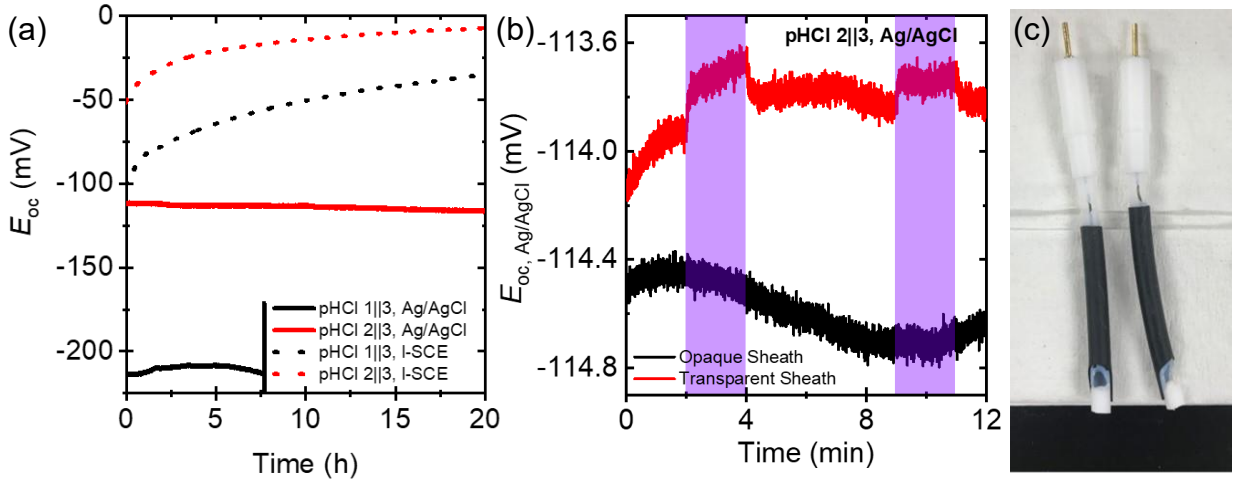

Figure 3.5. (a) Open-circuit potential (E_{oc}) over time measured between two Ag/AgCl wires (solid) or two salt-leaking KCl-saturated calomel electrodes (l-SCE, dashed) positioned across **DSM-H1** under various conditions of *x* mM || 1 mM HCl(aq) (pHCl –log(*x*)||3). E_{oc} is a convolution of the difference in reduction potential at the electrodes (E_N^{redox}) and contributions due to differences in electric potential between the electrodes (ϕ_i), where for Ag/AgCl wires, $E_N^{redox} \neq 0$, and for SCEs, $E_N^{redox} \approx 0$. Data acquisition was stopped at ~7.5 h for the solid black dataset. **(b)** E_{oc} over time measured between two Ag/AgCl wires (sheathed with a black tube (black) and a transparent tube (red)) positioned across unmodified Nafion NR-212 under conditions of 10 mM||1mM HCl(aq) (pHCl 2||3) and periodically illuminated with 150 mW/cm^2 of 405 nm laser light (purple bars). **(c)** Photograph of the two Ag/AgCl wires, each sheathed by a black tube.

For subsequent experiments and results, Ag/AgCl wires were utilized as sensing electrodes to eliminate sources of salt leakage. Use of Ag/AgCl wires limited electrolyte options to those that contained Cl^-, e.g. HCl(aq) and KCl(aq), but resulted in E_{oc} values that were quite stable on the order of >10 h for conditions where differences in the concentration of HCl across the membrane were as large as two orders-of-magnitude, i.e. pHCl 1||3 (**Figure 3.5a)**. Although coion crossover was greatly attenuated with this setup, osmosis was not, so much so that after 5 h, transport of water from the dilute electrolyte chamber to the concentrated electrolyte chamber was visibly evident (**Figure 3.6a**). Because osmosis and transient introduction of salt are each dynamic processes that should result in similar effects on E_{oc} values, the effects of osmosis on V_{oc} values were also assessed. For this, we compared V_{oc} values obtained under conditions of pHCl 1||3, where

an osmotic pressure of 44 atm existed, to V_{oc} values measured under equiosmolar conditions, where to account for the van't Hoff factor of HCl(aq), 198 mM of sucrose – a solute that under the aqueous conditions studied is non-dissociable, non-reducing, and uncharged – was introduced to the 1 mM HCl(aq) solution (**Figure 3.6b**). The resulting V_{oc} behavior both with and without added osmolyte was essentially the same, suggesting that transient osmotic processes do not explain the observed "reverse" photovoltaic behavior.

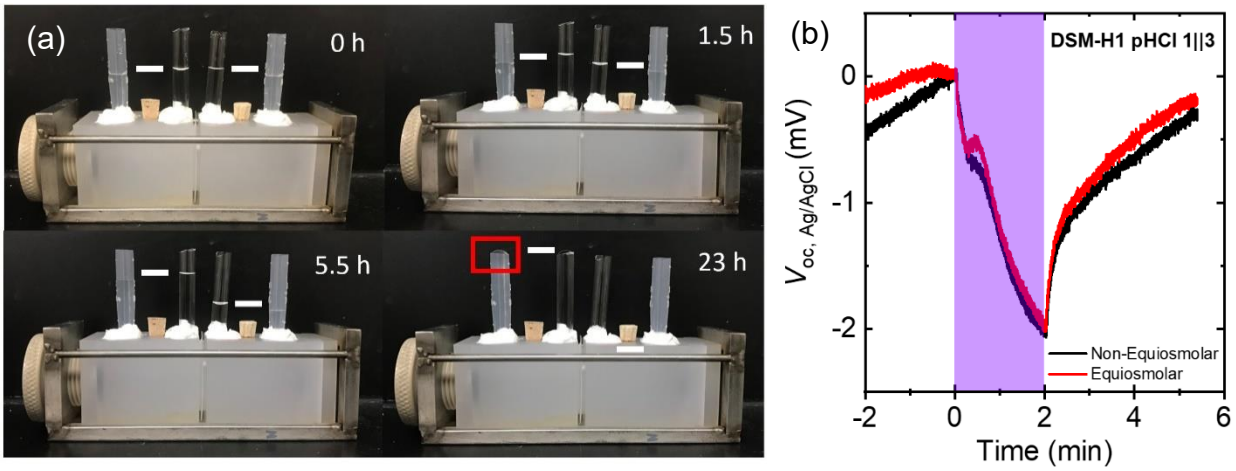

Figure 3.6. (a) Photographs of the electrochemical cell at the indicated times showing the effect of osmosis through **DSM-H1** under conditions of 100 mM||1 mM HCl(aq) (pHCl 1||3) without illumination. White bars indicate the electrolyte level in each chamber. By 23 h, the chamber that initially contained the larger concentration (concentrated) electrolyte began to overflow, as indicated by the red box. **(b)** Open-circuit photovoltage (V_{oc}) over time measured between two Ag/AgCl wires positioned across **DSM-H1** under conditions of 100 mM||1 mM HCl(aq) (pHCl 1||3) and illuminated with 170 mW/cm^2 of 405 nm laser light (purple bar) and in the presence of a 44 atm osmotic pressure difference (black) and zero osmotic pressure difference (red) due to the presence of sucrose in the dilute electrolyte chamber. Each measurement was subtracted by the open-circuit potential value at the start of the illumination event to obtain V_{oc}.

AgCl wires are also known to undergo photochemical reactions,[73] and therefore Ag/AgCl wires were initially sheathed in Teflon tubing and suspended above the illumination path to prevent direct photochemical responses. However, light that was scattered by the glass Luggin–Haber capillaries and through the bottom opening of the tubing were sufficient to induce a noticeable change in E_{oc} values upon illumination (**Figure 3.5b**). Therefore, the Teflon tubing was wrapped in opaque black polyolefin heat-shrink tubing and the bottom of the Teflon tubing was sealed with silicone (**Figure 3.5c**). Slits were made on the side of the tubing at the bottom/top to allow

solution/air to enter/exit the sheath and using this setup, we did not observe any noticeable changes in E_{oc} values upon illumination of unmodified Nafion under conditions of pHCl 2||3 (**Figure 3.5b**).

A critical constraint imposed by use of immersed Ag/AgCl wires as potential-sensing electrodes is exclusive use of chloride-containing electrolytes and reported electrode potential differences that are sensitive to not only net electric potentials across the membrane, but also differences in the activity of Cl^-(aq). An advantage to this setup is that the sign of ϕ_D^{mem} is such that $\Delta\bar{\mu}_{Cl} = \Delta\mu_{Cl} + zq\phi \neq 0$, and because the Ag/AgCl wires are sensitive to $\Delta\bar{\mu}_{Cl}$, this results in a non-zero value for the open-circuit potential, E_{oc}. If an anion-exchange membrane had separated the two sides of the electrochemical cell or the Ag/AgCl wires had been replaced with reversible hydrogen electrodes, then the sign of ϕ_D^{mem} would have led to near-zero E_{oc} values and provided little information about the value of ϕ_D^{mem}.[74] These facts are apparent by analyzing E_{oc} as follows,

$$E_{oc} = E_N^{redox} + \sum \phi_i = \left\{E_N^{int,WE} + \left(-E_N^{int,CE}\right)\right\} + \left\{\left(\phi_D^{int,WE}\right) + \left(-\phi_D^{int,CE}\right)\right\} + \phi_{LJ}^{mem} \quad (3.17)$$

where ϕ_i is any contribution to differences in electric potential between nearer to the WE *versus* nearer to the CE, including Donnan potentials, **Equations 3.5 and 3.7**, and liquid-junction potentials. Using **Equations 3.8 and 3.9**, and assuming a position-independent formal reduction potential because both sensing electrodes are the same type, $E_N^{o\prime,int,WE} = E_N^{o\prime,int,CE}$, E_{oc} can be rewritten as follows,

$$E_{oc} = \left\{\frac{RT}{F}\ln\frac{[Cl^-]^{CE}}{[Cl^-]^{WE}}\right\} + \left\{\frac{RT}{F}\ln\frac{[H^+]^{CE}}{[H^+]^{WE}}\right\} + \phi_{LJ}^{mem} \quad (3.18)$$

$$E_{oc} = \frac{2RT}{F}\ln\frac{[HCl]^{CE}}{[HCl]^{WE}} + \phi_{LJ}^{mem} \quad (3.19)$$

$$E_{oc} = 2\phi_D^{mem} + \phi_{LJ}^{mem} \quad (3.20)$$

The final expression results from use of **Equation 3.7**, and the fact that for each solution [HCl] = $[H^+]$ = $[Cl^-]$, and therefore every concentration term can be replaced with [HCl]. **Equation 3.20** indicates that when E_{oc} is measured across a *cation*-exchange membrane using sensing electrodes whose reduction products, e.g. Cl^-(aq), are equal to the concentration of cations in the electrolyte, the net effect is a non-zero E_{oc}. And assuming that ϕ_{LJ}^{mem} is small,[46] the net Donnan membrane potential, ϕ_D^{mem}, can be deconvoluted from measured E_{oc} values in the dark as $\phi_D^{mem} \approx E_{oc}/2$. Moreover, we assume that under illumination, $\Delta E_{oc} = V_{oc} \approx \Delta\phi_D^{mem}$, which implies that only changes in electric potential are detected at the potential-sensing electrodes, and not changes in chemical potential of Ag, AgCl, and/or Cl^-, and thus not E_N^{int} at an electrode|solution interface. We assume this to be true, because generally the activity of Cl^- should not be altered by the photoacid dye sensitization Förster cycle. In addition, steady-state V_{oc} values are observed after only a short ~2 min illumination time and distances that Cl^-(aq) must transport in order to influence E_N^{int} at the Ag/AgCl wires, 2.5 cm from membrane to electrode, are ~500 times larger than the maximum distance that Cl^-(aq) must transport to influence either value of ϕ_D^{int} at a membrane|solution interface, <50 μm across the membrane.

Finally, the substitution from SCEs to Ag/AgCl wire meant measurements of current were now strongly limited by uncompensated resistance between the sensing electrodes and the membrane interface, so much so that Luggin–Haber capillaries could not remedy this limitation (**Figure 3.3**). Therefore, the magnitude of photocurrent values were not representative of the applied potential to HPTSA-modified PFSA. This suggests that detailed analysis of photocurrent values is futile, while also supporting the observation that light and dark current density *versus* potential data are linear, even when ion-exchange-membrane–liquid junctions were designed for effective current rectification and charge separation.

Chapter 3.4: Results and Discussion

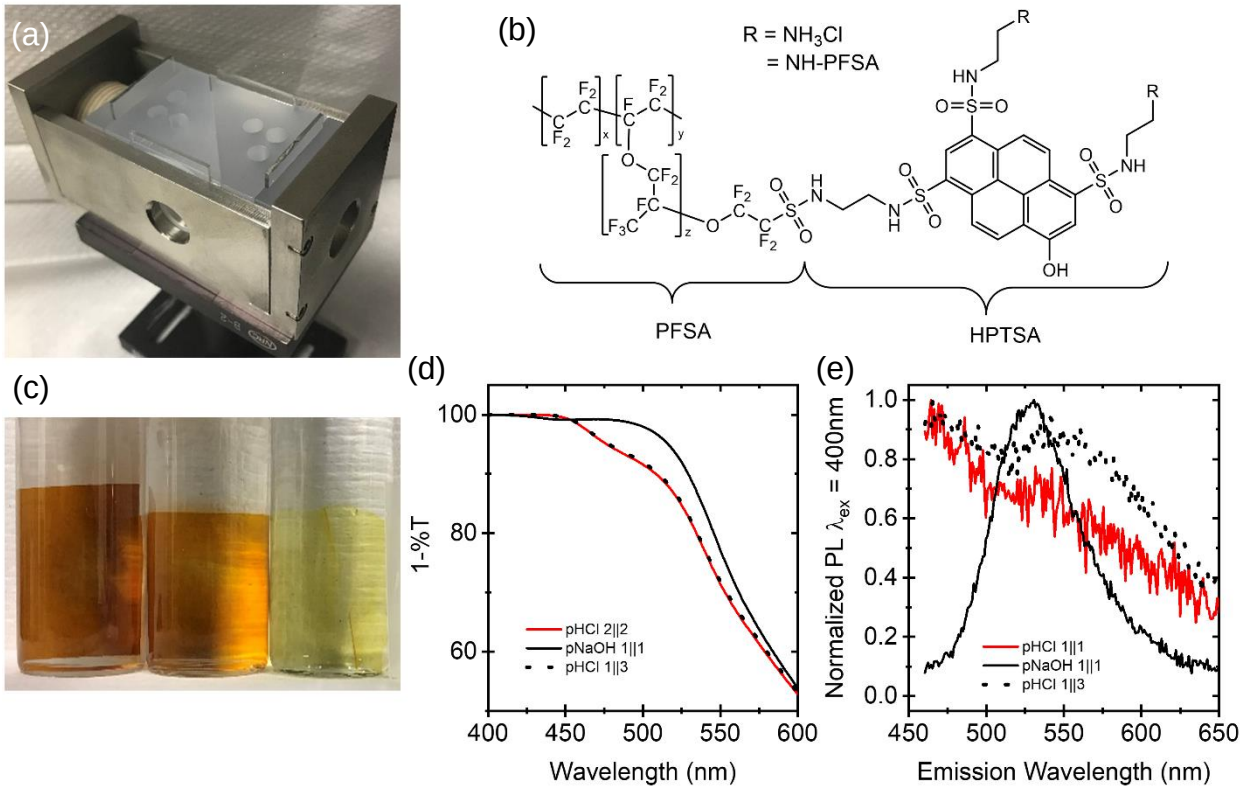

Figure 3.7. (a) Photograph of custom four-window H-cell used to perform absorption and photoluminescence measurements on wetted samples. **(b)** Chemical structure of HPTSA-modified PFSA. More than one ethylenediamine group can covalently bond to PFSA, as indicated by the two options for each of the R groups, which may result in crosslinking of the polymer membrane. **(c)** Photograph of HPTSA-modified PFSA with, from left-to-right, greatest-to-least concentration of dye (**Table 3.2**). **(d)** Transmittance spectra and **(e)** normalized photoluminescence spectra for **DSM-H1** (leftmost membrane in **panel c**) under the aqueous pHCl (pNaOH) conditions indicated, where pHCl (pNaOH) stands for "–log [HCl] ([NaOH])" and [HCl] ([NaOH]) is the concentration of HCl (NaOH), such that pHCl 1||3 means 100 mM HCl(aq)||1 mM HCl(aq), and in which case light was incident on, and photoluminescence was detected from, the side with the dilute electrolyte chamber.

We synthesized three ion-exchange membranes consisting of HPTSA covalently bound to PFSA at various photoacid dye binding densities using a previously reported procedure[20] (**Figure 3.7c,d**, **Table 3.2**): two samples contained a high concentration of photoacid dyes (**DSM-H**) and one sample contained a low concentration of photoacid dyes (**DSM-L**). To obtain electric potential differences that

Table 3.2. HPTSA-modified PFSA membranes with various dye doping densities as indicated by optical densities (OD) at 405 nm.

Membrane	$OD_{405\ nm}$
DSM-H1	>4
DSM-H2	>4
DSM-L	0.664

were stable on the timescale of days with only minor evidence for ion crossover, we substituted SCEs with Ag/AgCl wire, only used acidic electrolytes to wet each side of the membrane and decreased the acid concentration that we used previously from 1 M to between 100 mM HCl(aq) (pHCl = 1) and 0.1 mM HCl(aq) (pHCl = 4). Unless stated otherwise, from this point forward we define pHCl to stand for "–log [HCl]," where [HCl] is the concentration of HCl, and not "–log a_{HCl}," where a_{HCl} is the activity of HCl.

Effects of junction contacts on electric potential differences in the dark and light. It is useful to quantify net electric potential differences across semiconducting devices, because those values are predictive of the ability of the device to rectify current well and exhibit large values for V_{oc}. Validation of variable-magnitude built-in membrane potentials was achieved by wetting HPTSA-modified PFSA on each side by different concentrations of aqueous acidic electrolytes: moderate acid on one side, e.g. pHCl = 1 – 2, and weaker acid on the other side, e.g. pHCl = 3 – 4, with an example projected distribution of ions for pHCl 1||3 across Nafion shown in **Figure 3.8**. Unlike in electronic semiconductor–liquid-junction photoelectrochemical constructs, ion-exchange membranes in

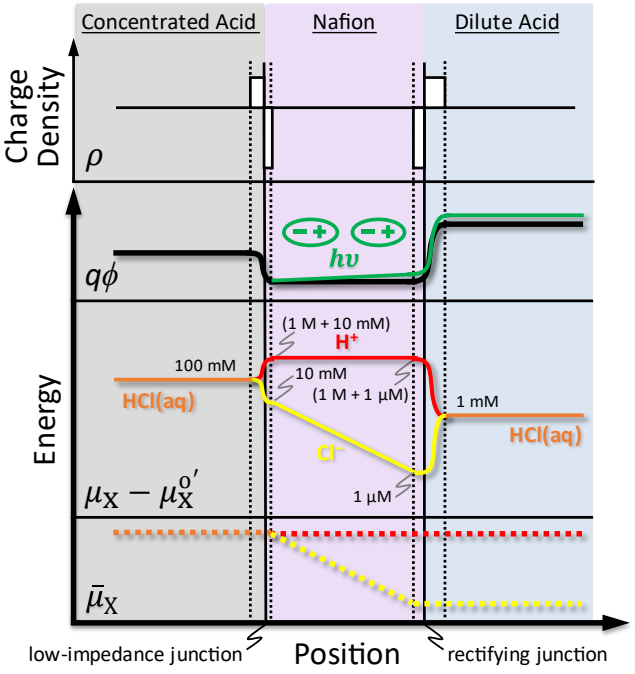

Figure 3.8. Spatial representation, from top to bottom, of near-equilibrium uncompensated charge density; electric potential as an energy; chemical potentials each referenced to its concentration chemical potential (where "concentration" is commonly used for equilibrium constants and is analogous to "formal" for reduction potentials) and including concentrations of mobile charged species, X = H^+ or Cl^-; and electrochemical potentials, each expected for wetted Nafion|solution interfaces. Also shown in green is the proposed outcome of continuous-wave illumination, where dipoles are proposed to form at steady state that results in an increase in the magnitude of the membrane potential from values measured in the dark.

contact with aqueous electrolytes are limited to approximately a 2–3-unit pH difference across the membrane due to limitations described above. As expected, using our new more accurate setup and protocols, HPTSA-modified PFSA exhibited values of E_{oc} that are similar to those predicted by Donnan theory (**Table 3.3**), suggesting that the bulk material is still a cation-exchange membrane even at the largest loading of photoacid molecules used, which are proposed to covalently bind to sulfonate groups and therefore decrease protonic dopant density.[13] Differences between measured E_{oc} values and those predicted by Donnan theory were largest in magnitude, resulting in the largest predicted values for ϕ_{LJ}^{mem}, when the low-impedance junction was in contact with the chamber that contained a large concentration of aqueous electrolyte, i.e. 100 mM HCl(aq) (pHCl = 1), and/or when the rectifying junction was in contact with the chamber that contained the smallest concentration of aqueous electrolyte, i.e. 0.1 mM HCl(aq) (pHCl = 4). Despite the existence of Donnan exclusion of Cl^- coions, the cause of these large values for ϕ_{LJ}^{mem} are likely due to the presence of a relatively large concentration of Cl^- coions immediately inside the membrane in contact with the concentrated electrolyte that results in substantial rates of HCl crossover and/or significant changes in local HCl concentration in the dilute electrolyte near the membrane, respectively.

Table 3.3. Open-circuit potential (E_{oc}, in mV) and open-circuit photovoltage (V_{oc}, in mV), under 405 nm illumination at 1.4 Suns equivalent excitation (45 mW/cm^2 of 405 nm laser light) measured across **DSM-H1** for different combinations of HCl(aq) concentrations in contact with the membrane to form the low-impedance junction (first value; larger concentration; at working electrode (WE)) and the rectifying junction (second value; smaller concentration; at counter electrode (CE)), calculated values (in mV), and differences (in mV) attributed to ϕ_{LJ}^{mem}.

pHCl condition	$\boldsymbol{E_{oc}}$ *(measured)*	$\boldsymbol{\phi_D^{mem}}$ *(calculated using **Equation 2**, with T = 25 °C, approximately ambient)*	$\boldsymbol{\phi_{LJ}^{mem}}$ *(calculated using **Equation 9**)*	$\boldsymbol{V_{oc}}$ *(measured)*
2||3	-113.7 ± 0.3	-59.2	+4.7 ± 0.3	-0.19 ± 0.02
2||4	-229.1 ± 0.3	-118.4	+7.7 ± 0.3	-0.78 ± 0.01
1||2	-109.3 ± 1.4	-59.2	+9.1 ± 1.4	-0.58 ± 0.07
1||3	-219.1 ± 0.6	-118.4	+17.7 ± 0.6	-2.2 ± 0.2

Using our new more accurate setup and protocols, we now observed that illumination results in an *increase* in the magnitude of E_{oc}, and thus an increase in the net electric potential difference between nearer to the WE *versus* nearer to the CE. This results in the *sign* of V_{oc} values (**Table 3.3**) being opposite ("reverse") of those expected if the same electrostatic distributions had existed in solid-state electronic semiconductor pn-junction or Schottky junction solar cells and opposite of our previous observations using significantly larger concentrations of aqueous acidic electrolyte.[20,22] Nevertheless, "reverse" photovoltaic action has been reported previously in the literature for electronic solar cells[75–80] and for bipolar-membrane-based light-driven proton pumps,[81] often proposed to occur due to dynamic processes that are common in soft polymer materials like ion-exchange membranes. Irrespective, the *magnitude*, on the order of 1 mV, and *timescales*, on the order of 1 min, of growth and decay for our observed quasi-steady-state "reverse" V_{oc} values are each rather similar to those we reported previously,[20,22] and again were *independent on the direction of illumination* (**Figure 3.15**), suggestive of a bulk photovoltaic mechanism.

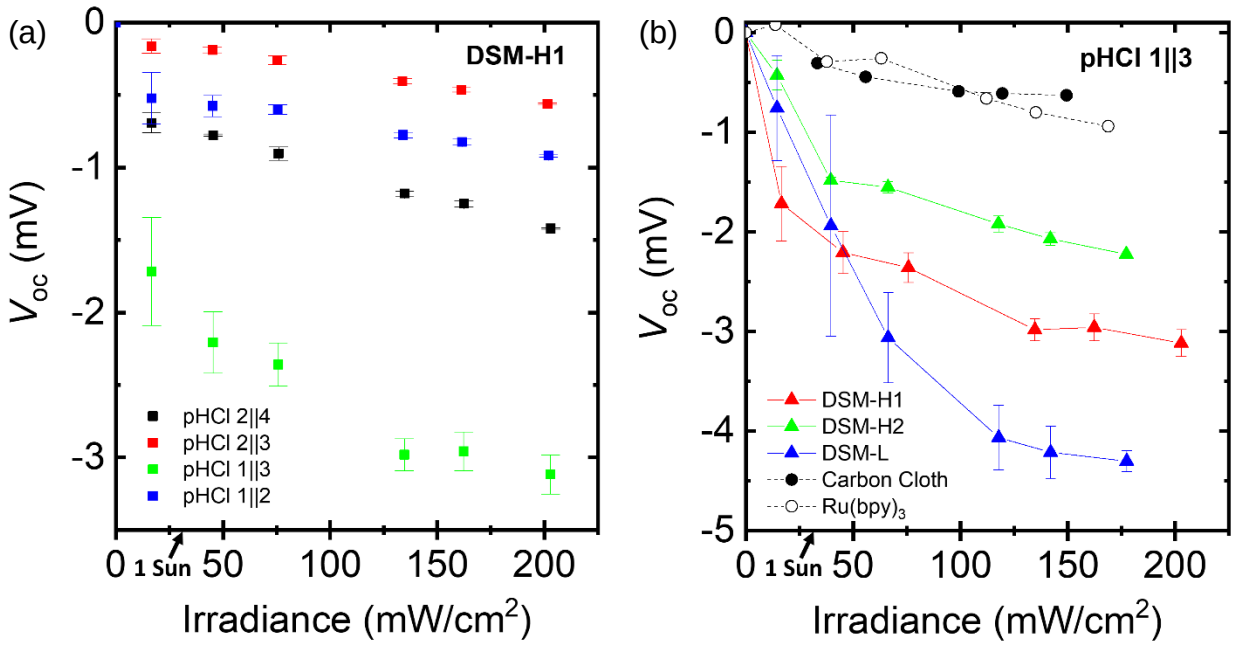

Figure 3.9. (a) Open-circuit photovoltage (V_{oc}) as a function of irradiance from 405 nm laser light measured across **DSM-H1** for different combinations of HCl(aq) concentrations in contact with the membrane to form the low-impedance junction (first value; larger concentration; at working electrode) and the rectifying junction (second value; smaller concentration; at counter electrode). We define pHCl to stand for "–log [HCl]", where [HCl] is the concentration of HCl, such that pHCl 2||4 means 10 mM HCl(aq)||0.1 mM HCl(aq). **(b)** V_{oc} as a function of irradiance measured across Nafion membranes containing various photoabsorbers under conditions of 100 mM HCl(aq)|| 1 mM HCl(aq) (pHCl 1||3). HPTSA ("**DSM**" datasets) was covalent bound to PFSA, $[Ru^{II}(bpy)_3]^{2+}$ was ionically associated into commercial Nafion NR-212, and carbon cloth was affixed to one side of commercial Nafion. Optical densities at 405 nm were >4, except for **DSM-L**, which was 0.664. Data and error bars for each **DSM-X** are the mean ± standard deviation of three trials while each negative control measurement was only performed once. The condition of 1 Sun equivalent excitation occurs for an irradiance of 31.3 mW/cm^2.

Solar cells based on electronic semiconductors exhibit larger values for V_{oc} when they have a low-impedance charge-collection junction, with a small magnitude built-in electric potential difference, and a highly rectifying charge-separation junction, with a large magnitude built-in electric potential difference. To determine whether these same design rules exist for HPTSA-modified PFSA, E_{oc} values and V_{oc} values were examined for various combinations of electrolyte concentrations in the concentrated and dilute electrolyte chambers (**Table 3.3**) and as a function of irradiance (**Figure 3.9**). V_{oc} values correlate somewhat well to E_{oc} values, which are dominated by Donnan-potential-induced membrane–liquid junctions, but correlate even better with minority contributions to E_{oc} presumably due to liquid-junction potentials, ϕ_{LJ}^{mem}, therefore suggesting that

crossover of HCl may be a related to the observed photovoltaic behavior. Comparing conditions when the electrolyte concentration used to form the low-impedance junction is the same (**Figure 3.10a**, black *versus* red, and green *versus* blue), V_{oc} values are largest when an electrolyte with a *larger* value for pHCl is in contact with the rectifying junction, leading to a larger magnitude net built-in electric potential difference. When the electrolyte concentration used to form the rectifying junction of the same (red *versus* green), V_{oc} values are largest when an electrolyte with a *smaller* pHCl is in contact with the low-impedance junction, leading to a smaller impedance for charge collection. This suggests that the overarching design principle for efficient charge separation and charge collection in our protonic membrane–liquid-junction assemblies is to use electrolytes with a large difference in pHCl, and thus protonic chemical potential, across the membrane and large values for $\phi_{\mathrm{LJ}}^{\mathrm{mem}}$. The former condition is analogous to the design principle in electronic semiconductor–liquid-junction photoelectrochemical constructs where a large difference in reduction potential, and thus electronic chemical potential, is desired. However, for our protonic membrane–liquid-junction assemblies, the magnitude of the net electric potential difference increases upon illumination resulting in "reverse" photovoltaic action, not decreases as would be expected for traditional electronic semiconductor–liquid-junction designs. Moreover, the fact that **DSM-L**, which contained an order-of-magnitude less photoacids, exhibited a slightly larger value for its maximum V_{oc} than **DSM-H1** and **DSM-H2** (**Figure 3.9b**) suggests that photochemical performance benefits from polymer morphologies present when photoacid concentrations are smaller[55] and/or when photoexcitation is more homogenous.

Effects of dye photochemistry and photophysics on electric potential differences in the light. As desired, illumination of HPTSA-modified PFSA results in photoacids undergoing the dye sensitization Förster cycle, which is supported by the presence of small photoluminescence features that resemble those from deprotonated HPTSA (**Figure 3.7e**). In addition, because >75% of excited-state photoacids recombine non-radiatively independent of their protonation state,[34] absorption of incident illumination necessarily results in significant local heating, which may influence rates of species transport and reactivity. Because **DSM-H1** and **DSM-H2** each has an optical density at 405 nm of >4 OD, illumination predominantly heats the side of the membrane that the light was incident on and results in a predictable temperature gradient and expected sign of V_{oc} due to the Seebeck effect. However, we observed that the *sign* of V_{oc} did not depend on the direction of illumination (**Figure 3.15**), suggesting that the Seebeck effect was not the main contributor to the observed photoresponse. Notwithstanding, as negative controls two photo-absorbing membranes were evaluated under the optimal pHCl condition of 1||3 to discern the non-photoacidic contribution to the observed photovoltage (**Figure 3.9b**): $[Ru^{II}(bpy)_3]^{2+}$, where bpy is 4,4'-bipyridine, ionically associated into Nafion NR-212 ($[Ru^{II}(bpy)_3]^{2+}$/Nafion) and carbon cloth affixed to Nafion NR-212, each with an optical density at 405 nm of >4. Under these conditions, a significant difference between photoacidic and non-photoacidic membranes was apparent (**Figure 3.10**), suggesting that at least a portion of the photovoltage from HPTSA-modified PFSA is from photoacidic generation of mobile charged species. Moreover, $[Ru^{II}(bpy)_3]^{2+}$/Nafion produced inconsistent values for V_{oc} over time in comparison to **DSM-H1** (**Figure 3.11**), further supporting the importance of photoacidic behavior in order to observe relatively large values for V_{oc} and suggesting that $[Ru^{II}(bpy)_3]^{2+}$/Nafion is not an ideal negative control for a molecular non-photoacidic photoabsorber. In fact, it has been previously reported that ligands from $[Ru^{II}(bpy)_3]^{2+}$

exchange with solvent molecules under visible-light excitation, with the dissociation rate accelerated in highly acidic environments,[82] calling its stability into question.

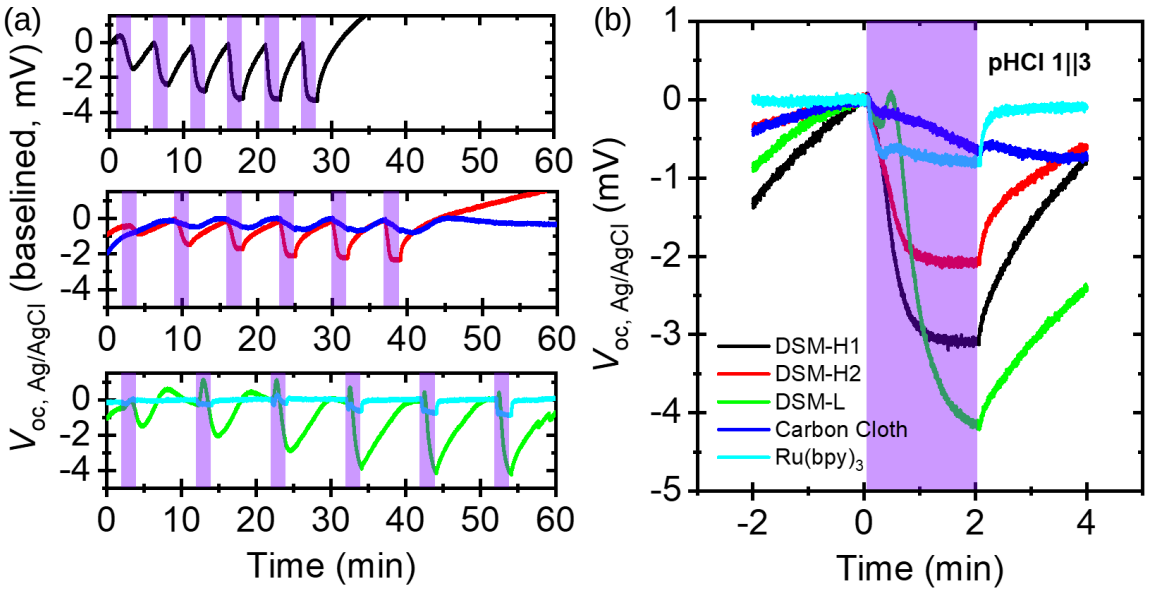

Figure 3.10. (a) Open-circuit photovoltage (V_{oc}) over time measured between two Ag/AgCl wires positioned across various light-absorbing PFSA or Nafion membranes under conditions of 100 mM || 1 mM HCl(aq) (pHCl 1||3) and with data grouped based on illumination cycle timing. Each measurement was baseline corrected for drift of the open-circuit potential by subtracting a line that spanned from the beginning of the first illumination event to the beginning of the sixth illumination event. Purple bars indicate times of 405 nm laser excitation (2 min each) with increasing intensity over time due to decreasing attenuation from a neutral density filter (1 ND, 0.6 ND, 0.4 ND, 0.2 ND, 0.1 ND, no filter). **(b)** Final illumination events in the absence of a neutral density filter, each at a similar irradiance of 140 mW/cm^2, where the condition of 1 Sun equivalent excitation occurs for an irradiance of 31.3 mW/cm^2.

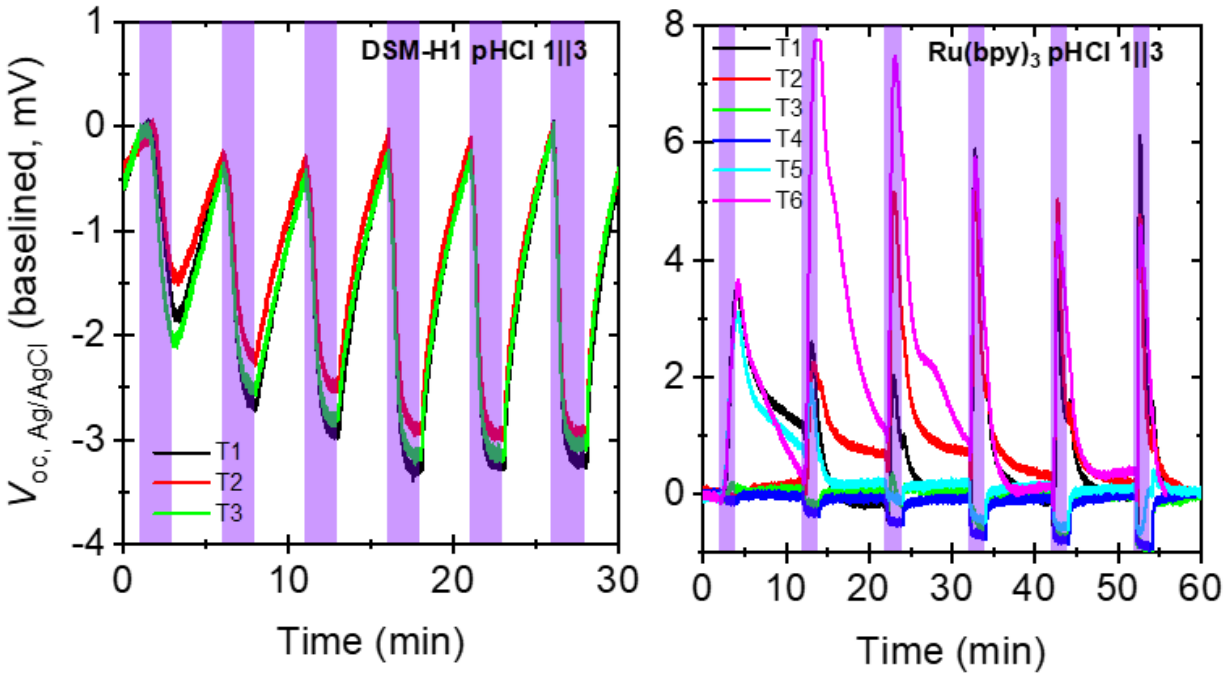

Figure 3.11. Open-circuit photovoltage (V_{oc}) over time measured between two Ag/AgCl wires positioned across **(a) DSM-H1** and **(b)** Nafion NR-212 with ionically associated $[Ru^{II}(bpy)_3]^{2+}$ under conditions of 100 mM||1 mM HCl(aq) (pHCl 1||3). Each measurement was baseline corrected for drift of the open-circuit potential by subtracting a line that spanned from the beginning of the first illumination event to the beginning of the sixth illumination event. Purple bars indicate times of 405 nm laser excitation (2 min each) with increasing intensity over time due to decreasing attenuation from a neutral density filter (1 ND, 0.6 ND, 0.4 ND, 0.2 ND, 0.1 ND, no filter). The maximum irradiance used for **DSM-H1** was 166 mW/cm^2 and for $[Ru(bpy)_3]^{2+}$/Nafion was 141 mW/cm^2, and the condition of 1 Sun equivalent excitation for **DSM-H1** occurs for an irradiance of 31.3 mW/cm^2. The legend indicates the chronological order of trials (T) taken on the same membrane, each with refreshed electrolyte.

Identification of mobile charge carriers using transient absorption spectroscopy. Transient absorption spectroscopy data from **chapter 1.2** suggest that reprotonation of ground-state HPTSA with H^+(aq) (**Reaction 1.2**) is significantly faster than reprotonation of ground-state HPTSA with H_2O(l) to form OH^-(aq) (**Reaction 1.1**), and thus **Reaction 1.1** contributes little-to-nothing toward dye regeneration, especially at the pH $\leq$ 4 conditions used for the photoelectrochemical measurements. Because HPTSA*(aq) is known to only release H^+(aq),[26] this suggests that the only species transiently photogenerated during the dye sensitization Förster cycle that can be collected to perform useful work are H^+, concomitant with formation of polymer-bound deprotonated

HPTSA. This implies that upon completion of the dye sensitization Förster cycle zero net chemistry has occurred, meaning that our prior cartoons of processes possible from HPTSA, and related analogs, do not likely depict the dominant reactions in practice.[20,21] This conclusion is of critical importance because the V_{oc} of solar-energy-conversion devices benefits most from light-driven changes in the concentration of minority-carrier species, where small changes in their concentration result in large changes in their chemical potential, which are directly related to the amount of useful work they are able to perform. Since HPTSA is only a photoacid at pH values near or smaller than its measured pK_a value of 4.9, and at these pH values HPTSA*(aq) only releases H^+(aq) and ground-state deprotonated HPTSA(aq) only reacts with H^+(aq), little-to-no minority-carrier OH^-(aq) are photogenerated. In the absence of photogenerated minority-carrier species, V_{oc} values are expected to be small, as we observed herein and previously.[20,22] Moreover, results from these photochemical analyses suggest that HPTSA and its analogs are not optimal for use in photovoltaic light-to-ionic energy conversion processes that mimic traditional electronic semiconductor designs. Detailed numerical studies of the design guidelines for photoacids and photobases that photogenerate both H^+(aq) and OH^-(aq) to allow for large V_{oc} values indicate that more extreme pK_a and pK_a* values are needed. Reported syntheses and characterizations of such molecules seem to be devoid from the peer-reviewed literature and so we are working to develop new photoacid and photobase motifs that will be far more effective at exhibiting protonic photovoltaic action.

Proposed mechanism for light-to-ionic power conversion. Nafion membranes wetted by aqueous acidic electrolytes have H^+ as counterions to their ~1 M sulfonate groups,[69] meaning that pH ≈ 0 in their bulk quasi-neutral regions.[70] This is relevant because under these nearly super-acidic electrolyte conditions, excited-state proton transfer from photoacids to solution can be kinetically

inhibited,[23] thus attenuating photogeneration of mobile H^+, as supported by the data in **Figure 3.7e**. Therefore, photoacids most likely to perform excited-state proton transfer are probably located at the membrane|solution interfaces where a gradient in pH exists across the space–charge region, and which is also the optimal location for efficient charge separation of photogenerated mobile charged species in traditional electronic semiconductor solar cells. This, coupled with the observation of an illumination-direction-independent *sign* and *magnitude* of V_{oc}, suggests that photogenerated majority-carrier H^+ are collected over the thickness of HPTSA-modified PFSA (50.8 μm) and/or that photo-induced local polarizations generate differences in electric potential that are sensed at the Ag/AgCl wires and are independent on the direction of illumination.

The hypothesis of a tens-of-microns collection length seems unlikely based on the reasonable upper limit for the diffusion coefficient of H^+ in Nafion (9.31×10^{-5} cm^2/s in bulk water)[46] and an effective time constant for the photoacid dye sensitization Förster cycle, which is gated by the ~5 ns excited-state lifetime of the photoacid in strongly acidic conditions like those in Nafion, because this suggests a diffusion length of ~7 nm. This diffusion length is the average transport distance for a photogenerated H^+ prior to recombination with a deprotonated photoacid; although, the diffusion length prior to recombination with OH^-(aq) is considerably larger. Under our experimental conditions on average there are only 10^{-14} M OH^-, which is the same as 30,592 OH^- molecules per cm^2 of 50.8 μm thick membrane. Presuming that photogenerated H^+ sample positions within a hemisphere of 50.8 μm radius during transport across the 50.8 μm thick membrane, the average number of OH^- encounters experienced by each photogenerated H^+ before reaching the other membrane|solution interface is 1 – 2. Such a majority-carrier device could conceivably collect charges stochastically over such large distances,[83] but only in the absence of deprotonated photoacids, because they limit this transport distance to ~7 nm.

Given that deprotonated photoacids will be present under illumination, we hypothesize that photo-induced local polarizations are responsible for the observation of "reverse" photovoltaic action by a process that we term electrolyte-crossover-induced bulk membrane polarization (ECIBMP). For ECIBMP, we propose that photogenerated-H^+/deprotonated-HPTSA pairs, and not mobile charged species pairs that are commonly generated in traditional electronic solar cells, form collectively *asymmetric* space–charge regions in the *bulk* of HPTSA-modified PFSA (Figure 3, in green). In order to observe a non-zero value for V_{oc} a net asymmetry is required. The observation of "reverse" photovoltaic action is consistent with the driving force for charge separation being liquid-junction potentials that form due to diffusion of HCl toward the rectifying junction in the dark. This hypothesis is also consistent with the fact that the magnitude of measured V_{oc} values are directly related to presumed magnitudes of ϕ_{LJ}^{mem} values (**Table 3.3**). Moreover, such a bulk phenomenon would result in an illumination-direction-independent *sign* and *magnitude* of V_{oc}, as we observed.

Mechanistically, we envision that during the lifetime of photogenerated H^+, H^+ diffuse away from ground-state deprotonated HPTSA and toward the rectifying junction. However, photogenerated H^+ also experience Coulombic attraction to anionic ground-state deprotonated HPTSA via processes that are similar to those that occur in formation of liquid-junction potentials in a solution and Dember potentials due to ambipolar diffusion in electronic semiconductors.[84] Therefore, H^+ resides on average at a distance equal to the Debye/Bjerrum length for the two ions (**Figure 3.15**), which is on the order of 1 nm per HPTSA at the approximate concentration of HPTSA present in **DSM-H**. (The concentration of HPTSA was approximated to be 77 mM using

the Beer–Lambert law and the decadic absorption coefficient of HPTSA(aq) at 405 nm, a pathlength equal to the thickness of Nafion NR-212 (50.8 μm), and the optical density of **DSM-H** at 405 nm, which was approximated to be ten times larger than that measured for **DSM-L** (0.664) because the synthetic protocol used a ten times more dilute dye solution.) This dipolar state generated by a single charge pair exhibits a small electric field in comparison to projected electric field strengths at space–charge regions near the membrane|solution interface, which are up to ~240 mV and drop over several nanometers. Excitonic electrostatically bound charges will separate at these space–charge regions to generate mobile charged species and will result in typical photovoltaic action, but the number of species photogenerated near those interfacial regions (over <10 nm) is likely so small compared to those generated in the membrane bulk (over 50.8 μm) that any effects from excitonic charge-separation events are likely undetectable given the sensitivity of our measurement capabilities. Regeneration of ground-state deprotonated HPTSA by a nearby H^+ results in formation of no net chemical species, however we suspect that spatial distributions of H^+ under illumination differ from those in the dark, where most H^+ are electrostatically attracted to sulfonate groups covalently anchored to the polymer, or less commonly, mobile Cl^-. In either case, on average electric potential differences formed by ECIBMP will increase the magnitude of ϕ_{LJ}^{mem} values present in the dark due to similar ion-crossover phenomena.

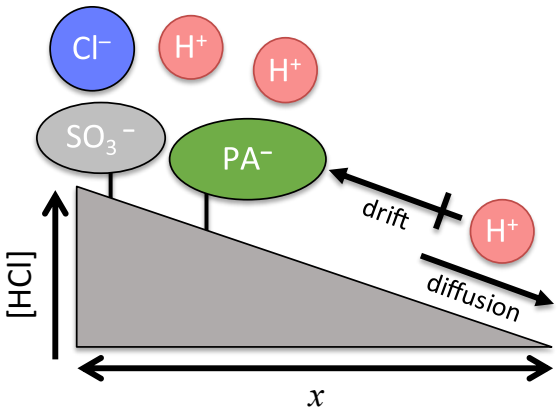

Figure 3.12. Scheme depicting the proposed mechanism for "reverse" photovoltaic action, ECIBMP, in ionic membrane–liquid assemblies. A gradient in HCl across the membrane drives dipole formation between photogenerated H^+ and various counterion species.

While reported V_{oc} values are likely indicative of the properties of HPTSA-modified PFSA, as mentioned above, photocurrent values are not, due to the low ionic strength and large transport

distances of ions in the aqueous electrolytes between the membrane and each Ag/AgCl wire in comparison to solely across the membrane. However, an upper limit to the local current density across only HPTSA-modified PFSA can be approximated by assuming a unity quantum yield for conversion of absorbed photons to ionic current and assuming a membrane conductivity of ~50 mS/cm, which is the approximate value reported for commercial Nafion at room temperature when fully hydrated and protonated using H_2SO_4(aq).[85,86] A relation between observed V_{oc} values and ideal short-circuit photocurrent values can be obtained using Ohm's law,

$$E = iR = j\text{ASR} = j/\text{ASC} = j\ell/\sigma \tag{3.21}$$

where i is the current (A), R is the resistance (Ω), j is the current density (A/cm^2), ASR is the area-specific resistance (Ω-cm^2), ASC is the area-specific conductance (S/cm^2), ℓ is the thickness of the membrane (cm), and σ is the conductivity of the membrane (S/cm). Solving this formula for the current density as a function of the potential and adding a constant ideal photocurrent in the absence of other losses, $j_{ph,ideal}$, one obtains the following,

$$j = \sigma E/\ell - j_{ph\text{-}sc,ideal} \tag{3.22}$$

Under open-circuit conditions, $j = 0$ and thus $j_{ph,ideal} = \sigma V_{oc}/\ell$. Using the maximum measured $V_{oc} \approx$ 4 mV, which seems to saturate at high light intensities and requires an irradiance of > ~100 mW/cm^2, one calculates that $j_{ph,ideal} \approx$ (5 x 10^{-2} S/cm) (4 x 10^{-3} V) / (5 x 10^{-3} cm) = 40 mA/cm^2. It is remarkable that this value is within error of the value predicted by assuming that every incident photon is converted into current as a mobile H^+. Further refinement of this analysis would lead to a smaller value for $j_{ph,ideal}$, because the conductivity used for this calculation is likely overestimated given that it was measured in the absence of interfacial space–charge regions. But this effect is offset by the fact that every absorbed photon does not generate a mobile H^+, as evidenced by

photoluminescence data (**Figure 3.7e and 3.13**), which suggest that ~10% of photoacids in **DSM-H1** undergo the Förster cycle. Collectively, however, this simple Ohm's law analysis does suggest that it is reasonable to assume that photogenerated H^+ are capable of generating a photocurrent. Using this above information one can approximate the average concentration of photogenerated H^+, by dividing $j_{ph,ideal}$ by the membrane thickness (5.08 x 10^{-3} cm) and the Faraday constant, and multiplying it by the time it takes to regenerate the deprotonated photoacid, which in aqueous 1 M acidic solutions is limited by the excited-state lifetime to ~5 ns. This results in a projected steady-state increase in the concentration of H^+ of ~4 x 10^{-10} M, which is intermediate in concentration between that of Cl^- coions and OH^- in the dark.

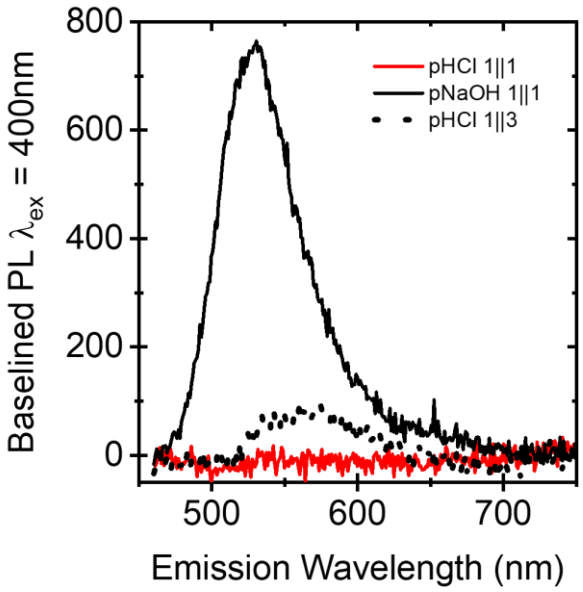

Figure 3.13. Photoluminescence spectra for **DSM-H1** under the indicated aqueous pHCl (pNaOH) conditions, and with light incident on the less-acidic electrolyte, where photoluminescence was also detected. A baseline correction was applied by subtracting a line that spanned data from 460 nm to 750 nm in order to highlight spectral features that are consistent with emission from deprotonated HPTSA (530 nm for pNaOH 1||1 and 570 nm for pHCl 1||3).

Outlook for use of photoacid-modified ion-exchange membranes for light-driven desalination. Minimum voltages required to drive desalination are not very large, thermodynamically requiring at most ~50 – 200 mV depending on the salinity of the water source, e.g. seawater or brackish, and desired output salinity, e.g. potable or for agriculture, and before considering overpotential losses. With further increase in performance, illumination of HPTSA-modified PFSA could be used to *indirectly* drive desalination of salt water via intermediate electricity. However, a benefit of using an ion-exchange membrane is that it could be contacted directly by aqueous salt solutions on each

side to *directly* drive desalination. This requires that Donnan space–charge regions are generated from equilibration of majority-carrier salt cations, such as Na^+ or K^+, with minority-carrier excluded salt anions, such as Cl^-. In this configuration, however, photovoltages must be of the traditional sign so that photogenerated cationic charged species transport toward and across the low-impedance charge-collection junction, which is the side of the membrane that contacts the solution containing the larger salt concentration.

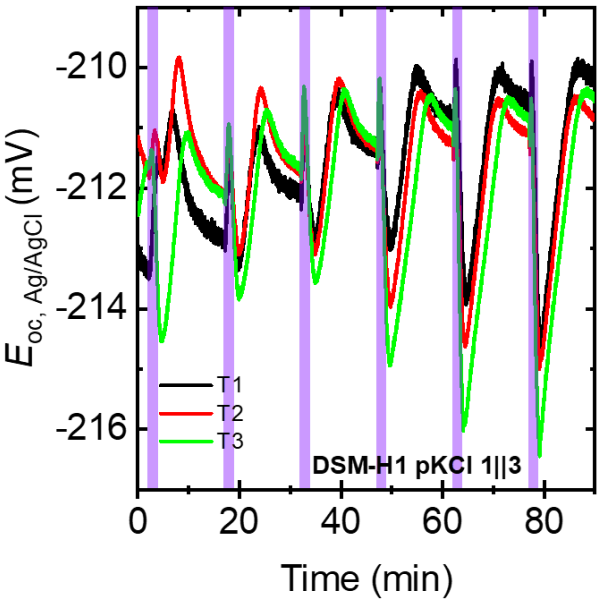

Figure 3.14. Open-circuit potential (E_{oc}) over time measured between two Ag/AgCl wires positioned across **DSM-H1** under conditions of 100 mM||1 mM KCl(aq) (pKCl 1||3). The legend indicates the chronological order of trials (T) taken on the same membrane. Purple bars indicate times of 405 nm laser excitation (2 min each) with increasing intensity over time due to decreasing attenuation from a neutral density filter (1 ND, 0.6 ND, 0.4 ND, 0.2 ND, 0.1 ND, no filter). The maximum irradiance used was 120 mW/cm^2 and the condition of 1 Sun equivalent excitation occurs for an irradiance of 31.3 mW/cm^2.

Detailed studies of HPTSA-modified PFSA function when in the presence of pH-neutral aqueous salt solutions were not performed due to the complexity of having multiple ions present (i.e. H^+ and salt ions), use of photoacids that only photogenerate mobile protons, and small magnitude V_{oc} values observed in the presence of acid only. Notwithstanding, as an initial proof-of-concept we evaluated **DSM-H1** in the dark and under illumination while in the presence of significant amounts of aprotic salts, i.e. KCl, under near-neutral pH conditions (**Figure 3.14**). Inconsistent behavior was observed at early times, which also used the lowest intensity light of those examined, that may be a consequence of initial equilibration of the salt solution with photogenerated H^+ from the photoacids, even though the membrane had been soaked

in 100 mM KCl(aq) for 24 h prior to measurements. Regardless, data obtained from **DSM-H1** using pKCl 1||3 suggest that in this configuration "reverse" photovoltaic action is still observed (**Figure 3.14**).

Further requirements to enable dye-sensitized membrane–liquid-junction constructs to *directly* drive desalination likely include that photoacid and/or photobase dye sensitizers be replaced with photo-ionophores, which change binding strength to a cation or anion upon photoexcitation. Such molecules have been reported previously,[87] but have not been optimized for this application. Moreover, a single homogeneous ion-exchange membrane directly wetted by salt solutions on each side will not be able to drive the desired ion-pumping chemistry. This is because in the absence of a low-impedance junction between the ion-exchange membrane and the concentrated electrolyte, e.g. like a so-called tunnel junction, net chemical reactions cannot be driven by light that require more free energy than the reactions used to set the built-in potentials of the rectifying charge-separation junction and low-impedance charge-collection junction. This does not limit photovoltaic devices, where light does not generate any net chemical species and therefore the entire photovoltage can be used to perform useful work. However, in devices that drive net chemistry, such as solar fuels constructs, chemical reactions of interest, such as H_2 evolution and O_2 evolution, cannot be used to dictate the built-in potential of both the rectifying and low-impedance junction on each side of a homogeneously-doped electronic semiconductor, because photovoltages due to solar irradiation of terrestrial constructs will not exceed the free energy difference of these reactions, e.g. 1.23 V. This challenge existed in our previous buried-junction bipolar-membrane designs,[21,22] where contacting phases consisted of aqueous acid and aqueous base, which determined built-in potentials but limited photovoltages to values that were incapable of driving net generation of acid, as H^+(aq) and a solvated counterion, and base, as OH^-

(aq) and a solvated counterion.[3] Therefore, analogous to design principles in semiconductor–liquid junctions, low-impedance junctions are typically formed using an intervening contact that decouples the selectivity of transport from the thermodynamics of the contacting phase. In this regard, a highly doped membrane could be used to form a solid-state low-impedance junction to a dye-sensitized membrane–liquid-junction construct prior to contacting the concentrated electrolyte chamber.[88]

Dye-sensitized membrane–liquid-junction constructs will also suffer from challenges that are common for ion-exchange membranes in desalination technologies, such as biofouling, scaling, instability, etc.[89,90] However, if these obstacles can be overcome, dye-sensitized membrane–liquid-junction constructs afford a flexible platform for desalination that can be used as an alternative to existing technologies (reverse osmosis, solar-thermal desalination, electrodialysis, etc.) by enabling a small-footprint autonomous desalination device.[91] The proposed technology would be most beneficial for use in remote desalination of brackish water, where reverse osmosis is not cost competitive,[88] and transporting water is too expensive.[92] For example, salinity requirements for agriculture are often less strict compared to requirements for potable water, offering an avenue for feed water partially contaminated with saline to be passively desalinated for use in irrigation, and reused via collection of runoff. Collectively, our work provides guidance for the community to help advance these device designs with hopes of ultimately realizing a small-footprint autonomous device for distributed clean water generation.

Chapter 3.5: Conclusions

Traditional perfluorosulfonic acid ion-exchange membranes were covalently modified with custom photoacid dye molecules and wetted by an aqueous acidic electrolyte on each side. Using a custom electrochemical cell and Ag/AgCl wires as potential-sensing electrodes, membrane potentials were accurately quantified in the dark and under 0.5 – 6.5 Suns equivalent excitation. In the dark, measured net electric potential differences were similar to those expected from Donnan theory, while in the light, open-circuit photovoltages were largest in magnitude when the difference in interfacial Donnan electric potentials between the rectifying charge-separation junction and the low-impedance charge-collection junction were largest. Maximum open-circuit photovoltages of ~4 mV were measured albeit their sign was opposite ("reverse") of that expected based on the sign of net electric potential differences across the membrane. Dye sensitizers consisting of photoacids that could perform excited-state proton transfer were more effective at exhibiting photovoltaic action than negative control dyes that could not. However, mechanistic details gleaned from nanosecond transient absorption spectroscopy suggest that even state-of-the-art photoacids only photogenerate mobile protons, which in part limits performance because protons are majority-carrier mobile charged species. We hypothesize that the observation of "reverse" photovoltaic action is due to electrolyte-crossover-assisted charge separation that results in bulk membrane polarization, which are the liquid-junction analogs of Dember potentials in electronic semiconductors. Our results further the basic understanding of means by which light can be used exhibit photovoltaic action through transport and reactivity of ions. These results also guide next research steps, which include the development of photoacids and/or photobases that exhibit a larger change in acidity upon photoexcitation, such that both majority-carrier and minority-carrier species are photogenerated. Moreover, to realize light-driven ion pumps for

application in direct desalination of salt water, critical needs include the development of photo-ionophores, to directly photogenerate non-protonic ions, and highly doped membranes, to form low-impedance junctions between low-doped ion-exchange membranes and concentrated electrolytes.

Chapter 3.6: Additional Experiments

Independence of Illumination Direction on Open-Circuit Photovoltage. Using a custom automated setup we measured the effect of equal illumination intensity and beam profile incident from either direction of the cell in an alternating fashion (**Figure 3.15**), using only one motorized flipper mirror (Thorlabs, MFF101). Results were the same as we reported previously in that there was no illumination-direction dependence to the observed sign or magnitude of V_{oc} values.

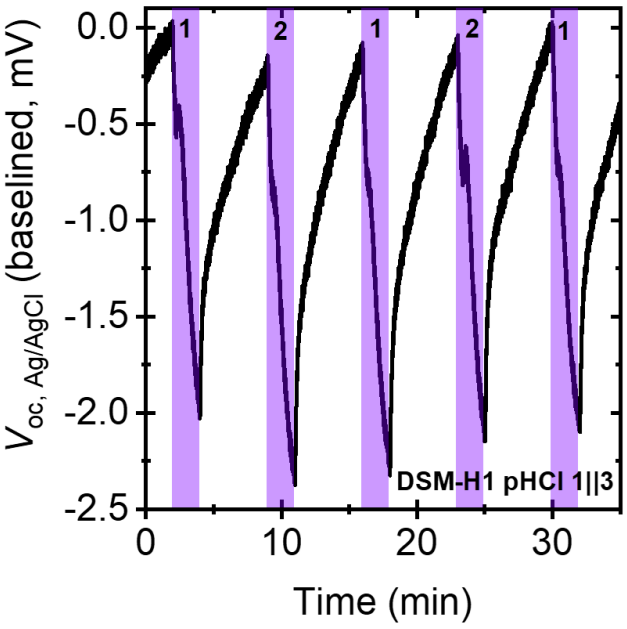

Figure 3.15. Open-circuit photovoltage (V_{oc}) measured for **DSM-H1** under conditions of 100 mM HCl||1 mM HCl (pHCl 1||3) in the dark and illuminated with 170 mW/cm^2 of 405 nm laser light demonstrating the independence of illumination direction (incident on the side with the dilute electrolyte (*Event 1*) or incident on the side with the concentrated electrolyte (*Event 2*)) on the sign and magnitude of the open-circuit photovoltage (V_{oc}) while illuminated (purple bars). Each measurement was baseline corrected for drift of the open-circuit potential by subtracting a line that spanned from the beginning of the first illumination event to the beginning of the fifth illumination event.

Photoresponse Contribution due to Photoinduced Redox Reactions. Prior literature has reported that intense ultraviolet illumination of HPTS, a precursor of HPTSA, results in its photooxidation.[40] Therefore, to evaluate whether a similar process could also be responsible for some of the observed V_{oc} values from HPTSA-modified PFSA, 1 mM $Fe(ClO_4)_x(aq)$, where x is the oxidation state of iron, was introduced into both electrolytes of the pHCl 1||3 condition to attenuate photooxidation of HPTSA or provide a scavenger for solvated radicals. The addition of iron salts did not result in a significant change to V_{oc} values (**Figure 3.19**). Moreover, a methoxylated version of HPTSA, MeOPTSA, was synthesized and characterized (**Figures 1.4 and 1.5**), and when covalently bonded to PFSA and evaluated under conditions of pHCl 2||3 was shown to exhibit V_{oc} values that were significantly smaller in magnitude and opposite in sign to those observed from HPTSA-modified PFSA (**Figures 3.17 and 1.1**), again supporting the importance of photoacidic behavior in order to observe relatively large values for V_{oc}.

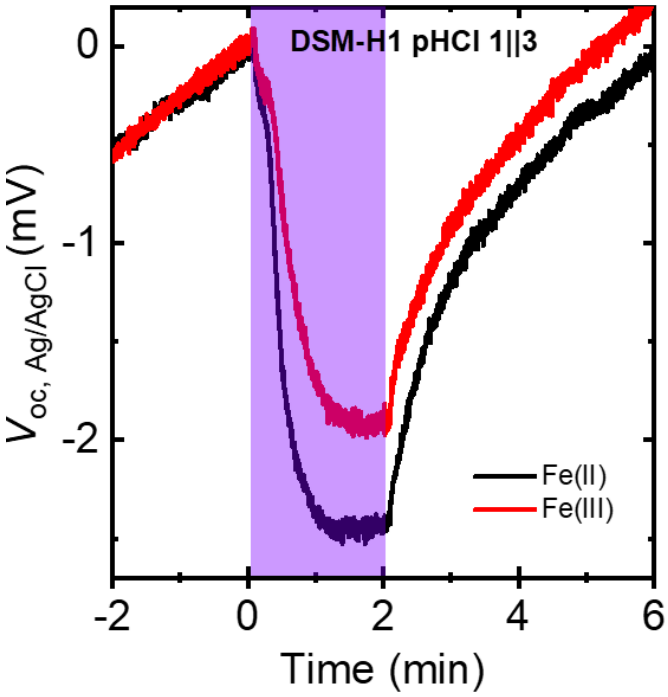

Figure 3.16. V_{oc} across **DSM-H1** when both electrolytes included 1 mM $Fe(ClO_4)_x(aq)$ where x = 2 or 3, and illuminated with 145 mW/cm^2 of 405 nm laser light (purple bar). Each measurement was baseline corrected for drift of the open-circuit potential by subtracting the open-circuit potential value just prior to the illumination event.

Comparison of HPTSA-modifed PFSA to its Methoxylated Analog, MeOPTSA-modified PFSA. A shortcoming of the non-photoacidic light absorbers used as negative controls, i.e. $[Ru^{II}(bpy)_3]^{2+}$ ionically associated into Nafion and carbon cloth affixed to Nafion, were that the light-absorbing

species were not covalently bound to the membrane. Therefore, we aimed to improve on these negative controls by developing a new dye where the photoacidic hydroxyl group in HPTSA was replaced with a methoxy group, resulting in the non-photoacidic molecule abbreviated MeOPTSA.

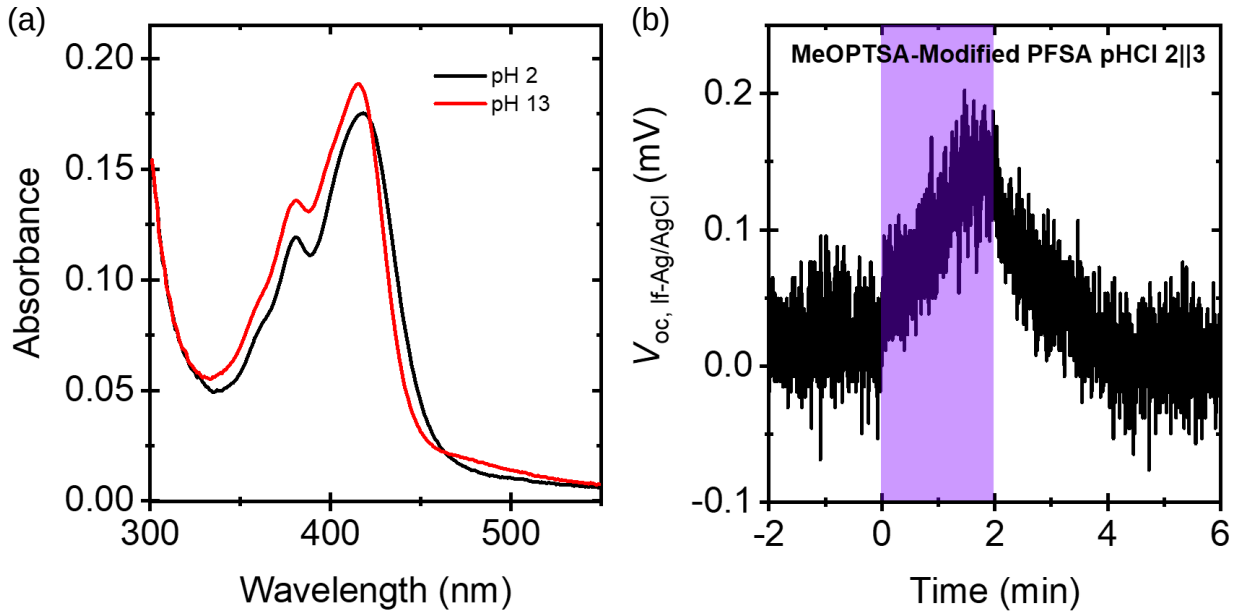

Figure 3.17. (a) Electronic absorption spectra of MeOPTSA-modified PFSA wetted by acidic (pH = 2) aqueous electrolyte (black) and alkaline (pH = 13) aqueous electrolyte (red). **(b)** Open-circuit photovoltage (V_{oc}) over time measured between two Ag/AgCl wires positioned across MeOPTSA-modified PFSA under conditions of 10 mM||1 mM HCl(aq) (pHCl 2||3) and illuminated with 150 mW/cm^2 of 405 nm laser light (purple bar).

Covalent bonding of MeOPTSA to PFSA resulted in a small bathochromic shift of its strongest absorption feature (**Figure 3.17a**), but the overall electronic absorption spectrum remained qualitatively similar to that observed for MeOPTS(aq). Increasing the pH of the aqueous electrolyte in contact with MeOPTSA-modified PFSA from 2 to 13 resulted in a small hypsochromic shift of its strongest absorption feature, consistent with deprotonation of free ammoniums on HPTSA/MeOPTSA that were not crosslinked with PFSA. Under conditions of pHCl 2||3, MeOPTSA-modified PFSA exhibited small positive V_{oc} values (**Figure 3.17b and 3.18a**), consistent with a decrease in the magnitude of the built-in electric potential as observed with traditional electronic solar cells. The small magnitude of V_{oc} values can be rationalized,

because 60% less photons were absorbed by MeOPTSA-modified PFSA as compared to other non-photoacidic controls, but the sign of the V_{oc} values was unexpected. Positive values for V_{oc} were only observed sporadically using $[Ru^{II}(bpy)_3]^{2+}$/Nafion (**Figure 3.11b**) and in the presence of a constant source of salt, e.g. in the presence of a salt-leaking SCE (**Figure 3.4**). The stability of MeOPTS was evaluated for MeOPTS in D_2O(l) in an NMR tube by illuminating it for 24 h at ~20 mW with a generic 405 nm presentation pointer, equivalent to ~1.9 h of constant illumination at the irradiance used in the electrochemical experiments. Changes in relative integrated signal intensities and/or the presence of new peaks, e.g. due to methanol at 3.34 ppm,[93] were not observed (**Figure 2.5**), suggesting that MeOPTS is photostable over the timescale of our experiment. This may indicate that mechanisms for generating photovoltages with modified PFSA may be different between MeOPTSA-modified PFSA and other non-photoacidic negative control dye molecules.

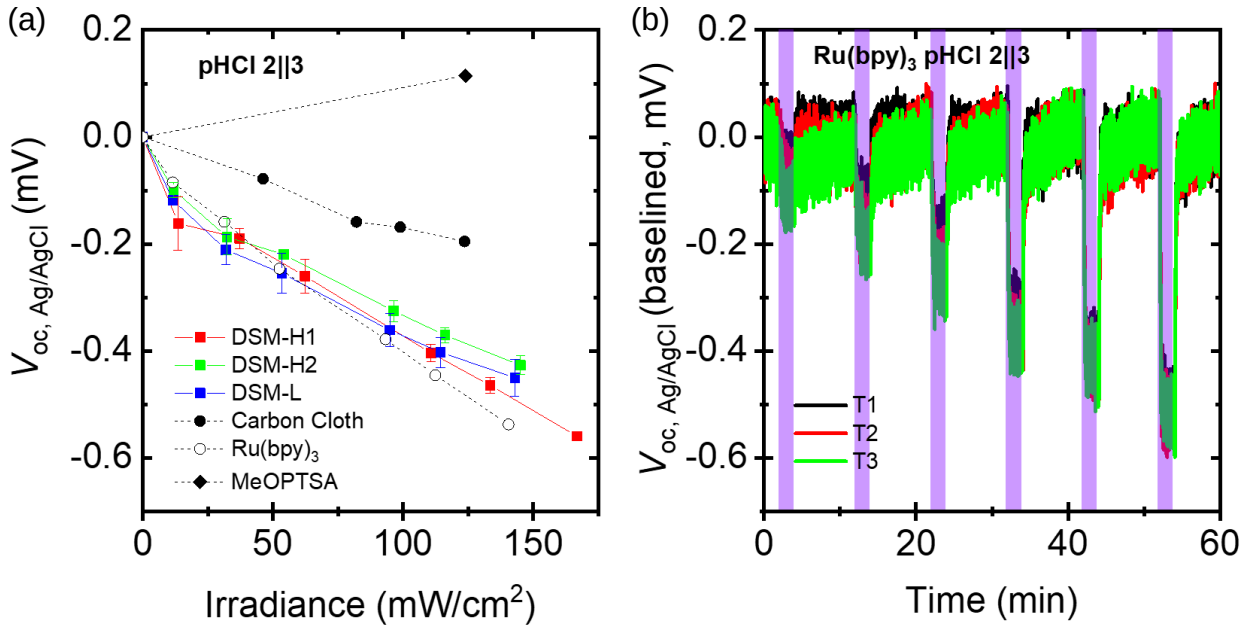

Figure 3.18. (a) Open-circuit photovoltage (V_{oc}) as a function of irradiance from 405 nm laser light measured between two Ag/AgCl wires positioned across Nafion membranes containing various photoabsorbers under conditions of 10 mM||1 mM HCl(aq) (pHCl 2||3). HPTSA ("**DSM**" datasets) was covalent bound to PFSA, $[Ru^{II}(bpy)_3]^{2+}$ was ionically associated into commercial Nafion NR-212, and carbon cloth was affixed to one side of commercial Nafion. Optical densities at 405 nm were >4, except for **DSM-L**, which was 0.664. Data and error bars for each **DSM-X** are the mean ± standard deviation of three trials while each negative control measurement was only performed once. **(b)** V_{oc} over time measured between two Ag/AgCl wires positioned across Nafion NR-212 with ionically associated $[Ru^{II}(bpy)_3]^{2+}$ under conditions of 10 mM||1 mM HCl(aq) (pHCl 2||3). Each measurement was baseline corrected for drift of the open-circuit potential by subtracting a line that spanned from the beginning of the first illumination event to the beginning of the sixth illumination event. Purple bars indicate times of 405 nm laser excitation (2 min each) with increasing intensity over time due to decreasing attenuation from a neutral density filter (1 ND, 0.6 ND, 0.4 ND, 0.2 ND, 0.1 ND, no filter). The maximum irradiance used was 170 mW/cm^2 and the condition of 1 Sun equivalent excitation occurs for an irradiance of 31.3 mW/cm^2. The legend indicates the chronological order of trials (T) taken on the same membrane, each with refreshed electrolyte.

Chapter 3.7: Experimental

Reagents and Chemicals. The following reagents were used as received from the indicated suppliers: hydrochloric acid (36.5-38.0%, Fisher Chemical), perchloric acid (70%, Alfa Aesar), sodium chloride (>99%, Fischer Chemical), sodium hydroxide (>95%, Macron Fine Chemicals), Nafion NR-212 poly(perfluorosulfonic acid) membrane (2 mil (50.8 μm) thick, equivalent weight (EW) = 1100, Ion Power), Nafion precursor poly(perfluorosulfonyl fluoride) membrane (2 mil (50.8 μm) thick, EW = 1100, C.G. Processing), carbon cloth (plain, Fuel Cell Earth), tris(2,2'-bipyridyl)ruthenium(II) chloride hexahydrate (98% Acros Organics), 2-propanol (>99.5%, Fischer Chemical), triethylamine (>99.5%, EMD Millipore Corporation), 8-hydroxypyrene-1,3,6 trisulfonic acid trisodium salt (HPTS, >98%, Carbosynth), methyl iodide (99%, Alfa Aesar), dimethylsulfoxide (>99.9%, fisher chemical), ethyl acetate (>99.5%, Fisher Chemical), acetone (>99.5%, Fisher Chemical), thionyl chloride (>99%, Sigma-Aldrich), *N*,*N*-dimethylformamide (>99.8%, Macron Fine Chemicals), dichloromethane (>99.5%, Macron Fine Chemicals), 1-boc-ethylenediamine (98%, Combi-Blocks), tetrahydrofuran (>99.9%, Fisher Chemical), acetonitrile (>99.5%, Fisher Chemical), chloroform (99.8%, VWR Chemical BDH), and trifluoroacetic acid (99%, Oakwood Chemical). Purified 8-hydroxypyrene-1,3,6-tris(2-aminoethylsulfonamide) (HPTSA), as the trifluoroacetate salt, was available from prior work.[34]

Synthesis of Methyoxylated Photoacid, MeOPTSA, as a Negative Control. The synthesis of MeOPTS was described in **Chapter 2.3**. Conversion of MeOPTS to its trisulfonamide variant, MeOPTSA, was performed using the protocol that we previously reported for conversion of HPTS to HPTSA,[34] with minor modification that purification was performed using column chromatography (Teledyne ISCO, CombiFlash NextGen 300+).

Covalent and Ionic Bonding of Dyes in Nafion Membranes. Synthesis of PFSA ion-exchange membranes with covalently bound HPTSA and MeOPTSA, and Nafion with ionically associated $[Ru^{II}(bpy)_3]^{2+}$, where bpy is 4,4'-bipyridine, were described in our previous works.[20] Briefly, for covalently bound dye-modified PFSA, a sheet of Nafion precursor poly(perfluorosulfonyl fluoride) was cut into ~3 x 3 cm membranes. The membranes were bathed and stirred in a scintillation vial filled with 75 µL of 1M NaOH(aq), 45 µL of triethylamine, and the following dye solutions at 90 ºC for 7 days. For **DSM-H1** and **DSM-H2**, 5 mg HPTSA in 20 mL isopropyl alcohol was used for PFSA modification (>4 OD at 405 nm) while a ten-fold serial dilution of this solution was used to synthesize **DSM-L** with a lower dye density. An arbitrary amount of purified MeOPTSA was directly transferred from column chromatography to 20 mL of isopropyl alcohol for the synthesis of MeOPTSA-modified PFSA due to low yields. For $[Ru^{II}(bpy)_3]^{2+}$ ionically associated into Nafion, a sheet of Nafion NR-212 was cut into ~3 x 3 cm membranes and pretreated by stirring in 1 M H_2SO_4(aq) for 1 h on a stirplate, followed by copious rinsing and storage in deionized water until use. The pretreated membranes were placed in scintillation vials containing 6 mg $[Ru^{II}(bpy)_3]Cl_2$ in 5 mL of 1 M H_2SO_4(aq) and stirred for 36 h at 80 °C using a sand bath. No emphasis was placed on any specific orientation of PFSA during modification or photoelectrochemical measurements.

Absorption and Photoluminescence Spectroscopy. Absorption and photoluminescence spectra were obtained using a spectrometer (Duetta, HORIBA). HPTSA-modified PFSA was mounted in a custom sample holder machined out of KEL-F and similar to H-cells used previously for our photoelectrochemical studies.[20,22] Notable modifications include the use of four glass windows in a rectangular arrangement to allow for in situ probing of right-angle photoluminescence and positioning of the membranes at an angle of 50 degrees relative to the optical axis (**Figure 3.7a**)

to prevent specular reflection of light from the excitation beam directly into the "right-angle" detector. Membranes were placed in-between two parafilm gaskets with slightly oval cutouts, to match the opening in the KEL-F block at 50 degrees. Absorption spectra were baseline corrected using the sample holder filled with ultrapure water in the absence of a sample. Photoluminescence spectra were collected for 400 nm light excitation in a right-angle configuration with 5 nm excitation and emission slit widths and with resulting data autocorrected for the wavelength-dependent sensitivity of the detection system.

Photoelectrochemical Measurements. Electrochemical measurements were conducted using a potentiostat (VSP-300, Biologic) in a four-electrode configuration consisting of platinum mesh current-carrying electrodes (0.15 cm^2) and Ag/AgCl potential-sensing electrodes. These sensing electrodes were prepared by sanding an Ag wire, rinsing it with dilute nitric acid, and rinsing it with copious amounts of ultrapure water, followed by immersing ~3 cm of the bottom of the clean Ag wires in an aqueous 8.25% sodium hypochlorite generic bleach solution for 15 min. After oxidation, the Ag/AgCl wires were rinsed and aged in ultrapure water overnight. To physically block incident illumination from interacting with the Ag/AgCl wires, a piece of Teflon tubing that was encased in opaque polyolefin heat-shrink was used as a sheath for the Ag/AgCl wires. Membranes were placed in-between two parafilm gaskets with circular cutouts (1.4 cm diameter) to define the geometric membrane active area. Specifically, for the experiment that used carbon cloth affixed to Nafion NR-212, before loading into the parafilm gasket carbon cloth was placed against Nafion that had been cut into ~3 x 3 cm membranes and pretreated by stirring in 1 M H_2SO_4(aq) for 1 h on a stirplate, followed by copious rinsing and storage in deionized water until use. Each chamber contained 9 mL of aqueous electrolyte that wetted the membrane to form an active area of 1.54 cm^2. Working electrodes were placed in the larger concentration (concentrated)

electrolyte chamber for all experiments. The concentrated and dilute electrolyte chambers form the low-impedance charge-collection junction and the rectifying charge-separation junction, respectively. Glass Luggin–Haber capillaries each with a ~1 mm tip diameter were installed ~1 mm from each side of the membrane to minimize potential drop due to uncompensated resistance between the Ag/AgCl sensing electrodes and to physically place the Ag/AgCl wires away from the path of incident illumination. Polyethylene terephthalate tubes were affixed to the fill ports of our custom H-cell to allow the aqueous electrolyte to remain at a large distance above the cell so that the current-carrying wires could also be positioned out of the path of incident illumination.

Optical excitation was achieved with a continuous-wave laser diode (L405G1, Thorlabs; 405 ± 5 nm) beam expanded to slightly underfill the active area of the membrane. The irradiance was adjusted with a set of neutral density filters and measured with a thermopile detector (S310C, Thorlabs). A monochromatic excitation source was used instead of a white-light source to minimize effects due to heating and, in general, to allow for facile quantification of quantum yields, which are not reported herein. Monochromatic irradiance at 405 nm was converted into equivalent Suns excitation by taking the ratio of the absorbed photon fluence rate for **DSM-H1** at 405 nm and the expected absorbed photon fluence rate of **DSM-H1** under reference air mass 1.5 global solar spectral irradiance,[94] as calculated in previous works.[20,21,95] An equivalent excitation of 1 Sun was determined to be equal to 31.3 mW/cm^2 of 450 nm light. Photoresponse data are reported as the mean of data collected 117.5 s ± 2.5 s into a 2-min period of illumination versus data in the dark before illumination. After illumination, the system was allowed to return to its pre-illumination state by sitting in the dark for at least 3 min, which is the minimum time needed to reach a quasi-steady-state signal. Each of these processes was controlled by a custom optical shutter.

All membranes were positioned in our custom H-cell containing the desired experimental electrolytes in each chamber and allowed to soak for at least 10 min, followed by exchange of the soaking electrolyte with fresh electrolyte prior to photoelectrochemical evaluation. When an experiment required changing the composition of an electrolyte, e.g. from HCl(aq) to KCl(aq), membranes were submerged in 1 M of the new aqueous electrolyte, with a large enough volume so that electrolyte species were in excess, and stirred overnight, followed by copious rinsing with deionized water and storage in the lowest concentration experimental electrolyte to be used. V_{oc} values as a function of irradiance were collected by performing three trials under the same experimental conditions, refreshing the electrolyte after each trial, and are reported in reference to the corresponding open-circuit potential (E_{oc}) in the dark, meaning that $V_{oc} = E_{meas} - E_{oc}$, where E_{meas} is the measured potential difference. Negative control experiments were each conducted once using $[Ru^{II}(bpy)_3]^{2+}$ ionically associated into Nafion, carbon cloth affixed to Nafion, and MeOPTSA-modified PFSA. Chronoamperometry measurement used to quantify membrane conductance were performed out of sequence by alternating the polarity of the applied potential bias before increasing the magnitude of the applied potential bias in order to reduce net transport of ions across the membrane.

References

1. Chapin, D. M., Fuller, C. S. & Pearson, G. L. A New Silicon p-n Junction Photocell for Converting Solar Radiation into Electrical Power. *J. Appl. Phys.* **25**, 676 (1954).

2. Mulligan, W. P. *et al. MANUFACTURE OF SOLAR CELLS WITH 21% EFFICIENCY*. www.sunpowercorp.com (2004).

3. Shockley, W. & Queisser, H. J. Detailed balance limit of efficiency of p-n junction solar cells. *J. Appl. Phys.* **32**, 510–519 (1961).

4. Würfel, U., Cuevas, A. & Würfel, P. Charge carrier separation in solar cells. *IEEE J. Photovoltaics* **5**, 461–469 (2015).

5. Nielander, A. C., Shaner, M. R., Papadantonakis, K. M., Francis, S. A. & Lewis, N. S. A taxonomy for solar fuels generators. *Energy Environ. Sci.* **8**, 16–25 (2015).

6. Steinberg-Yfrach, G. *et al.* Conversion of light energy to proton potential in liposomes by artificial photosynthetic reaction centres. *Nature* **385**, 239–241 (1997).

7. Xie, X., Crespo, G. A., Mistlberger, G. & Bakker, E. Photocurrent generation based on a light-driven proton pump in an artificial liquid membrane. *Nat. Chem.* **6**, 202–7 (2014).

8. Wang, L. *et al.* Light-Driven Active Proton Transport through Photoacid- and Photobase-Doped Janus Graphene Oxide Membranes. *Adv. Mater.* **31**, 1903029 (2019).

9. Lehovec, K. Theorie des sperrschicht-photoeffekts. *Zeitschrift fur Naturforsch. - Sect. A J. Phys. Sci.* **1**, 258–263 (1946).

10. Lehovec, K. A new theory of the junction photo effect. *Opt.* **1**, 268 (1946).

11. Lehovec, K. The photo-voltaic effect. *Phys. Rev.* **74**, 463–471 (1948).

12. Würfel, P. & Würfel, U. *Physics of solar cells: From basic principles to advanced concepts*,

second updated and expanded edition. (Wiley-VCH, 2009).

13. Shockley, W. The Theory of p-n Junctions in Semiconductors and p-n Junction Transistors. *Bell Syst. Tech. J.* **28**, 435–489 (1949).

14. Ardo, S. & Meyer, G. J. Photodriven heterogeneous charge transfer with transition-metal compounds anchored to TiO2 semiconductor surfaces. *Chem. Soc. Rev.* **38**, 115–164 (2009).

15. O'Regan, B. & Grätzel, M. A low-cost, high-efficiency solar cell based on dye-sensitized colloidal TiO2 films. *Nature* **353**, 737–740 (1991).

16. Hagfeldt, A., Boschloo, G., Sun, L., Kloo, L. & Pettersson, H. Dye-sensitized solar cells. *Chem. Rev.* **110**, 6595–6663 (2010).

17. Brennaman, M. K. *et al.* Finding the Way to Solar Fuels with Dye-Sensitized Photoelectrosynthesis Cells. *J. Am. Chem. Soc.* **138**, 13085–13102 (2016).

18. Cao, W. & Xue, J. Recent progress in organic photovoltaics: Device architecture and optical design. *Energy Environ. Sci.* **7**, 2123–2144 (2014).

19. Inganäs, O. Organic Photovoltaics over Three Decades. *Adv. Mater.* **30**, 1800388 (2018).

20. White, W., Sanborn, C. D., Reiter, R. S., Fabian, D. M. & Ardo, S. Observation of Photovoltaic Action from Photoacid-Modified Nafion Due to Light-Driven Ion Transport. *J. Am. Chem. Soc.* **139**, 11726–11733 (2017).

21. White, W., Sanborn, C. D., Fabian, D. M. & Ardo, S. Conversion of Visible Light into Ionic Power Using Photoacid-Dye-Sensitized Bipolar Ion-Exchange Membranes. *Joule* **2**, 94–109 (2018).

22. White, W. *et al.* Evaluation of the role that photoacid excited-state acidity has on photovoltage and photocurrent of dye-sensitized ion-exchange membranes. in *Physical Chemistry of Semiconductor*

Materials and Interfaces XVIII vol. 11084 12 (SPIE, 2019).

23. Lakowicz, J. R. Principles of fluorescence spectroscopy. in *Principles of Fluorescence Spectroscopy* 260–262 (Springer, 2006). doi:10.1007/978-0-387-46312-4.

24. Tolbert, L. M. & Solntsev, K. M. Excited-state proton transfer: From constrained systems to 'super' photoacids to superfast proton transfer. *Acc. Chem. Res.* **35**, 19–27 (2002).

25. Phun, G. No Title. *Energy Environ. Sci.* to be submitted shortly.

26. Tran-Thi, T.-H., Gustavsson, T., Prayer, C., Pommeret, S. & Hynes, J. T. Primary ultrafast events preceding the photoinduced proton transfer from pyranine to water. *Chem. Phys. Lett.* **329**, 421–430 (2000).

27. Pines, E. & Huppert, D. Geminate recombination proton-transfer reactions. *Chem. Phys. Lett.* **126**, 88–91 (1986).

28. Ross, R. T. & Hsiao, T. L. Limits on the yield of photochemical solar energy conversion. *J. Appl. Phys.* **48**, 4783–4785 (1977).

29. Hammett, L. P. & Deyrup, A. J. A SERIES OF SIMPLE BASIC INDICATORS. I. THE ACIDITY FUNCTIONS OF MIXTURES OF SULFURIC AND PERCHLORIC ACIDS WITH WATER1. *J. Am. Chem. Soc.* **54**, 2721–2739 (1932).

30. Bell, R. P., Dowding, A. L. & Noble, J. A. The kinetics of ester hydrolysis in concentrated aqueous acids. *J. Chem. Soc.* 3106–3110 (1955) doi:10.1039/JR9550003106.

31. Paul, M. A. & Long, F. A. H0 And Related Indicator Acidity Function. *Chem. Rev.* **57**, 1–45 (1957).

32. Sanborn, C. D. Aqueous Ionic Photovoltaics from Photoacid-Sensitized Ion-Selective Polymers. (University of California, Irvine, 2017).

33. Washburn, E. R. & Olsen, A. L. The precision with which the concentrations of solutions of hydrochloric acid and sodium hydroxide may be determined with the immersion refractometer. *J. Am. Chem. Soc.* **54**, 3212–3218 (1932).

34. Sanborn, C. D., Chacko, J. V., Digman, M. & Ardo, S. Interfacial and Nanoconfinement Effects Decrease the Excited-State Acidity of Polymer-Bound Photoacids. *Chem* **5**, 1648–1670 (2019).

35. Eigen, M. Fast elementary steps in chemical reaction mechanisms. *Pure Appl. Chem.* **6**, 97–116 (1963).

36. Förster, T. & Völker, S. Kinetics of proton transfer reactions involving hydroxypyrene-trisulphonate in aqueous solution by nanosecond laser absorption spectroscopy. *Chem. Phys. Lett.* **34**, 1–6 (1975).

37. Perrin, C. L., Dwyer, T. J. & Baine, P. Two-Dimensional NMR Exchange Spectroscopy Study of Proton Exchange in Aqueous Ammonium Ion: H/D Primary Kinetic Isotope Effect for Direct Nitrogen-to-Nitrogen Proton Transfer. *J. Am. Chem. Soc.* **116**, 4044–4049 (1994).

38. Xia, H. L., Ardo, S., Sarjeant, A. A. N., Huang, S. & Meyer, G. J. Photodriven spin change of Fe(II) benzimidazole compounds anchored to nanocrystalline TiO2 thin films. *Langmuir* **25**, 13641–13652 (2009).

39. Eigen, M. Proton Transfer, Acid-Base Catalysis, and Enzymatic Hydrolysis. Part I: ELEMENTARY PROCESSES. *Angew. Chemie Int. Ed. English* **3**, 1–19 (1964).

40. Kotlyar, A. B., Borovok, N., Raviv, S., Zimanyi, L. & Gutman, M. Fast Redox Perturbation of Aqueous Solution by Photoexcitation of Pyranine. *Photochem. Photobiol.* **63**, 448–454 (1996).

41. Friedrich, D. *et al.* Dye regeneration dynamics by electron donors on mesoscopic TiO2 films. *J. Phys. Chem. C* **118**, 3420–3425 (2014).

42. Cong, J., Hao, Y., Sun, L. & Kloo, L. Two Redox Couples are Better Than One: Improved Current

and Fill Factor from Cobalt-Based Electrolytes in Dye-Sensitized Solar Cells. *Adv. Energy Mater.* **4**, 1301273 (2014).

43. Donten, M. L. & Hamm, P. pH-Jump Overshooting. *J. Phys. Chem. Lett.* **2**, 1607–1611 (2011).

44. Eigen, M. & De Maeyer, L. Self-dissociation and protonic charge transport in water and ice. *Proc. R. Soc. London. Ser. A. Math. Phys. Sci.* **247**, 505–533 (1958).

45. Natzle, W. C. & Moore, C. B. Recombination of hydrogen ion (H+) and hydroxide in pure liquid water. *J. Phys. Chem.* **89**, 2605–2612 (1985).

46. Bard, A. J. & Faulkner, L. R. *Electrochemical Methods Fundamentals and Applications, Second Edition*. (Wiley, 2001).

47. Barron, A. R. The interaction of carboxylic acids with aluminium oxides: journeying from a basic understanding of alumina nanoparticles to water treatment for industrial and humanitarian applications. *Dalt. Trans.* **43**, 8127 (2014).

48. Simkovitch, R., Karton-Lifshin, N., Shomer, S., Shabat, D. & Huppert, D. Ultrafast Excited-State Proton Transfer to the Solvent Occurs on a Hundred-Femtosecond Time-Scale. *J. Phys. Chem. A* **117**, 3405–3413 (2013).

49. Ardo, S. & Meyer, G. J. Characterization of Photoinduced Self-Exchange Reactions at Molecule–Semiconductor Interfaces by Transient Polarization Spectroscopy: Lateral Intermolecular Energy and Hole Transfer across Sensitized TiO2 Thin Films. *J. Am. Chem. Soc.* **133**, 15384–15396 (2011).

50. Glancy, J. A. Confirmation of Photoacidic Quantum Dots Using Electrochemical Impedance Spectroscopy. (University of California, Irvine, 2019).

51. Haghighat, S., Ostresh, S. & Dawlaty, J. M. Controlling Proton Conductivity with Light: A Scheme Based on Photoacid Doping of Materials. *J. Phys. Chem. B* **120**, 1002–1007 (2016).

52. Fonash, S. J. *Solar Cell Device Physics*. (Academic Press, 2010).

53. Tan, M. X. *et al.* Principles and Applications of Semiconductor Photoelectrochemistry. in *Progress in Inorganic Chemistry* vol. 41 21–144 (Wiley, 2007).

54. Walter, M. G. *et al.* Solar water splitting cells. *Chem. Rev.* **110**, 6446–6473 (2010).

55. Lewis, N. S. A Quantitative Investigation of the Open-Circuit Photovoltage at the Semiconductor/Liquid Interface. *J. Electrochem. Soc.* **131**, 2496 (1984).

56. Grimm, R. L. *et al.* Comparison of the photoelectrochemical behavior of h-terminated and methyl-terminated Si(111) surfaces in contact with a series of one-electron, outer-sphere redox couples in CH 3CN. *J. Phys. Chem. C* **116**, 23569–23576 (2012).

57. Bansal, A. & Lewis, N. S. Stabilization of Si photoanodes in aqueous electrolytes through surface alkylation. *J. Phys. Chem. B* **102**, 4058–4060 (1998).

58. Kalan, R. E., Russell, M. A., Taylor, J. L. & Grimm, R. L. Dual Liquid Junction Photoelectrochemistry: Part I. Dual-Cuvette and Dual-Thin-Film Cells for Screening and Quantification of Back-Contact Properties. *J. Electrochem. Soc.* **164**, H798–H804 (2017).

59. Russell, M. A. *et al.* Dual Liquid Junction Photoelectrochemistry: Part II. Open-Circuit Photovoltage Variations Due to Surface Chemistry, Interfacial Dipoles, and Non-Ohmic Junctions at Back Contacts. *J. Electrochem. Soc.* **166**, H608–H614 (2019).

60. Newman, J. & Thomas-Alyea, K. E. *Electrochemical Systems*. (2004).

61. Bockris, J. O. & Reddy, A. K. N. *Modern Electrochemistry 1: Ionics*. *Modern Electrochemistry 2B* (Springer US, 1998). doi:10.1007/0-306-48036-0_1.

62. Henderson, P. The Thermodynamics of Liquid Cells. *Zeitschrift für Phys. Chemie* **59**, 118 (1907).

63. Goldman, D. E. Potential, impedance, and rectification in membranes. *J. Gen. Physiol.* **27**, 37–60

(1943).

64. Ward, K. R., Dickinson, E. J. F. & Compton, R. G. Dynamic theory of membrane potentials. *J. Phys. Chem. B* **114**, 10763–10773 (2010).

65. Reiter, R. S., White, W. & Ardo, S. Communication—Electrochemical Characterization of Commercial Bipolar Membranes under Electrolyte Conditions Relevant to Solar Fuels Technologies. *J. Electrochem. Soc.* **163**, H3132–H3134 (2016).

66. Donnan, F. G. The theory of membrane equilibria. *Chem. Rev.* **1**, 73–90 (1924).

67. Manning, G. S. Limiting laws and counterion condensation in polyelectrolyte solutions I. Colligative properties. *J. Chem. Phys.* **51**, 924–933 (1969).

68. Kusoglu, A. & Weber, A. Z. New Insights into Perfluorinated Sulfonic-Acid Ionomers. *Chem. Rev.* **117**, 987–1104 (2017).

69. The Chemours Company. *Nafion NR211 and NR212 Ion Exchange Materials*. (2017).

70. Kamcev, J., Paul, D. R. & Freeman, B. D. Effect of fixed charge group concentration on equilibrium ion sorption in ion exchange membranes. *J. Mater. Chem. A* **5**, 4638–4650 (2017).

71. Hu, S. *et al.* Proton transport through one-atom-thick crystals. *Nature* **516**, 227–230 (2014).

72. Achtyl, J. L. *et al.* Aqueous proton transfer across single-layer graphene. *Nat. Commun.* **6**, 1–7 (2015).

73. Moody, G. J., Oke, R. B. & Thomas, J. D. R. The influence of light on silver-silver chloride electrodes. *Analyst* **94**, 803–804 (1969).

74. Kim, T., Logan, B. E. & Gorski, C. A. High power densities created from salinity differences by combining electrode and Donnan potentials in a concentration flow cell. *Energy Environ. Sci.* **10**, 1003–1012 (2017).

75. Tauc, J. & Závětová, M. Photo-piezoelectric effect in semiconductors. *Czechoslov. J. Phys.* **9**, 572–577 (1959).

76. Moerner, W. E. Photorefractive Polymers. in *Encyclopedia of Materials: Science and Technology* 6961–6968 (Elsevier, 2001). doi:10.1016/b0-08-043152-6/01233-x.

77. Ju, L. *et al.* Photoinduced doping in heterostructures of graphene and boron nitride. *Nat. Nanotechnol.* **9**, 348–352 (2014).

78. Osterloh, F. E. *et al.* P3HT:PCBM bulk-heterojunctions: Observing interfacial and charge transfer states with surface photovoltage spectroscopy. *J. Phys. Chem. C* **118**, 14723–14731 (2014).

79. Pockett, A. *et al.* Origin of Exceptionally Slow Light Soaking Effect in Mesoporous Carbon Perovskite Solar Cells with AVA Additive. *J. Phys. Chem. C* **123**, 11414–11421 (2019).

80. Deppe, T. & Munday, J. N. Nighttime Photovoltaic Cells: Electrical Power Generation by Optically Coupling with Deep Space. *ACS Photonics* **7**, 1–9 (2020).

81. Schulte, L., White, W., Renna, L. A. & Ardo, S. Turning Water into a Solar Cell by Protonic Doping and Dye Sensitization. *Joule* under review.

82. Giro, G., Di Marco, P. G. & Casalbore, G. Photochemical behaviour of Ru(bpy)3Cl2 complex in strong acidic media. *Inorganica Chim. Acta* **50**, 201–204 (1981).

83. Hodes, G. & Kamat, P. V. Understanding the Implication of Carrier Diffusion Length in Photovoltaic Cells. *J. Phys. Chem. Lett.* **6**, 4090–4092 (2015).

84. Fonash, S. J. & Ashok, S. An additional source of photovoltage in photoconductive materials. *Appl. Phys. Lett.* **35**, 535–537 (1979).

85. Zawodzinski, T. A. Water Uptake by and Transport Through Nafion® 117 Membranes. *J. Electrochem. Soc.* **140**, 1041 (1993).

86. Shi, S. *et al.* Impact of hygrothermal aging on structure/function relationship of perfluorosulfonic-acid membrane. *J. Polym. Sci. Part B Polym. Phys.* **54**, 570–581 (2016).

87. Turlington, M. D., Troian-Gautier, L., Sampaio, R. N., Beauvilliers, E. E. & Meyer, G. J. Ligand Control of Supramolecular Chloride Photorelease. *Inorg. Chem.* **57**, 5624–5631 (2018).

88. Ardo, S. *et al. Systems and methods for integrated solar photodialysis*. (2019).

89. Elimelech, M. & Phillip, W. A. The future of seawater desalination: Energy, technology, and the environment. *Science (80-.).* **333**, 712–717 (2011).

90. Patel, S. K. *et al.* The relative insignificance of advanced materials in enhancing the energy efficiency of desalination technologies. *Energy Environ. Sci.* **13**, 1694–1710 (2020).

91. Ardo, S. *et al. Light-driven ion-pumping membrane systems.* (2018).

92. Zhou, Y. & Tol, R. S. J. Evaluating the costs of desalination and water transport. *Water Resour. Res.* **41**, 1–10 (2005).

93. Fulmer, G. R. *et al.* NMR chemical shifts of trace impurities: Common laboratory solvents, organics, and gases in deuterated solvents relevant to the organometallic chemist. *Organometallics* **29**, 2176–2179 (2010).

94. Reference Air Mass 1.5 Spectra | Grid Modernization | NREL. https://www.nrel.gov/grid/solar-resource/spectra-am1.5.html.

95. Chen, H. Y. & Ardo, S. Direct observation of sequential oxidations of a titania-bound molecular proxy catalyst generated through illumination of molecular sensitizers. *Nat. Chem.* **10**, 17–23 (2018).